Oxidative dehydrogenation (ODH) of ethane to ethene over supported vanadium containing oxide catalysts

Thesis submitted in accordance with the requirement of Cardiff University for the degree of Doctor of Philosophy

Asad Ahmad Khan

2016

DECLARATION

This work has not previously been accepted in substance for any degree and is not concurrently submitted in candidature for any degree.

Signed …………………………………….. (Candidate) Date ………………….......

STATEMENT 1

This thesis is being submitted in partial fulfillment of the requirements for the degree of PhD.

Signed …………………………………….. (Candidate) Date ………………….......

STATEMENT 2

This thesis is the result of my own independent work/investigation, except where otherwise state. Other sources are acknowledged by explicit references.

Signed …………………………………….. (Candidate) Date ………………….......

STATEMENT 3

I hereby give consent for my thesis, if accepted, to be available for photocopy and for inter-library loan, and for the title and summary to be made available to outside organizations.

Signed …………………………………….. (Candidate) Date ………………….......

STATEMENT 4

I hereby give consent for my thesis, if accepted, to be available for photocopying and for inter-library loans **after expiry of a bar on access previously approved by the Graduate Development Committee.**

Signed …………………………………….. (Candidate) Date ………………….......

Abstract

In this thesis work oxidative dehydrogenation (ODH) of ethane to ethene over MoV oxide catalyst was investigated. The influence of the preparation techniques and different reaction conditions were studied thoroughly. It was found that the precipitation method for the catalyst preparation using variable pH produces a more active catalyst at pH values of 3 to 3.5. Slurry temperature and calcination temperature are also very important parameters which affect the selectivity pattern of the products. This selectivity pattern was found to be further influenced by reaction temperature, pressure, GHSV and ethane-oxygen ratio in the feed.

The influence of the V: Mo ratio on the performance of the catalyst for the ODH was investigated by several characterization techniques, such as BET, XRD, XPS, TEM, SEM, EDX coupled with catalytic performance tests in a fixed bed reactor. The optimum V: Mo ratio was found to be 0.25:1 (i.e., $Mo_1V_{0.40}$). At this ratio, the oxidation state of vanadium with respect to total vanadium concentration (V^{5+}/ V^{total}) is at an optimum in terms of the adsorption strength of the desired products. It was further fine-tuned by investigating the influence of reaction conditions.

An improvement on the most active MoV oxide catalyst for the ODH reaction was developed with the addition of oxalic acid as the vanadium dissolution and pH adjustment agent. Addition of oxalic acid influenced the catalytic properties in a variety of ways as observed from characterization and reaction results. Addition of either a smaller amount or an excess amount compared with the optimal amount has determental impact on the activity of the catalyst. Further catalytic activities were tested by the addition of different types of supports (e.g., ZrO_2, TiO_2, Nb_2O_5, SiO_2, and Al_2O_3) into the MoV oxide catalytic system. The alumina support was extensively tested with different amounts onto the base MoV oxide for the ethane ODH to ethene.

To my Parents

To the glory of God

<u>ACKNOWLEDGEMENTS</u>

<u>CONTENTS</u>

LIST OF TABLES

LIST OF FIGURES

<u>LIST OF ABBREVIATIONS</u>

AA – Acetic Acid

BE – Binding Energies

BET – Brunauer, Emmett, Teller (Surface area)

CO_x – Carbon Oxide

CT – Contact Time

EDX – Energy Dispersive X-ray Spectroscopy

EPR – Electron Paramagnetic Resonance

FCC – Fluid Catalytic Cracking

FID – Flame Ionization Detector

FWHM – Full Width Half Maximum

GHSV – Gas Hourly Space Velocity

IR – Infrared Spectroscopy

JCPDS – Joint Committee on Powder Diffractions Standard

µL – Micro litre

µm – Micro Metre

ODH – Oxidative Dehydrogenation

ODHE – Oxidative Dehydrogenation of Ethane

SEM – Scanning Electron microscopy

SSTIKA – Steady State Transeint Isotopic Kinetic Analysis

SV – Space Velocity

TCD – Thermal Conductivity Detector

TEM – Transmission Electron Microscopy

TGA – Thermogravimetric Analysis

XPS – X-ray Photoelectron Spectroscopy

XRD – X-ray Powder Diffraction

XRF – X-ray Fluorescence

Aims and Scope of the thesis

The aim of this thesis is to investigate a catalytic system for the production of ethene through the ODH of ethane using vanadium-based mixed oxide catalysts. For this purpose molybdenum-vanadium-oxide and molybdenum-vanadium-supported catalysts were prepared, characterized and tested for their catalytic performance at various feed concentrations, space velocities and temperatures at steady state.

The tuning of MoV oxide properties to fit one or the other reaction is a feature of this system which is versatile enough to incorporate with other elements. The presence of these elements (whatever their nature and their content) is obviously a prominent factor to develop a more prominent sustainable catalytical system.

The following variables were investigated:

- catalyst composition and structure,
- preparation parameters such as drying time, ageing and calcination temperature,
- metal concentration, and
- reaction conditions such as temperature, pressure, contact time and reactant composition

Furthermore, the ODH of ethane was carried out at relatively low temperature with an exothermic reaction in the presence of properly selected MoV oxide catalysts.

Chapter 1

Introduction

1.1 Objectives and justification

The presence of the light alkanes ethane and propane in natural gas is considered to be one of the most attractive raw materials for the petrochemical industries for producing lower alkenes and many other intermediates. The chemical industry relies heavily on unsaturated hydrocarbons (alkenes with at least one carbon-carbon double bond) as a feedstock for many industrially significant processes. The present industrial capacity for lower alkenes such as ethene, propene and butenes is expected to be insufficient due to the increasing demands of the petrochemical industry [1-2].

Presently, the selective oxidation of n-butane to maleic anhydride using vanadium phosphorus oxide catalysts is the only industrial process involving the selective oxidation

of a light alkane [3] leaving a wide scope for their utilization in other chemical process. Conversion of alkanes to alkenes is one of the industrially important practices. Since the current chemical industry depends heavily on the use of alkenes as starting materials, if alkanes can be dehydrogenated to alkenes with high yields, they can become a valuable alternate feedstock [4].

Presently, the traditional methods for the production of light alkenes involve catalytic or steam cracking of naphtha and fluid catalytic cracking (FCC) of petroleum crude oil [5]. While these two routes are very well developed, increasing the capacity of these processes is only possible to some extent, as the changing regulations limit the use of byproducts (notably aromatic molecules) in fuels. The rate at which refineries can increase their alkene production is also limited by the complexity of refinery processes, thus for satisfactory alkene production, industry needs dedicated alkene producing processes. Conventional dehydrogenation reactions are reversible due to the hydrogen evolved, and the alkane conversion is limited by the thermodynamic equilibrium. In order to shift it towards the formation of the dehydrogenation products, the reactions are carried out at relatively high temperatures (from 550 ºC to 650 ºC). However, at these temperatures, cracking of hydrocarbons occurs, reducing the alkene selectivity [5]. Moreover, coke deposition causes a decrease in catalyst activity and there is a need for the frequent regeneration [6].

Hence as a route to light alkenes catalytic dehydrogenation of alkanes shows some major disadvantages, i.e. thermodynamic limitations, a high tendency to coking and consequently short catalyst lifetime [5]. A conceptually interesting way to overcome the thermodynamic limitation in the direct dehydrogenation reaction is to couple it with hydrogen oxidation [7]. Moreover, the presence of oxygen limits coking and therefore extends catalyst lifetime. This new concept of alkene production, generically called

oxidative dehydrogenation (ODH), has been thoroughly studied in the literature motivated by the prospect of a new alternative process which overcomes the above-mentioned advantages [5-7]. Despite the large amount of research effort, industrial scale application of the ODH reaction has not been realized to date due to the low alkene selectivity shown by the catalysts that are currently available. The main problem with most of the catalysts studied for ODH is that alkene yields typically do not exceed 30 % [8]. Conventional transition metal oxides with pronounced redox properties such as supported vanadium catalysts have been explored [9-12], but have not been seen as promising, as readsorption of alkenes (leading to total oxidation) appears to limit the alkene yield [13,14].

1.2 Current methods of alkene production

Most of the lower alkenes produced are converted directly or indirectly to polymers and other synthetic materials. Demands for these new synthetic materials are steadily increasing year by year, the need for lower alkenes, especially ethene and propene follows this demand. The entire capacity of [C_2-C_4] alkenes worldwide is produced by three commercial processes: thermal cracking (pyrolysis or steam cracking), catalytic cracking and catalytic dehydrogenation. A brief description of these processes is given in the following sections [15-17].

1.2.1 Thermal cracking (Steam cracking)

Today 70 % of alkene production comes from thermal cracking of various petroleum hydrocarbons, most often liquefied petroleum gas (LPG) and naphtha, with steam; the process is commonly called steam cracking or pyrolysis. The main product of steam cracking is ethene; propene and limited amounts of higher alkene are byproducts from this process. A hydrocarbon stream is heated by heat exchange against flue gas

combustion in the convection section, mixed with steam, and further heated to the incipient cracking temperature 500-700 °C, depending on the feedstock. The stream then enters a fired tubular reactor (radiant tube or radiant coil) where, under controlled contact time, temperature profile, and partial pressure, it is heated from 500–650 °C to 750–900 °C in two steps for a short time. During this short reaction time hydrocarbons in the feedstock are cracked into smaller molecules; ethene, other alkenes and dienes are the major products. Since the conversion of alkanes to alkenes in the radiant tube is highly endothermic, high energy input rates are needed. The reaction products leave the radiant tube at high temperature and are cooled to 550–650 °C in a few seconds to prevent degradation of the highly reactive products by secondary reactions. The resulting product mixtures are then separated into the desired products by using a complex sequence of separation and chemical-treatment steps which can vary widely, depending on feedstock and severity of the cracking operation.

The steam cracking reaction is highly endothermic requires substantial energy to activate the reactant molecules. In steam cracking, radical chain reactions are the reaction pathway in which radicals or hydrogen atoms react with other radicals to form a series of products [18]. Energy costs typically account for 60 % of total production cost in the steam cracking. Additionally, coke deposition is a major drawback. Coking occurs on the reactor lowering heat transfer, increasing pressure drop through the reactor and causes corrosion. Consequently, commercial reactors must be periodically de-coked resulting in increased downtime.

1.2.2 Catalytic cracking

Propene is formed mainly as a by-product of fluid catalytic cracking (FCC) of gas oils in the refinery [19]. In FCC units, small amounts of ethene are produced but generally not

4

recovered, except in a few locations where large FCC units are adjacent to petrochemical facilities. This refinery process produces a mixture of butenes and butanes with very small amounts of butadiene as well. Whereas in Europe, refineries satisfy an average of only 20 % of the chemical industry's requirement of propene, in the United States they meet more than 40 % of the consumption demand [20]. In Western Europe propene demand is predicted to grow faster than that of ethene (3.7 % *vs.* 2.4 %) in the coming years [4], so additional propene sources are highly needed.

The conversion reactions of partially vaporized crude oil distillates in the FCC process occur mainly at elevated temperatures in the presence of a cracking catalyst. The acid catalysts first used in catalytic cracking were low alumina catalysts comprising amorphous solids composed of approximately 87% silica, (SiO_2), and 13 % alumina, (Al_2O_3) [21]. Later, high alumina catalysts containing 25 % alumina and 75 % silica were used [21]. However, this type of catalyst has largely been replaced by catalysts comprising crystalline aluminosilicates (zeolites) or molecular sieves [22]. The cracking reactions occurring at the active sites of the catalyst proceed via a carbenium ion mechanism that predominantly affects the formation of alkenes, isomeric components, and aromatics (the latter via intermediate formation of cycloalkenes) [23]. The formation of low-boiling alkenes, branched alkanes, and aromatics favours the production of gasoline with high octane levels. Overall FCC produces gasoline-boiling-range hydrocarbons, C_4 and lighter gas, and coke. Gaseous components are separated in a gas plant into fuel gas (containing hydrogen, methane, ethane, ethene, and hydrogen sulfide) and LPG fractions, i.e., propane–propene and butane–butene. The propene yield varies, depending on reaction conditions, but yields of 2–5 % based on feedstock [24].

1.2.3 Catalytic dehydrogenation

Alkane dehydrogenation, also a heterogeneous catalytic process, usually uses either a Cr_2O_3/Al_2O_3 or $Pt/Sn/Al_2O_3$ catalyst [25]. In this reaction, the alkane decomposes into alkene and H_2.

$$(C_2H_6 \rightarrow C_2H_4 + H_2) \qquad (\Delta H^o = 137 \text{ kJ/mol}) \qquad (1.1)$$

Dehydrogenation suffers the same difficulties as encountered in steam cracking and FCC, namely; high endothermicity of the reaction and catalyst deactivation due to coke formation. An additional difficulty encountered with dehydrogenation is the thermodynamic limitation of the reaction. Direct dehydrogenation is thermodynamically limited at low temperature making it impossible to achieve acceptable yields [26]. The endothermic reaction makes the process very energy intensive.

The limitation of the current alkene production methods is clear. All three of these processes are endothermic and require high temperatures to obtain acceptable yields. A number of alternative technologies have been investigated including: coupling direct alkane dehydrogenation with alkane combustion or hydrogen combustion to supply the required heat, membrane assisted direct dehydrogenation to separate hydrogen from the products to bypass the thermodynamic limitations and the other is the ODH reaction [5, 6]. Among these options ODH appears to be the simplest and the production of ethene by ODH does not suffer the same shortcoming as thermal cracking, FCC and direct dehydrogenation [7].

1.3 Oxidative methods for alkene production

Alkene production through oxidative routes, oxidative coupling and ODH has been recognized as a potentially attractive alternative since the presence of oxygen offers

6

thermodynamic advantages in equilibrium limited processes catalytic dehydrogenation and limits coking on the catalysts.

1.3.1 Oxidative dehydrogenation (ODH)

In view of the limitations of the dehydrogenation equilibrium, research has focused on ways to remove one of the products, namely hydrogen, by chemical methods. In this way, hydrogen is oxidized to water and hence there is no equilibrium limitation to the alkane conversion.

$$(C_2H_6 + 1/2\ O_2 \rightarrow C_2H_4 + H_2O) \qquad (\Delta H^\circ = -105\ kJ/mol) \qquad (1.2)$$

ODH, unlike steam cracking and direct dehydrogenation, is a thermodynamically favourable exothermic reaction making water and alkene. Additionally, ODH can operate at lower temperatures (250-550 ℃) than any of the aforementioned processes when using an appropriate catalyst [27]. The exothermic nature of the reaction together with the lower temperature requirement leads to substantial energy saving when using ODH as compared to direct dehydrogenation. In fact, the energy consumption is expected to be substantially less than any of the current alkene production methods due to their endothermic nature. Furthermore, the deposition of coke is largely eliminated due to the presence of oxygen, which can oxidize coke to form carbon dioxide preventing the routine de-coking procedures necessary in current commercial processes.

There are, however, a number of current challenges preventing ODH from being widely implemented. The difficulties inherent in ODH reactions revolve around selectivity control. Typically, alkane activation (which requires abstraction of the first hydrogen atom) is considered to be the rate limiting step. Unfortunately, at the temperatures required for alkane activation, the alkene product is easily oxidized. In these undesired

pathways, lattice, adsorbed or gas phase oxygen can be inserted into ethane or ethene to ultimately form combustion products.

$$(C_2H_6 + 5/2\ O_2 \rightarrow 2CO + 3H_2O) \qquad (\Delta H^\circ = -860\ kJ/mol) \qquad (1.3)$$

$$(C_2H_6 + 7/2\ O_2 \rightarrow 2CO_2 + 3H_2O) \qquad (\Delta H^\circ = -1430\ kJ/mol) \qquad (1.4)$$

However, the same oxygen species also oxidizes the alkane and alkene to CO_2 and other oxygenated products. Therefore, alkene selectivity remains a serious problem, as it limits the maximum achievable yield. Despite the research efforts invested to date the maximum yield in propane ODH reported in the literature is 30 %, which is unsatisfactory for commercialization [5]. Only the ODH of ethylbenzene to styrene has been commercialized to date [28]. Besides the challenge of finding a selective catalyst to perform the desired reaction, other issues such as safety in handling hydrocarbon-oxygen mixtures, have to be considered. Several approaches were taken to arrive to a well performing ODH catalyst. Basically three types of catalytic materials were investigated: redox catalysts, non-redox catalysts, noble metal (Pt, Rh, Ir) coated monolith [29]. The reaction mechanism over the different type of catalysts is also considered to be dependent on the materials used; Baerns proposed three types of mechanism being operative over different types of metal oxide materials [30].

1.3.1.1 Redox catalysis

Most literature data concerning redox catalysts are reported for transition metal containing materials. There are excellent reviews that summarize the work done on the ODH of low alkanes [5, 6]. Magnesia-supported vanadium (VMgO) has been a commonly studied catalyst. The reaction mechanism is typical of the Mars-van Krevelen description, where the transition metal oxide is reduced by the hydrocarbon in the first

step and it is reoxidized by gas-phase oxygen in a subsequent step [31]. Different alkanes showed different conversion, depending on the most labile C-H bond, showing that splitting the carbon-hydrogen bond is the rate-determining step. Over redox catalysts alkenes reacted generally faster than alkanes, except for ethene. Because of the higher activity of alkenes, finding a suitable redox catalyst seems to be an elusive goal [29]. In order to avoid contact of oxygen with the product alkene, reactor operation has been carried out in a cyclic mode, similar to the catalytic dehydrogenation in the CATOFIN process. CATOFIN dehydrogenation is a continuous process with cyclic reactor operation in which multiple reactors go through a controlled sequence of reaction reheat / regeneration from Abb Lummus Technology [32].

1.3.1.2 Non-redox catalysis

Primarily ODH of ethane was studied over non-redox type materials such as alkali promoted alkali-earth oxides and rare-earth oxides [33], often as an extension of the methane oxidative coupling reaction [34]. Propane ODH has been less studied over non-redox catalysts, but the best propene yields reported in the literature (~30 %) involve the use of non-redox materials [35]. Propane ODH over non-redox catalysts does not result propene exclusively, ethene is produced in large amounts as well. Although there are only a few studies of propane ODH conversion over non-redox type catalysts, it is apparent that gas-phase reactions contribute to alkene formation [36]. However, it is unclear from the literature whether catalytic or noncatalytic contributions to propane ODH conversion are more important, unlike in methane oxidative coupling where the role of catalytic and homogeneous reactions is well established [37]. Some authors explain their results of propane conversion to alkene only in terms of catalytic reactions, due to either weakly adsorbed or lattice oxygen, not affected by homogeneous gas-phase

9

contribution [39, 39], while others describe their results in terms of radical reactions in the gas-phase initiated on the catalyst, and radical-surface interactions [40].

1.3.1.3 Noble metal catalysis

Although noble metals are known to be very good combustion catalysts, under certain conditions, namely with a limited oxygen concentration and very low contact times, alkanes can be converted to alkene with high selectivity [41]. The product spectrum resembles the one over non-redox catalysts. The mechanism of this process is described by an initial full combustion of alkanes until total oxygen conversion, accompanied by heat generation and further thermal cracking of the remaining alkanes with the heat generated in the first step [42]. A different approach was taken when an effective dehydrogenation catalyst (Pt) was used in combination with a selective hydrogen combustion catalyst [Bi_2O_3] in order to perform the ODH in a continuous process [43]. In practice, Pt coated monoliths are used under very high flow conditions, contact times are as low as one millisecond [44].

1.3.2 Oxidative coupling

Oxidative coupling uses methane as feedstock and results in higher hydrocarbons, mostly ethene. It is difficult to break the C–H bond in methane; therefore it occurs at high temperatures (750-950 ºC). In the reaction, methane is activated heterogeneously on the catalyst surface, forming methyl radicals. These methyl radicals then couple in the gas phase to form ethane, which subsequently undergoes dehydrogenation to form ethene [45]. The yield of desired C_2 products is reduced by the nonselective reactions of methyl radicals with either surface or gas phase oxygen to produce carbon monoxide and carbon dioxide. The process could be economical when methane is available in abundance at extremely low cost, such as in Saudi Arabia. Since this process does not depend on crude

oil as a feed stock, research has continued in recent years, and it is possible that it may soon be commercialized. In the methane oxidative coupling reaction typically non-redox catalysts are employed. It is believed that the active (or activated) lattice oxygen abstracts the hydrogen from the methane molecule forming a surface hydroxyl [46]. It was first proposed in the methane coupling literature that the active sites of Li-promoted magnesia are the oxygen trapped by an electron hole next to a cation defect caused by stoichiometric Li^+ replacement for Mg^{2+} in the magnesia lattice [47]. This active site was commonly noted as $[Li^+O^-]$. When activating a methane molecule this active site transforms to $[Li^+OH^-]$. Regarding the regeneration of the active site there are two principally different propositions; in the mechanism proposed by Ito [47] the site is regenerated by dehydroxylation, that implies removal of lattice oxygen, while there are alternative propositions that do not require the costly removal of lattice oxygen [48].

An important element of the reaction mechanism in methane coupling is the release of radicals from the surface of the catalyst into the gas-phase. There is a vast body of evidence that radicals are released from the catalyst. These include mass-spectrometry, matrix isolation IR and matrix-isolation EPR [49]. Furthermore, a good correlation has been found between the EPR signals of the $[Li^+O^-]$ sites, the amount of radicals produced and the catalytic activity [47]. The kinetics of the methane coupling reaction has been described by mixed heterogeneous-homogeneous kinetic models [50]. These models included heterogeneous generation of radicals and some heterogeneous radical reactions. The kinetic parameters of the gas-phase reactions were generally provided by the extensive literature in combustion chemistry [51]. The role of homogeneous and heterogeneous reactions was critically discussed and the two contributions were rigorously defined [37]. A number of computational studies of the $[Li^+O^-]$ active sites and processes occurring on this site for methane coupling have been carried out [52, 53],

while extraction of hydrogen either from molecular hydrogen or methane on the active site has also been studied [54].

1.4 Limitations of ODH

The selective conversion of alkanes into alkenes is an important reaction both in fundamental research and in industrial applications. The ODH of alkanes produces usually a considerable amount of carbon oxide because of the low selectivity of the catalyst employed [55]. Although the process o f ODH has been widely implemented to solve the problem of an unfavourable equilibrium in the absence of oxygen, a high reaction temperature is necessary and poor selectivity to the alkanes has often resulted. The key aspect of this technology is, therefore, the development of catalysts capable of activating only the C-H bonds of the alkane molecule in a flow of oxygen. Designing the catalyst with a function to produce lower alkenes is a globally important issue to the petrochemical industries [56, 57].

In ODH reactions, oxygen or air has been used as oxidant because it is cheap and readily available. Substantial gains in process efficiency may be realized by consideration of less conventional oxidants such as N_2O and CO_2. A better understanding of each one of the above factors means a better comprehension of the overall process of alkane transformation, and hence an improved possibility of increasing the catalytic performance to make these processes more attractive to obtain the desired products.

There are still a number of current research challenges preventing ODH from becoming commercial. Due to these limitations, the only current commercial process that utilizes lower alkanes as a feedstock in an oxidation reaction is the selective oxidation of butane to maleic anhydride and acetic acid. It has been suggested that, due to the well established, highly efficient and fully depreciated existing plants, ODH will need to

achieve even higher selectivity than the current technologies. Currently, there are no commercial processes producing ethene from ethane using ODH and yields up to 70 % may be necessary to compete with the current technology [58, 59].

1.5 Catalytic systems of ODH for lower alkane

ODH of ethane as an alternative to the highly endothermic thermal pyrolysis has been the subject of many studies [60] in which a great variety of catalysts have been formulated and tested in the temperature range from 350 ℃ to 1000 ℃. Ethene can also be synthesized by auto-thermal ODH. Huff and Schmidt [61] reported the conversion of ethane in the presence of oxygen over Pt- and Rh- coated ceramic foam monoliths in an auto-thermal reactor at very low contact times in the order of milliseconds. Ducarme [62] studied the activity of the Co, Ni, and Fe oxides catalytic systems. Conversion of ethane was very low at the temperature range of 487 ℃ to 585 ℃ for Co, Ni and Fe, respectively. The specific activity sequence for the three metal oxides is Co > Ni > Fe. In the case of Co and Fe oxide catalyst, selectivity to ethene decreases when conversion increases with temperature. But this is not observed with Ni even at high temperature and this makes nickel the most attractive metal but yielded less promising results for ODH.

Other catalysts have been divided into two groups, high temperature catalysts and low temperature catalysts [63, 64] due to activity dependence on temperature; catalyst activity data are given in Table 1.1-1.3. At temperatures lower than 600 ℃, the ethene selectivity of 89 % and 91 % at ethane conversion of 19 % and 15 % were reported at 470 ℃ on B_2O_3/Al_2O_3 catalyst at 550 ℃ and on $K_2P_{1.2}Mo_{10}W_1Sb_1\text{-}Fe_1Cr_{0.5}Ce_{0.75}O_n$ catalysts respectively [63]. Catalysts that show high selectivity at higher temperatures (temperature higher than 600 ℃) generally do not contain easily reducible metals ions (such as V, Mo, W and Sb). The high temperature catalysts typically contain ions and oxides of group IA

or IIA metals (alkali or alkali earth metals) such as Li, K and Mg. Low temperature catalysts generally contain easily reducible transition metal oxides such as V, Mo and Nb.

1.5.1 High temperature catalysts

Catalysts containing ions and oxides of group IA and IIA metals such as Li and Mg are active and selective in the ODH of ethane. High selectivity can be achieved when chlorine compounds are added to the feed components or if catalysts are modified with halide compounds [65]. Kung [66] suggests that these catalysts may work in two ways: through a surface reaction or a homogeneous gas phase reaction. An ethane species adsorbs onto a surface oxygen atom before having a C-H bond cleaved to form a surface ethyl. This ethyl species can then further reacts with an oxygen molecule to form ethene. Alternatively, the adsorbed ethyl species can desorb from the surface into the gas phase. In this case, the catalyst mainly works as a radical initiator creating charged ethyl radicals through heterolytic C-H bond cleavage. The radicals then desorb from the surface and participate in homogeneous gas phase radical chemistry.

Table 1.1: High temperature catalytic system used for the ODH of ethane.

Catalysts Composition	Temp. (°C)	Conv. (%) C_2H_6	Selectivity (%)		Yield (%) C_2H_4	Ref. No.
			C_2H_4	CO_x		
$SrBi_3O_4Cl_3$	660	19.5	89.4	10.6	17.4	67
$KSr_2Bi_3O_4Cl_6$	660	45.3	92.2	7.8	41.8	67
Li-Mg-Cl	620	63	72.2	26.4	45.5	68
Sn/Li-Mg-Cl	620	78.7	71.6	26.1	56.4	68
Li-Mg	625	53.9	63.8	28.7	34.4	69
Li-Na-Mg	625	38.0	86.4	13.1	32.8	93
Li-Co-Mg	550	20.0	70.5	29.6	14.1	93

It has been reported, that these gas phase radical reactions can be more selective than the heterogeneous reactions leading to an increase in ethene selectivity as temperature is increased [67]. Large void fractions and high temperatures are employed to maximize the homogeneous gas phase reaction and it has been reported that packing a reactor with quartz wool can suppress this homogeneous reaction [68]. Over this class of catalysts, the yield improves with increasing temperature due to ethyl radical desorption into the gas phase to undergo homogeneous gas phase reactions with oxygen, ultimately forming ethene. It has been demonstrated by many researchers that the activity of Li-Mg base catalyst for the conversion of ethane to ethene can be further increased by treatment with chlorine [68, 69, 71]. The Li-Mg base catalyst has good activity at 620 ℃, giving 63 % ethane conversion without treatment with chlorine. After treating this catalyst with chlorine, its activity increased the ethane conversion 81.3 % with ethene selectivity 76 %, operating at a lower temperature (570 ℃) [69]. At higher temperatures the catalyst assisted homogeneous reactions play an important role [69]. Burch and Crabb [70] also show that a significant non-catalytic oxidation dehydrogenation occurs already at 600 ℃.

Kung [66] agreed that the achieving high activity and selectivity in high temperature ODH generally do not contain transition metals that reduce easily. As noted earlier, most widely studied catalyst is Li-MgO which abstracts hydrogen on Li^+-O^- defect sites to create alkyl radicals [69, 70]. High performance can be also achieved using Li/MgO catalysts promoted with dysprosium [71], with the highest ethene yields being achieved when the catalyst is doped with chlorine [72]. It has been suggested that halides are beneficial because they help to generate ethyl radical through heterolytic cleavage of the C-H bond. The ethyl radical reacts with surface oxygen atoms to form an ethoxide species which can decompose to ethene or desorbs into the gas phase and engage in free radical chemistry.

1.5.2 Low temperature catalysts

It should be noted that the work presented in this dissertation will deal with a low temperature ODH catalyst. The low temperature ODH catalysts contain easily reducible transition metal oxides (e.g. V, Mo, Sb, Nb) and are used in a wide array of selective oxidation reactions including ODH of ethane, propane, butane, 1-butene and ethylbenzene [73-84]. These catalysts operate by a Mars-van-Krevelen type redox mechanism. Vanadium and molybdenum oxides are the most studied active catalysts for ODH of lower alkanes and have been extensively investigated [78, 80, 81, 83-84]. Often, these metal oxides are deposited on the surface of another metal oxide (the support) such as SiO_2, TiO_2, Al_2O_3 or ZrO_2 resulting in improved activity, selectivity and mechanical strength. One well known catalyst is Mo/V/Nb oxide [85-87] and can be improved with the incorporation of tellurium [88]. Mo/V/Sb mixed oxides are also active and selective in ethane ODH achieving ethene selectivity of 80 % at ethane conversions of 65 % [89]. Vanadium pyrophosphate (VPO) catalyst has been extensively been studied by Cantuic [90] and others [91-94] for ODH reaction. VPO shows very low activity for ethane oxidation as compared to mixed metal oxide catalyst [90]. However, the VPO catalyst shows a high selectivity to oxygenated products such as acetic acid and acetaldehyde.

In fact, the choice of support is of fundamental importance in the design of effective oxidation catalysts. The choice of support can affect the metal oxide dispersion through the number and activity of support hydroxyl groups. Many authors have demonstrated that the nature of the support can influence the catalytic activity in selective oxidation reactions (including ODH) by over an order of magnitude [95-97]. By first constructing TiO_x, AlO_x and ZrO_x monolayers on a SiO_2 support and then anchoring isolated VO_3 species on these, turnover frequencies in methanol selective oxidation to formaldehyde were modified by a factor of 10. They suggest that the electronegativity of the V-O-V

16

bond influences the activity. By using supports with lower electronegativities, it is possible to increase the electron density of the oxygen atom making it more active [98].

Table 1.2: Low temperature catalytic system used for the ODH of ethane.

Catalyst Composition	Temp. (ºC)	Conv. (%) C_2H_6	Selectivity (%)		Yield (%) C_2H_4	Ref. Nos.
			C_2H_4	CO_x		
MoVNbTe600	400	27.3	94.9	5.1	25.9	73
MoVTe-600	400	2.7	48.2	51.8	1.3	73
MoVNbTe	400	35.6	93.6	6.5	33.3	79
MoVNbTe-Si	400	18.0	95.4	4.6	17.2	79
MoO_x	440	0.13	52.1	47.9	0.1	80
$MoVO_x$	440	9.4	57.9	42.1	5.4	80
$MoVTeNbO_x$	440	65.0	91.9	7.1	59.7	80
5% V-TiO_2	550	8.0	42.5	56.8	3.4	82
5% V-Nb_2O_5	550	8.0	39.6	60.3	3.2	82
5% V_2O_5/SiO_2	530	5.6	62.0	29.3	3.5	84
2% V_2O_5/SiO_2	538	30.0	22.0	3.0	6.6	85
V_2O_5/Al_2O_3+K	530	6.2	39.1	34.7	2.4	86
$Mg_2V_2O_7$	571	6.5	25.0	75.0	1.6	99
VMgO	560	21.0	22.0	88.0	4.6	99
MoVWMn	400	58.0	58.0	42.0	33.6	101
LiVSb	500	10.0	50.0	50.0	5.0	102

1.5.3 Metal oxide catalysts

Most of the previous literature discusses the use of mixed metal oxide catalysts for the ODH of lower alkanes [99-103]. The most commonly used mixed oxides catalysts are shown in Table 1.3. For the mixed metal catalyst, mixed supports (consisting of more than one support) can provide benefits beyond those of using single supports [104]. In particular, a silica-titanium mixed oxide support is able to preserve the catalytic active

sites of a [VOx/TiO$_2$] or [MoOx/TiO$_2$] catalyst while gaining the mechanical and thermal stability of silica based catalysts [105]. These materials also possess new catalytic active sites [106]. These types of catalysts often have enhanced acidity due to the creation of unique Si-O-Ti sites not present on the individual oxides. Additionally, it has been demonstrated that the typical octahedral coordination state of the anatase form of TiO$_2$ can be accompanied by small tetrahedral sites when using a mixed silica-titanium oxide [107, 108]. These new catalytic sites can lead to improved chemical properties and active sites useful for catalytic reactions. Other benefits, not observed with single metal oxides, are also possible such as higher surface areas and higher active metal dispersions [109].

Table 1.3: The catalytic system used for the ODH of ethane.

Catalysts Composition	Temp. (ºC)	Conv. (%) C_2H_6	Selectivity (%) C_2H_4	Selectivity (%) CO_x	Yield (%) C_2H_4	Ref. Nos.
MoTeNb	420	0.2	10.3	89.7	0.1	76
MoVTeNb	380	6.3	95.9	4.1	6.1	76
MoVTeNb	380	29.0	94.5	5.6	27.4	76
MoVTeNb	380	12.5	94.5	5.6	11.8	76
MVNb- A-600	380	9.5	73.0	27.0	6.9	77
MVTe- A-600	380	39.0	93.0	7.0	36.3	77
MVTNb-A-600	380	10.0	96.0	4.0	9.6	77
Mo/V-M-Al	580	33.8	70.7	29.3	23.9	78
Mo/V	580	21.2	56.4	43.5	11.9	78
MoVNbTe-γAl	400	23.9	93.6	6.4	22.4	79
MoVNbTe-αAl	400	29.5	95.0	5.0	28.1	79
MoVNbTe-Ni	400	18.8	93.2	6.8	17.5	79
MoVNbTe-Zr	400	14.2	93.6	6.3	13.3	79

In addition to using different support materials, the surface characteristics of a catalyst can be tuned by the addition of small quantities of another metal as a promoter. These promoters affect the surface properties of a catalyst by creating active sites, improving

dispersion, modifying lattice oxygen diffusivity, and adjusting the reducibility of the metal cation [92]. Hence, the surface properties of a catalyst can be "tuned" by the addition of promoter metals and extensively investigated on silica-titanium supported molybdenum catalysts [86, 110-111].

Mo (V) is considered to be the active site in this reaction but the electronic nature of the coordinated oxygen atoms is likely the underlying cause of its activity [92]. Electron spin resonance experiments showed that the presence of potassium alters the electronic structure of the surface Mo (V) species, lowering molybdenum's coordination sphere from 6 to 5. This change of coordination creates highly distorted molybdenum species and may be responsible for the observed increase in propane ODH reactivity [112].

Though it is understood how these structural changes affect the oxidation/reduction cycle, their influence on the nature of oxygen species during reaction remains unclear. Other work has focused on the addition of halide promoters to silica-titanium supported molybdenum catalysts [78, 80, 85, 111]. Post-reduction X-ray photoelectron spectroscopy studies demonstrated that the addition of chlorine strongly influenced the reducibility of surface molybdenum oxide species. In the presence of chlorine, propane was only able to reduce molybdenum to Mo (V) whereas in the absence of chlorine, propane reduced some molybdenum to Mo (IV) [111]. Steady state reaction experiments showed improved alkane conversion and alkene yield in ODH reactions over chlorine doped catalysts [113].

Using V_2O_5 Le Bars [83] suggested the improved selectivity seems to be a characteristic of the reduced surface of the mixed oxide catalyst. However, it can hardly be maintained under the reaction conditions because of oxygen diffusion from the bulk. At the steady state, the surface of V_2O_5 is close to being fully oxidized and does not retain any strong

acid sites. To enhance the ethene selectivity, an optimum regeneration of the surface, acidic properties, and a rapid removal of the ethene from the reaction zone are claimed to be essential [114]. Vanadium pentaoxide supported on silica or alumina [64-67] is reported to be an active functionalization element of ethane molecule relatively at higher temperature.

Table 1.4: Catalytic performance of the different catalytic systems

	Catalyts	Temperature (ºC)	Conv.-C_2H_6 (Min-Max. %)	Sel-C_2H_4 (Min-Max. %)	Ref.
A	Li-Mg-Cl	580 – 660	38 – 80	64 - 80	[69,70,93]
B	Mo-V/Support	530 – 550	10 – 21	56 - 58	[78,80,81]
C	Mo-V -Nb-Te	380 – 440	6 – 2	90 - 95	[73,76,77,79]
D	V_2O_5/Support	530 – 550	5 – 30	22 - 62	[72,84,85,86]

1.6 ODH reaction mechanism for lower alkanes

Mainly there are three types of initial mechanism for the primary reaction of the ODH of alkanes on metal oxide catalysts that have been considered in the literature [99]. These are based on the type of oxygen species involved in alkane oxidation which is illustrated in Fig.1.1.

(A)   In the redox mechanism, the oxygen of the metal oxide takes part in the reaction by abstraction and oxidation of the hydrogen from the hydrocarbon. The OH groups being formed in this way are then removed from the surface by dehydration. The catalyst is subsequently reoxidized by oxygen from the gas phase.

(B)   In this mechanism, oxygen participates via its adsorbed state, hydrogen is abstracted forming as OH group on the catalyst surface which is removed by

20

dehydration. The active surface oxygen in then restored by oxygen adsorption from the gas phase.

(C)   In this mechanism, it is assumed that strongly bound lattice oxygen abstracts hydrogen, which is, removed from the surface by hydration with gas-phase oxygen.

C_nH_{2n+2}

A) Redox mechanism

$C_nH_{2n+1} + MO_xH$

MO_x

$C_nH_{2n} + MO_{x-1} + H_2O$

$0.5\ O_2$

B) Activation by adsorbed

oxygen

$C_nH_{2n+1} + MO_x\text{-OH}$

$MO_x - O(ad.)$

$C_nH_{2n} + MO_x\text{-OH}$

$0.5\ O_2$

C) Activation by lattice oxygen

(No redox mechanism)

$C_nH_{2n+1} + MO_xH$

MO_x

$0.5\ O_2$

$C_nH_{2n} + MO_x + H_2O$
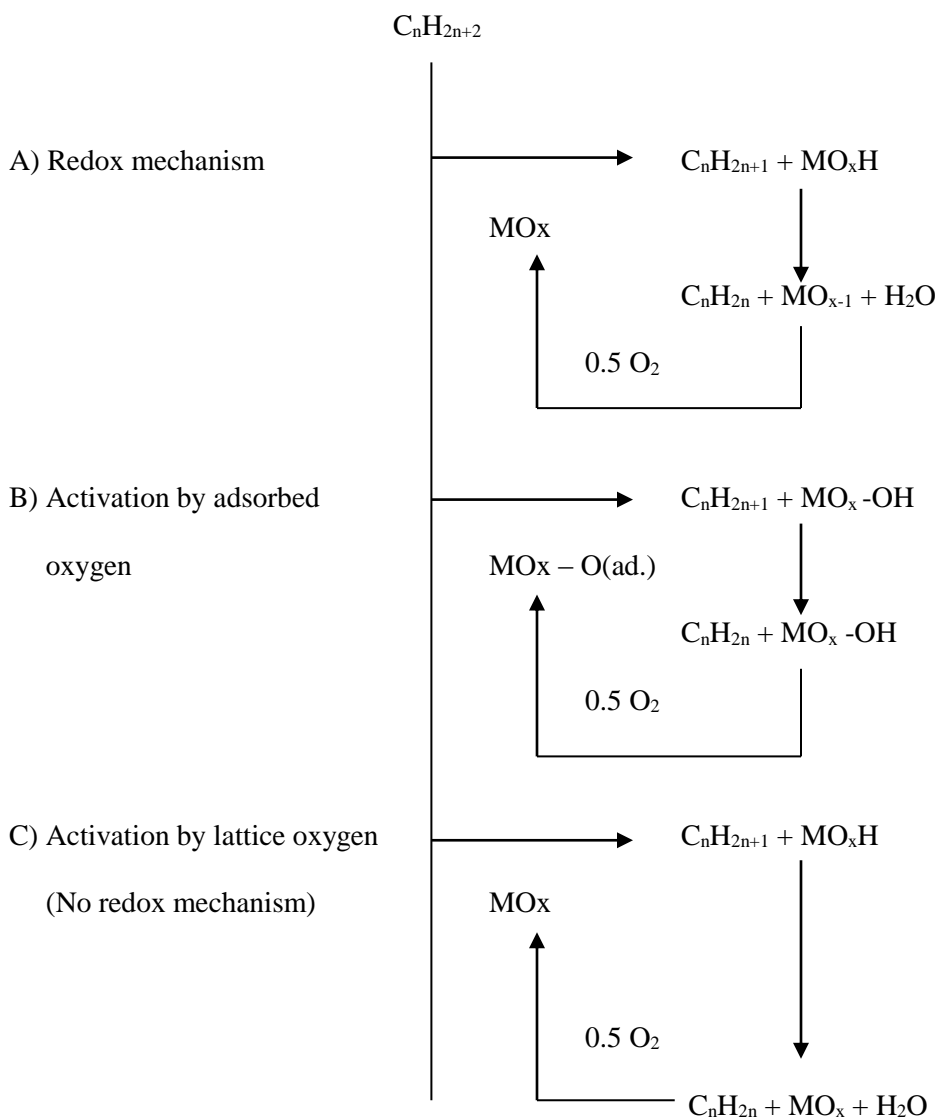
Fig.1.1: Initial mechanism for the ODH of alkanes on metal oxide catalyst [68].

1.7 ODH ethane reaction mechanism

The reaction mechanism proposed in the literature for ODH of ethane [64, 96, 100] are based on consecutive and parallel reactions. These proposed mechanism and the associated kinetic modeling have been mainly applied to Mo and V based catalysts. The generally accepted mechanism for the oxidation of a hydrocarbon over a reducible metal oxide catalyst is the Mars-van Krevelen mechanism. Kung [7] suggested that rupture of the first C-H bond is generally slowest step in the ODH reaction, and that the activation of the C-H bond by a metal oxide leads to the formation of alkyl or alkoxide species. However, the high reactivity of surface intermediates has made direct observation of these species difficult and the detailed reaction mechanism for light alkane oxidation remains elusive. The ethane molecule is adsorbed on the catalyst surface in the form of an ethoxide species, as proposed for the case of V^{5+} by Oyama [96] or for the case of Mo^{6+} by Thornsteinson [64] and by Lin [101] for the Ni, Cu, Fe metal oxides catalysts. Experimental data suggest two types of pathways for ODHE (oxidative dehydrogenation of ethane) [115]:

(A) C_2H_6 reacts with surface oxides to form a metal-ethoxide and a surface hydroxyl,

$$(C_2H_6 + 2M\text{–}O \longrightarrow C_2H_5\text{–}O\text{–}M + M\text{–}O\text{–}H) \qquad (1.5)$$

The metal ethoxide may then undergo two possible reactions: α- hydrogen abstraction or β- hydrogen abstraction, which leads to an aldehyde or C_2H_4, respectively.

$$(CH_3CH_2\text{–}O\text{–}M \longrightarrow CH_3\text{–}CHO + M\text{–}H) \qquad (1.6)$$

$$(CH_3CH_2\text{–}O\text{–}M \longrightarrow CH_2=CH_2 + M\text{–}O\text{–}H) \qquad (1.7)$$

22
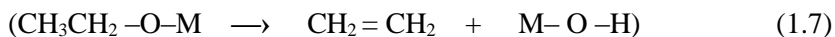
(B) C_2H_6 reacts with surface oxides to form a ethyl-metal complex followed by β- hydrogen elimination to give C_2H_4 and a metal-hydride site,

$$(C_2H_6 + M\text{–}O + M \longrightarrow C_2H_5\text{–}M + M\text{–}O\text{–}H) \qquad (1.8)$$

$$(C_2H_5 - M \longrightarrow C_2H_4 + M\text{–}H) \qquad (1.9)$$
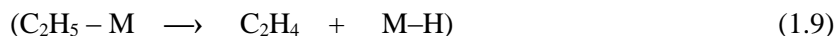
After the reactions in either pathways (A) or (B) take place, surface hydroxyl and/or surface hydrogen may undergo the following reactions to produce a reduced metal site and water.

$$(M\text{-}H + M\text{–}O \longrightarrow M + M\text{–}O\text{–}H) \qquad (1.10)$$

$$(M\text{-}H + M\text{–}O\text{–}H \longrightarrow 2M + H_2O) \qquad (1.11)$$

$$(2M\text{–}O\text{–}H \longrightarrow M - O + M + H_2O) \qquad (1.12)$$
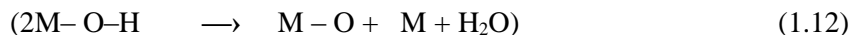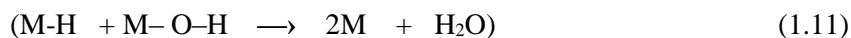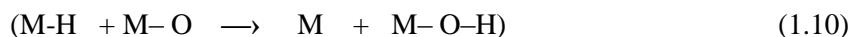
Oxidation of the reduced metal site by O_2 then regenerates the oxidized metal site, completing the catalytic cycle.

$$(M + \tfrac{1}{2}\,O_2 \longrightarrow M\text{–}O) \qquad (1.13)$$

Thornsteinson [64] suggested schemes for the interaction of ethane with the surface of the catalyst to form the ethoxy complex followed by formation of ethene. In preparation step, the Mo^{6+} atoms are reduced to Mo^{5+} species, treatment with ethane causes Mo^{5+} to disproportionate into Mo^{4+} and Mo^{6+}. Ethane reacts with the oxoligand on Mo^{6+} giving an ethoxyhydroxyl species. The ethoxy species releases ethene and ultimately Mo^{4+} is produced. Vanadium and niobium help the re-oxidation of Mo^{4+} to Mo^{6+} which is the species acting as a catalyst for the ODH of ethane into ethene. A hydroxyl ethoxy molybdenum is formed and that is decomposes into ethene, water and Mo^{4+}.

1.8 Mars-van Krevelen mechanism

Ethane ODH is typically considered to occur by a network of consecutive and parallel reactions as shown in Fig. 1.2 [116]. The three primary reactions that occur are (1) ODH of ethane, (2) the undesired direct combustion of ethane and (3) the undesired secondary combustion of ethene. Many studies have investigated the reaction mechanism in propane and ethane ODH [117-122]. Burch and others have been demonstrated that the reducibility of the active metal is closely related to catalytic activity [123-125]. It has also been suggested that the ODH reaction rates more closely correlate with UV-Vis adsorption edge energy which indicates the ease that lattice oxygen atoms transfer electron to the metal center [126]. These results suggest that the reduction of the catalyst is involved in the ODH mechanism. Steady State Transient Isotopic Kinetic Analysis (SSTIKA) has been used to probe the ODH reaction mechanism. In SSITKA, a reaction is allowed to reach steady state. Then the isotopic composition of one of the reactants is abruptly switched while maintaining the concentration of the gas. For instance, a feed containing 5 % ^{16}O would be abruptly changed to 5 % ^{18}O. The resulting relaxation and evolution of products containing ^{18}O atoms provides information about the reaction mechanism and can be monitored with a mass spectrometer.
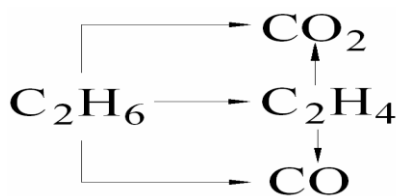
Fig. 1.2: ODH reaction scheme.

Similar results have been demonstrated for vanadium catalysts as well as it is now widely accepted that the ODH of lower alkanes by transition metal catalysts occurs by a Mars-van Krevelen redox mechanism. During oxidation, the catalyst surface is reduced as

24

lattice oxygen atoms activate ethane molecules; ultimately forming alkenes (Fig.1.3). First ethane must adsorb to a surface oxygen atom (O*) and a C-H bond must be cleaved forming an alkyl intermediate and a hydroxyl group on the catalyst surface. This initial cleavage of the ethane C-H bond is widely considered the rate limiting step and the literature consistently shows that consumption rates are first order in ethane concentration [119, 120]. The adsorbed alkyl species, which is adsorbed onto oxygen atom, then loses a second hydrogen atom forming ethene and another hydroxyl group on the catalyst surface. Finally, two hydroxyl groups combine to form water and a lattice vacancy (V*) where there was initially an oxygen atom. Gas phase oxygen then adsorbs to the surface and undergoes a series of electron transfer processes before being incorporated back into the lattice and restoring the initial oxidation state of the catalyst, thus completing the redox cycle given in Fig. 1.3 [127].

$C_nH_{2n+2(ads)}$ $\quad$ $C_nH_{2n} + H_2O$ $\qquad$ $O_{2(gas)}$

$C_nH_{2n+2(ads)} + O_l$ $\qquad$ $O_{2(surf)}^-$
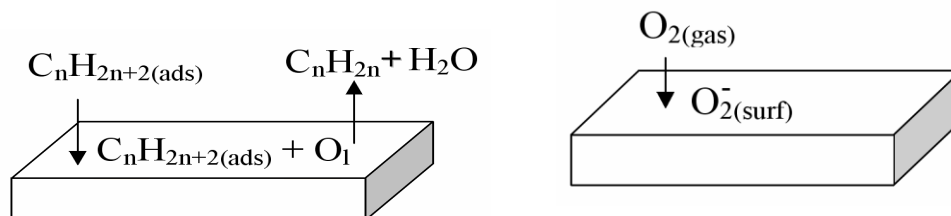
Fig. 1.3: Proposed Mars van Krevelen redox mechanism. Left- catalyst reduction by alkane. Right-catalyst re-oxidation with O_2.

$$(\tfrac{1}{2} O_2 + Z \quad \longrightarrow \quad [O- Z]) \qquad (1.14)$$

$$(C_nH_{2n+2} + [O\text{-}Z] \longrightarrow \quad C_nH_{2n+1} + [OH] - Z) \qquad (1.15)$$

$$(C_nH_{2n+1} + [O\text{-}H] \longrightarrow \quad C_nH_{2n+1} + [OH] - Z\ M- O) \qquad (1.16)$$

$$(2[OH] - Z \quad \longrightarrow \quad H_2O + [O\text{-}Z] + Z) \qquad (1.17)$$
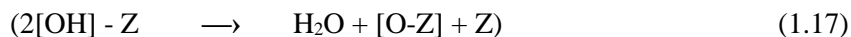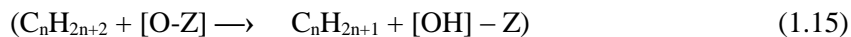
Mars-van Krevelen redox mechanism over reducible metal oxide catalysts shows the formation of an OH group and a carbanion, where Z is a vacant site.

When in equilibrium with the gas phase, the surface is populated by short-lived oxygen species $(O_2)^-$ and O^- that can affect catalyst performance (Fig. 1.4). The strongly electrophilic species, O^{2-} and O^-, are considered to be responsible for the unselective complete oxidation of lower alkanes leading to partial combustion products, CO and CO_2, while nucleophilic species of metal oxo (M=O) with lattice oxygen anions is believed to selectively produce alkene, though the lattice oxygen could participate in the partial combustion of ethene [126, 128]. The nature of these oxygen species depends on reaction conditions, degree of catalyst surface reduction, the counter metal oxide cation and the structure of surface species but the exact relationship is difficult to characterize [129].
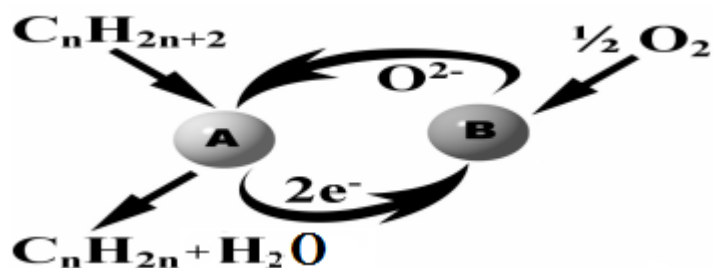
Fig. 1.4: Electron transfer processes during catalyst re-oxidation [128].

Chen and co-workers [130] have explored the ODH reaction mechanism on MoO_x/ZrO_2 catalysts and determined a number of important points. Lattice oxygen is required for ODH as evidenced by the slow incorporation of (^{18}O) in the reaction products after an isotopic switch. C-H bond activation is irreversible as evidenced by the lack of C_3H_8 with mixed deuterium-hydrogen content during ODH with a C_3H_8/C_3D_8 mixture. Kinetic isotope effects were observed during propane dehydrogenation and propene combustion suggesting that C-H bond dissociation is a kinetically relevant reaction step. These data suggest a redox type mechanism where lattice oxygen atoms react with the alkane to produce an alkene. The catalyst is reduced during this process and gas phase oxygen must then reoxidize the catalyst in a separate step.

1.9 Summary of the work described in this thesis

It is clear from the preceding literature review that MoV oxide catalysts are effective for ethane ODH. Hence, in the present study the synthesis of vanadium mixed oxide catalysts has been investigated. MoV oxide catalysts have prepared under modified well-controlled preparation conditions and are further studied by adding of several different supports.

In summary, Chapter 1 discusses motivation for research to obtain lower alkenes, mainly on vanadium based catalysts. Following this introduction, Chapter 2 presents the experimental methods which are mainly focused on the catalyst preparation, catalyst characterization, and catalytic reaction procedure and data analysis. Results of metal ratios (MoV) variation and reaction variables on MoV oxide catalysts have been discussed in Chapter 3. An influence of the addition of oxalic acid in the catalyst preparation and its effect on the activity has been studied and discussed in Chapter 4. Chapter 5 discusses the results obtained from the effect of various supports on the activity of the catalyst and the support loading concentration on the catalyst activity. Chapter 6 concludes all the investigation made on catalytic systems in the present study with proposed future work followed by Appendix 1-5 with detailed description of reactor system, GC configuration with data evaluation methods.

1.10 References

[1] S. Zehnder, *Hydrocarb. Process*. **77** (2) (1998) 59.

[2] H. A. Winttcoff, *Chem. Tech.* **48** (1) (1990) 20.

[3] G. Centi, F. Trifiro, J. R. Enber, V. M. Franchetti, *Chem. Rev.***55** (1988) 88.

[4] Petrochemistry Activity Review http://www.cefic.org, (1999-2000).

[5] J. G. Speight, *Chemistry and Technology of Petroleum* (4th Ed.). CRC Press. ISBN 0-8493-9067-2, (2006).

[6] F. Cavani, F. Trifiro, *Catal. Today* **24** (3) (1995) 307.

[7] H. H. Kung, *Adv. Catal.* **40** (1994) 1.

[8] C. Mazzocchia, C. Aboumrad, C. Diagne, E. Tempesri, J. M. Herrmann, G. Thomas, *Catal. Lett.* **10** (3-4) (1991) 191.

[9] A. A. Lemonidou, G. J. Tjatjopoulos, I. A. Vasalos, *Catal. Today* **45** (1-4) (1998) 65.

[10] M. A. Chaar, D. Patel, M. C. Kung, H. H. Kung, *J. Catal.* **105** (2) (1987) 483.

[11] H. H. Kung, M. A. Chaar, US Patent **4777319**. A1. (1988).

[12] M. A. Chaar, M. C. Kung, I. Jahan, H. H. Kung, *J. Catal.* **109** (2) (1987) 463.

[13] P. M. Michalakos, D. Patel, H. H. Kung, *J. Catal.* **140** (1) (1993) 226.

[14] T. C. Watling, G. Deo, K. Seshan, I. E. Wachs, J. A. Lercher, *Catal. Today* **28** (1) (1996) 139.

[15] Sixth Ed. Wiley-VHC, Weinheim, *Ullmann's Encyclopedia of Ind. Chem.*, (2002).

[16] Online Ed. Wiley-VHC, Weinheim, *Kirk-Othmer Encycl. Chem. Tech*., (2002).

[17] M. M. Bhasin, J. H. Mccain, B. V. Vora, T. Imai, P. R. Pujado, *Appl. Catal. A: Gen.* **221** (1-2) (2001) 397.

[18] E. Ranzi, T. Faravelli, P. Gaffuri, G. C. Pennati, A. Sugaro, *Comb. Sci. Tech.* **100** (1-6) (1994) 299.

[19] T. Chan, K. Sundaram, *AIChE Spring Meeting 2nd International Conference in Refinery Processing*, *Houston*, March 14-18, (1999).

[20] M. Rama Rao, D. Soni, G. M. Sieli, D. Bhattacharyya, *Hydrocarbon Processing* **90** (2) (2011) 45.

[21] C. H. Yang, H. H. Shan, J. S. Zheng, G. L. Niu, J. F. Zhang, *Am. Chem. Soc.*, *Div. Fuel Chem.* **48** (2) (2003) 702.

[22] J. G. Speight, B. Ozum, Petroleum Refining Process, Marcel Dekker, Inc. <u>ISBN: 0-8248-0599-8</u> (2000).

[23] J. Jakkula, *European Refining Technology Conference*, London, November (1997).

[24] K. Chen, E. Iglesia, A. T. Bell, *J. Phys. Chem. B* **105** (3) (2001) 646.

[25] D. Sanfilippo, F. Buonomo, G. Fusco, M. Lupieri, I. Miracca, *Chem. Eng. Sci*. **47** (1992) 2313.

[26] O. A. Barias, A. Holmen, E. A. Blekkan, *J. Catal*. **158** (1996) 1.

[27] J. Houzvicka, J. G. Nienhuis, S. Hansildaar, V. Ponec, *Appl. Catal. A* **165** (1997) 443.

[28] T. Tagawa, T. Hattori, Y. Murakami, *J. Catal.* **75** (1982) 66.

[29] F. Cavani, F. Trifiro, *Catal. Today* **51** (1999) 561.

[30] M. Baerns, O. Buyevskaya, *Catal. Today* **45** (1998) 13.

[31] A. Pantazidis, A. Burrows, C. J. Kiely, C. Mirodatos, *J. Catal.* **177** (1998) 325.

[32] G. J. Robert, R. J. Feldmen, E. Cemal, F. M. Dautzengerg, US Patent **5510557** (1996).

[33] G. E. Keller, M. M. Bhasin, *J. Catal* .**9** (1982) 73.

[34] P. G. Hinson, A. Clearfield, J. H. Lunsford, *J. Soc. Chem. Commun.* **20** (1991) 1430.

[35] M. V. Landau, M. L. Kaliya, M. Herskowitz, P. F. Oosterkamp, P. S. G. Boque *Chemtech*, **26** (2) (1996), 24.

[36] L. Leveles, K. Seshan, J.A. Lercher, L. Lefferts, *J. Catal.* **218** (2003) 307.

[37] M. Hatano, P. G. Hinson, K. S. Vines, J. H. Lunsford, *J. Catal.* **124** (1990) 557.

[38] W. D. Zhang, X. P. Zhou, D. L. Tang, H. L. Wan, K. Tsai, *Catal. Lett.* **23** (1) (1994) 103.

[39] Q. J. Ge, B. Zhaorigetu, C. Y. Yu, W. Z. Li, H. Y. Xu, *Catal. Lett.* **68** (1) (2000) 59.

[40] M. Y. Sinev, L. Y. Margolis, V. Y. Bychkov, V. N. Korchak, *Stud. Surf. Sci. Catal.* **110** (1997) 327.

[41] D. Mansuy, J. F. Bartoli, P. Battioni, D. K. Lyon, R. G. Finke, *J.Am. Chem.Soc.***113** (1991) 7222.

[42] A. Beretta, I. Piovesan, P. Forzatti, *J. Catal.* **184** (2) (1999) 455.

[43] R. K. Grasselli, D. L. Stern, J. G. Tsikoyiannis, *Appl. Catal. A: Gen.* **189** (1) (1999) 9.

[44] L. D. Schmidt, *Stud. Surf. Sci. Catal.* **130** (2000) 61.

[45] Y. Amenomiya, V. I. Birss, M. Goledzinowski, J. Galuszka, A. R. Sanger, *Catal. Rev. Sci. Eng.* **32** (1990) 163.

[46] P. M. Couwenberg, Q. Chen, G. B. Marin, *Ind. Eng. Chem. Res*. **35** (1996) 3999.

[47] H. G. Willium, Y. S. Su, Y. Y. Jackie, *J. Catal.* **218** (2) (2003) 321.

[48] T. Ito, J. X. Wang, C. H. Lin, J. H. Lunsford, *J. Am. Chem. Soc.* **107** (1985) 5062.

[49] M. A. Johnson, E. V. Stefanovich, T. N. Truong, *J. Phys. Chem. B* **101** (16) (1997) 3196.

[50] D. J. Driscoll, W. T. Martir, J. X. Wang, J. H. Lunsford, *Adv. Catal.* **35** (1987) 139.

[51] C. Shi, M. Hatano, J. H. Lunsford, *Catal. Today* **13** (2-3) (1992) 191.

[52] P. Baranek, G. Pinarello, C. Pisani, R. Dovesi, *Phys. Chem. Chem. Phys.* **2** (17) (2000) 3893.

[53] U. Birkenheuer, F. Cora, R. Millini, G. Perego, R. Dovesi, *Surf. Sci.* **373** (2-3) (1997) 393.

[54] L. Ackermann, G. D. Gale, C. R. A. Catlow, *J. Phys. Chem. B* **101** (48) (1997) 10028.

[55] M. B. Ward, M. J. Lin, J. H. Lunsford, *J. Catal.* **50** (2) (1977) 306.

[56] H. A. Winttcoff, *Chem. Tech.* **48** (1) (1990) 20.

[57] J. F. Roth, *Chem. Tech.* **357** (6) (1991) 21.

[58] A. Erdohyli, F. Solymosi, *Appl. Catal.* **74** (1991) 11.

[59] G. Colorio, J. C. Vedrine, A. Auroux, B. Bonnetot, *Appl. Catal.* **137** (1991) 55.

[60] C. Yokoyama, S. S. Bharadwaj, L. D. Schmidt, *Catal. Lett.* **38** (1996) 181.

[61] M. Huff, L. D. Schmidt, *J. Phys. Chem.* **11815** (1993) 97.

[62] V. Ducarme, A. Thalib, G. A. Martin, *Catal. Today* **24** (1995) 335.

[63] F. Cavani, M. Koutyrev, F. Trifiro, *Catal. Today* **28** (1996) 319.

[64] E. Thorsteinson, T. P. Vilson, F. G. Young, P. H. Kasai, *J. Catal.* **52** (1978) 116.

[65] S. Fuchs, L. Leveles, K. Seshan, L. Lefferts, A. Lemonidou, J. A. Lercher, *Top. Catal*. **15** (2001) 169.

[66] H. H. Kung, M. C. Kung, *Appl. Catal.* **157** (1-2) (1997) 105.

[67] W. Ueda, Sui-Wen Lin, I. Tohmoto, *Catal. Today* **49** (1997) 241.

[68] S. J. Conway, D. J. Wang, J. H. Lunsford, *Appl. Catal. A: Gen.* **79** (1991) L1-L5.

[69] E. Morales, J. Lunsford, *J. Catal.* **118** (1989) 255.

[70] R. Burch, E. M. Crabb, *Appl. Catal. A: Gen.* **79** (1993) 49.

[71] E. A. Mamedov, V. Crtes Coberan, *Appl. Catal. A* **127** (1995) 140.

[72] M. Panizza, C. Resini, F. Raccoli, G. Busca, R. Catani, S. Rossini, *J. Chem. Engg.* **93** (2003) 181.

[73] J. M. Lopez Nieto, P. Botella, A. Concepcion, A. Dejoz, M. I. Vazquez, *Catal. Today* **91-92** (2004) 241.

[74] X. Zhang, J. Liue, Y. Jing, Y. Xie, *Appl. Catal. A* **240** (2003) 143.

[75] E. Ranzi, T. Faravelli, P. Gaffuri, G. C. Pennati, A. Sogaro, *Comb. Sci. Tech.* **100** (1-6) (1994) 299.

[76] P. Botella, J. M. Lopez Nieto, B. Solsona, A. Misfud, F. Marquez, *J. Catal.* **225** (2004) 428.

[77] P. Botella, J. M. Lopez Nieto, A. Dejoz, M. I. Vazquez, A. Martinez-Arias, *Catal. Today* **142** (2009) 272.

[78] B. Solsona, T. Gracia, P. Concepcion, J. M. Lopez Nieto, M. I. Vazquez, M. T. Navara, *Catal. Today* **117** (2006) 228.

[79] M. Baerns, O. Buyevskaya, *Catal. Today* **45** (1998) 13.

[80] Q. Xie, L. Chen, W. Weng, H. Wan, *J. Mol. Catal. A* **240** (2005) 191.

[81] N. Haddad, E. Bordes-Richard, L. Hilaire, A. Barama, *Catal. Today* **126** (2007) 256.

[82] M. A. Banares, M. V. Martinez-Huerta, X. Gao, J. L. G. Fierro, I. E. Wachs, *Catal. Today* **61** (2000) 295.

[83] J. Le. Bars, A. Auroux, J. C. Vedrine, M. Baerns, Stud. *Surf. Sci. Catal.* **72** (1992) 181.

[84] M. A. Banares, X. Gao, J. L. G. Fierro, I. E. Wachs, R. K. Oyama, J. ELyons, *Stud. Surf. Sci.Catal.* **110** (1997) 295.

[85] A. Erdohelyi, F. Solymosi, *J. Catal.* **123** (1989) 31.

[86] A. Galli, J. M. Lopez Nieto, A. Dejoz, M. I. Vazquez, *Catal. Lett.* **34** (1995) 51.

[87] E. Morales, J. Lunsford, *J. Catal.* **118** (1989) 255.

[88] J. M. Lopez Nieto, P. Botella, M. I. Vázquez, A. Dejoz, *WO Patent 03/064035* (2003).

[89] M. Merzouki, B. Taouk, L. Tessier, E. Bordes, P. Courtine, *Proc. Cong. Catal.* **10** (1995)753.

[90] R. Lopez, N. Godjayaeva, V. Corberan, J. L. G. Fierro, E. Mamodov, *Appl.Catal.* **124** (1995) 281.

[91] A. Eastman, J. Kolts, US Patent **4370359** (1983).

[92] A. Corma, F. Melo, L. Sauvanaud, and F. Ortega, *Appl. Catal. A: Gen.***265** (2004) 195–206.

[93] G. J. Hutchings, R. Olier, M. T. Sananes, J. C. Volta, *Stud. Surf. Sci. Catal.* **82** (1994) 213.

[94] J. C. Volta, *Catal. Today* **32** (1996) 29.

[95] B. Solsona, M. I. Vazquez, F. Ivras, P. Concepcion, J. M. Lopez Nieto, *J. Catal.* **252** (2007) 271.

[96] S. T. Oyama, *J. Catal.* **128** (1995) 210.

[97] T. Ito, J. X. Wang, C. H. Lin, J. H. Lunsford, *J. Am.Chem. Soc.* **107** (1985) 5062.

[98] A. S. Craig, A. M. Gaffanay, R. Song, US Patent **20100256432** A1 (2009).

[99] P. M. Michalakos, M. C. Kung, I. Jahan, H. H Kung, *J. Catal.* **140** (1993) 226.

[100] S. A. Driscoll, D. K. Gardner, U. S. Ozkan, *J. Catal.* **147** (2) (1994) 379.

[101] X. Lin, K. R. Poeppelmeir, E. Weitz, *Appl. Catal. A: Gen.* **381** (1-2) (2010) 114.

[102] L. Yuan, S. Bhatt, G. Beaucage,V. V. Guliants, S. Mamedov, R.S. Soman, *J. Phys. Chem. B* **109** (49) (2005) 23250.

[103] R. Malathi, P. M. Rao, R. P. Viswanath, *Stud. Surf. Sci. Catal.* **113** (1998) 957.

[104] R. B. Watson, U. S. Ozkan, *J. Catal.* **191** (1) (2000) 12.

[105] R. B. Watson, U. S. Ozkan, J. Catal. **208** (2002) 124.

[106] R. B. Watson, U. S. Ozkan, *J. Mol. Catal. Chem.* **194** (1-2) (2003) 115.

[107] E. V. Kondratenko, M. Cherian, M. Baerns, *Catal. Today* **99** (1-2) (2005) 59.

[108]S. Imamura, T. Nakai, H. Kanai, T. Ito, *J. Chem. Soc.* **91** (8) (1995) 1261.

[109] U. S. Ozkan, R.B. Watson, *Catal. Today* **100** (1-2) (2005) 101.

[110] M. A. Banares, M. V. Martinez-Huerta, X. Gao, J. L. G. Fierro, I. E. Wachs, *Catal. Today* **61** (1-4) (200) 295.

[111] Y. Brik, M. Kacimi, F. Bozon-Verduraz, M. Ziyad, *J. Catal.* **211** (2) (2002) 470.

[112] M. A. Banares, N. D. Spencer, M. D. Jones, I. E. Wachs, *J. Catal.* **146** (1) (1994) 204.

[113] C. Liu, U. S. Ozkan, *J. Mol. Catal. A: Chem.* **220** (2004) 53.

[114] I. Wach, *Chem. Eng. Sci.*, **45** (1990) 2561.

[115] F. Cavani, N. Ballarini, A. Cericola, *Catal. Today*, **127** (2007) 113.

[116] E. Heracleous, M. Machli, A. A. Lemonidou, I. A. Vasalos, *J. Mol. Catal. A: Chem.* **232** (1-2) (2005) 29.

[117] S. Wang, K. Murata, T. Hayakawa, S. Hamakawa, K. Suzuki, *Catal. Lett.* **59** (1999) 173.

[118] H. L. Wan, W. Z. Wang, R. Q. Long, Z. S. Chao, W. D. Zhang, M. S. Chen, J. Z. Luo, S. Q. Zhou, *Catal. Today* **51** (1) (1999) 161.

[119] R. Grabowski, *Catal. Rev. Sci. Eng.* **48** (2) (2006) 199.

[120] M. D. Argyle, K. Chen, A. T. Bell, E. Iglesia, *J. Phys.Chem. B* **106** (21) (2002) 5421.

[121] M. D. Argyle, K. Chen, C. Resini, C. Krebs, A. T. Bell, E. Iglesia, *J. Phys.Chem. B* **108** (7) (2004) 2345.

[122] M. D. Argyle, K. Chen, E. Iglesia, A. T. Bell, *J. Phys. Chem. B* **109** (6) (2005) 2414.

[123] R. Burch, R. Swarnakar, *Appl. Catal.* **70** (1) (1991) 129.

[124] K. Chen, A. T. Bell, E. Iglesia, *J. Phys. Chem. B* **104** (6) (2000) 1292.

[125] E. A. Mamedov, V. Cortes Corberan, *Appl. Catal. A: Gen.* **127** (1-2) (1995) 1.

[126] E. Heracleous, A. F. Lee, I. A. Vasalos, A. A. Lemonidov, *Catal. Lett.* **88** (1-2) (2003) 47.

[127] J. C. Vedrine, J. M. M. Millet, J. C. Volta, *Catal. Today* **32** (1-4) (1996) 115.

[128] M. A. Banares, *Catal. Today* **51** (2) (1999) 319.

[129] A. Corma, J. M. Lopez Nieto, N. Paredes, M. Perez, Y. Shen, H. Cao, S. L. Suib, *Stud. Surf. Sci. Catal.* **72** (1992) 213.

[130] K. Chen, A. T. Bell, E. Iglesia, *J. Catal.* **209** (1) (2002) 35.

Chapter 2

Experimental

2.1 Introduction

In this chapter the details of catalyst preparation, materials and experimental measurement procedures used in this thesis are given.

2.2 Materials used

The following materials have been used: ammonium molybdate tetrahydrate $((NH_4)_6Mo_7O_{24}.4H_2O)$ (Sigma-Aldrich,99%), ammonium metavandate NH_4VO_3 (Sigma-Aldrich, 99%), oxalic acid $(C_2H_2O_4.2H_2O)$ (Riedel-deHaen, 99.5%), alumina $(\alpha-Al_2O_3)$ (Engelhard-Germany), silica amorphous (SiO_2) (Aerosil Ox-50 Degussa-Germany), Zirconia (monoclinic zirconium(IV) oxide, ZrO_2) (Fluka Chemie AG), niobia

(amorphous niobium(V) oxide, Nb_2O_5) (Sigma-Aldrich-203920), titania (anatase titanium dioxide, TiO_2) (Alfa Aesar), quartz-wool, ethane, oxygen, hydrogen, air, helium, argon.

2.3 Catalyst preparation

There are several methods for the preparation of metal oxides and each catalyst can be prepared through different routes including: precipitation, slurry formation, gelation and thermal transformation followed by drying and calcining. There are various preparation variables involved in these methods, which can affect the morphology and catalytic activity. Heat treatment, pH, temperature and ageing time affects the nature of catalyst in precipitation, slurry and deposition precipitation methods.

2.3.1 Preparation of MoV catalysts by slurry

Ammonium molybdate tetrahydrate (21.7 g, 0.13 mol), ammonium metavandate (5.7 g, 0.049 mol) and oxalic acid (10.0 g, 0.079 mol) were mixed in water (75 ml) at room temperature then heated at 80 ℃ with continuous stirring, resulting a thick dark bluish slurry. This slurry was dried at 120 ℃ for 16 hours (h) in an oven. The resulting material was crushed to form a powder and calcined at 350 ℃ for 4 h in flowing air 2 ℃/min ramp rate in a furnace.

2.3.2 Preparation of MoV catalysts by precipitation

Ammonium metavandate (21.7 g, 0.13 mol) was dissolved in water (50 ml) and heated to 80 ℃, and then solid oxalic acid (10.0 g, 0.079 mol) was added. The dark redish yellow suspension changed to a yellow coloured solution. A second aqueous solution of ammonium molybdate tetrahydrate (5.7 g, 0.049 mol) was prepared in water (25 ml) at 50 ℃ with continuous stirring. This ammonium molybdate tetrahydrate solution was added into the first solution slowly, and a greenish brown to a dark blue precipitate

formed. This was left stirring at 80 ℃ to remove excess water until a thick slurry was formed. This slurry was dried at 120 ℃ for 16 h in an oven. The obtained material was crushed and calcined at 350 ℃ for 4 h in flowing air 2 ℃/min ramp rate.

2.3.3 Preparation of supported MoV catalysts by precipitation-deposition

Catalysts were prepared in similar way to the catalyst prepared in section 2.3.2., with the addition of a support material. 30 wt% of amorphous silica (13.10 g, 0.22 mol) powdered form was added after the precipitation step, under continuous stirring at 80 ℃ to remove excess water and to obtain a thick slurry. This slurry was dried at 120 ℃ for 16 h in an oven. The resultant catalyst was crushed and calcined at 350 ℃ for 4 h in flowing air 2 ℃/min ramp rate. The resulted catalyst was pressed and crushed, and then sieved to 40-60 mesh size particles for the use in the catalytic reaction tests. Other support materials were also used with a similar procedure. 30 wt% of zirconium (IV) oxide monoclinic type (ZrO_2), niobium (V) oxide (Nb_2O_5), titanium dioxide anatase (TiO_2) and α-alumina (Al_2O_3) were added into the slurry of MoV oxides respectively and then dried into oven at 120 °C for 16 h. The precursor powders were then calcined in air at 350 °C for 4 h, in separate batches.

2.4 Catalytic activity measurements

Steady state catalytic measurements were carried out in a fixed bed stainless steel reactor (i.d. 3/8 ") using 1 g amount of catalyst of 40-60 mesh size particles. The catalyst bed was held in the middle of the reactor using glass wool. The catalyst bed was located in the isothermal heating zone of the reactor. The reaction temperature was measured by using a thermocouple located in the catalyst bed. All transfer lines were kept heated above 150 ℃ to avoid condensation. The catalyst bed was packed between two quartz-wool plugs, before and after the catalyst bed to minimize the empty reactor volume. The

feed consisted of 15-50 % hydrocarbon, 10-20 % oxygen, with the balance nitrogen. The total flow rates ranged between 25 and 100 ml/min. Different pressures (atmospheric pressure to 200 psig) and temperatures between 250-340 ℃ were used. The reactor system is shown in Fig. 2.1.
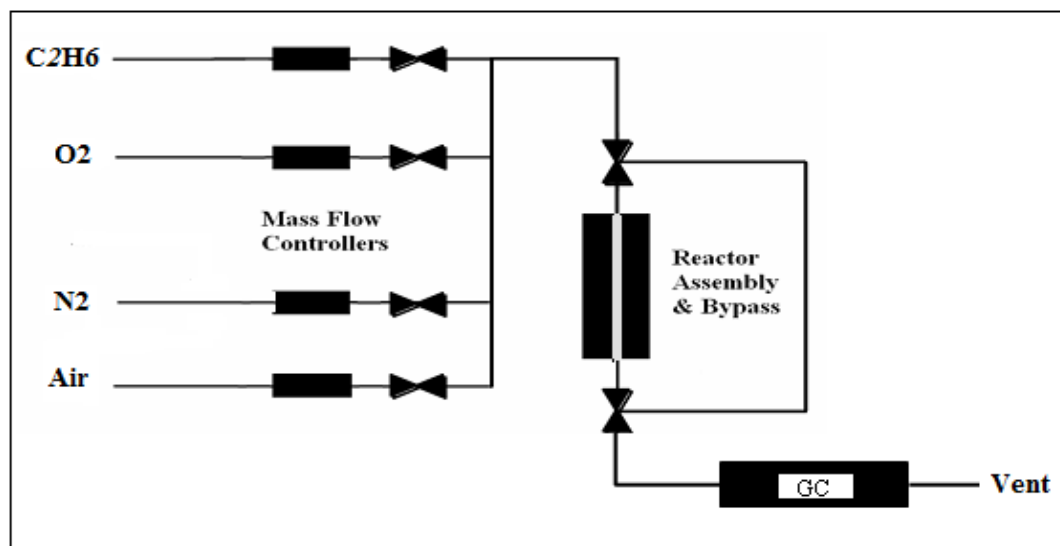
Fig.2.1: Catalytic reactor set-up system.

Feed and effluent composition analyses were conducted using an Agilent HP gas chromatogram (GC) equipped with Porapak N, Hayesep Q and Molecular Sieve columns. All columns elluted to TCD and FID detectors using helium as a carrier gas. GC data points were collected and averaged after 60 minutes of stabilization on stream and all carbon balances were close to 100 % (ie. ±5 %). Conversion, selectivity and yield are all calculated on a carbon atom basis.

Ethane conversion is defined as:

$$X_{ethane} = \frac{\sum \left(n_i \times C_i\right)_{products}}{2 \times n_{ethane}}$$ (2.1)

where n_i and C_i are the number of moles of and carbon atoms in molecule i, respectively.

It should be noted that the numerator summation contains only the products formed, not ethane.

The selectivity of component i is defined as:

$$S_i = \frac{n_i \times C_i}{\sum \left(n_i \times C_i\right)_{products}}$$ (2.2)

And the yield of component i defined as:

$$Y_i = \frac{n_i \times C_i}{2 \times n_{ethane}}$$ (2.3)

Using these definitions, the yield of a given component is simply the selectivity of that component times the conversion of ethane. The specific details on the various experiment regarding product analysis and data evaluation method used is given in Appendix 4.

2.5 Analysis of products

The total gas phase product stream was analyzed by online gas chromatography, using a TCD and FID. The detailed description of gas chromatography used in this study is discussed in Appendix 3.

2.5.1 Gas chromatography (GC)

Gas chromatography (GC) is a physical separation of two or more compounds based on their differential distribution between two phases, one of which is stationary and the other fluid (mobile phase i.e. carrier gas). In the case of gas chromatography the mobile phase is a gas. This technique specifically involves a sample being vaporized and injected into the head of chromatographic column.

2.5.1.1 Instrumental components

Gas chromatography mainly consists of five components; i) carrier gas, ii) sample injection port, iii) column, iv) detector and v) data acquisition system (recorder).
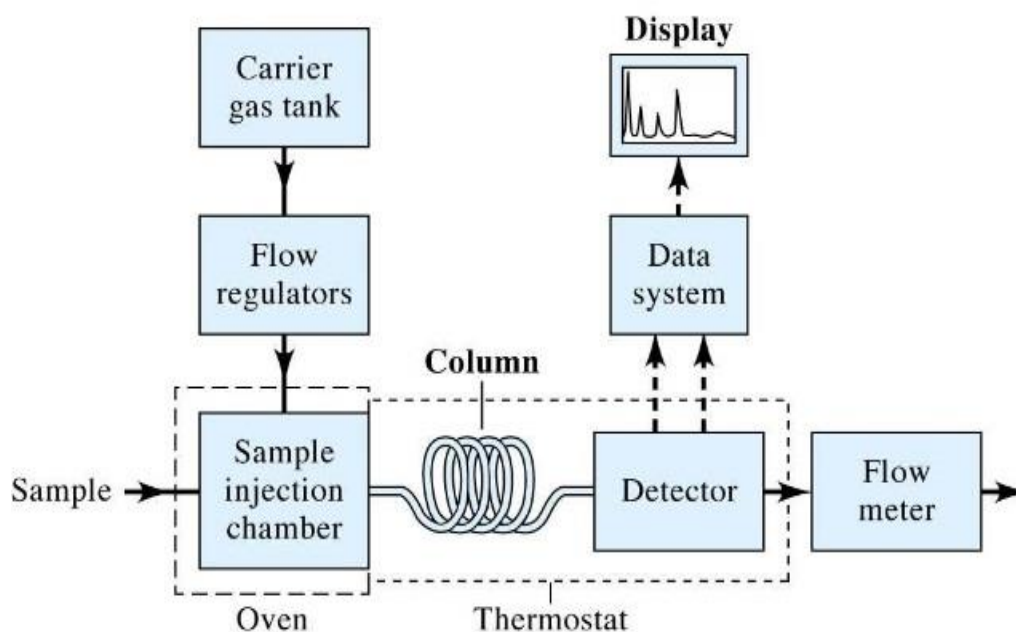
Fig.2.2: Schematic diagram of a GC system [1].

(i) Carrier gas

The most common carrier gases used in GC are He, Ar, H_2, and N_2. Selection of carrier gases depends on the nature of the detector being used. The carrier gas selected must be

43

inert, dry, and pure and may not be adsorbed by the column material. When analyzing gas samples, however, the carrier is sometimes selected based on the sample's composition, for example, when analyzing a mixture in argon, an argon carrier is preferred, because the argon in the sample does not show up on the chromatogram. Helium is commonly used as a carrier gas. The carrier gas is also called the mobile phase because it transports the sample through the columns. The GC system used in this study used helium as the carrier gas.

(ii) Sample injection port

The sample to be analyzed is introduced at the injection port via a micro syringe. The injection port is heated in order to volatilize the sample. Once in the gas phase, the sample is carried onto the column by the carrier gas. The volume injected can be further reduced by using a split injection system in which a controlled fraction of the injected sample is carried away by a gas stream before entering the column.
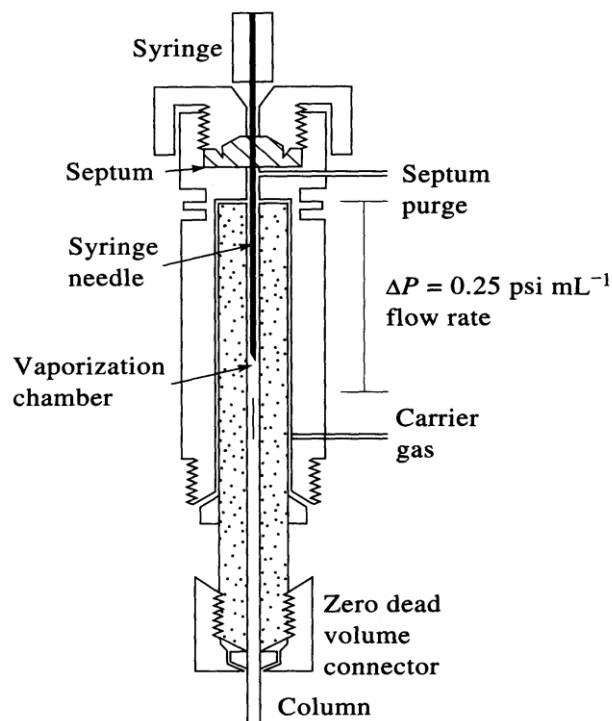
Fig.2.3: Diagram of a sample injection port [1].

(iii) Columns

The column is where the components of the sample are separated and contains the stationary phase. GC columns are of two types, packed and capillary, and are composed of three elements;

1) the container for the packing

2) the solid support

3) stationary phase

The solid support provides a large inert surface area to hold the fluid phase. The stationary phase is the only active portion of the column. Separation takes place between the carrier gas and this material. The affinity of the sample for the stationary phase determines the length of the time individual sample components will remain in the

45

column. Those compounds with the least affinity emerge first and those with the greatest affinity emerge last. Materials for use as stationary phase are classed as polar or non-polar in nature.

As the components move into the column from the injection port they adsorb in the stationary phase and are retained. Upon desorption into the mobile phase they are carried further down the column. This process is repeated many times as the components migrate through the column. Components that interact more strongly with the stationary phase spend proportionally less time in the mobile phase and therefore move through the column more slowly. Normally the column is chosen such that its polarity matches that of the sample. When this is the case, the interaction and elution times can be rationalized according to Raoult's law and the relationship between vapor pressure and enthalpy of vaporization.

(iv) Detectors

If the column conditions are chosen correctly, the components in the sample will exit the column and flow past the detector one at a time. There are several different types of detectors that can be connected to a GC. Flame-ionization detectors (FID), flame photometric detectors (FPD) and thermal conductivity detectors (TCD) are very common and are useful for determining the concentration of specific compounds. The choice of detector is determined by the general class of compounds being analyzed and the sensitivity required.

(a) Flame ionization detector (FID)

Flame ionization detectors (FID) are the most widely used detectors for organic samples. FIDs use an air/hydrogen flame to pyrolyze the sample. The pyrolysis of the compounds

in the flame creates ions. A voltage is applied across the flame and the resulting flow of ions is detected as a current. The number of ions produced, and therefore the resulting current, depends on the flame conditions and the identity of the molecule in question (the current is proportional to the number of reduced carbons in the molecule). In other words, the detector shows a different response to each compound. For this reason, separate calibrations must be performed for each compound analyzed.

(b) Thermal conductivity detector (TCD)

TCD is used to analyse inorganic gases (argon, nitrogen, hydrogen, etc) and lower hydrocarbon molecules. The TCD is often called a universal detector because it responds to all compounds. The TCD works by measuring the change in carrier gas thermal conductivity caused by the presence of the sample, which has a different thermal conductivity from that of the carrier gas. The TCD compares the thermal conductivity of two gas flows carrier (reference) gas and the sample. Helium is typically used as the carrier gas for the TCD because of its high thermal conductivity. Changes in the temperature of the electrically-heated wires in the detector are affected by the thermal conductivity of the gas which flows around this. The changes in this thermal conductivity are sensed as a change in electrical resistance and are measured. The TCD can detect concentrations from down to around 100 ppm on a flat baseline with sharp peaks. The concentration of a sample component can be estimated by the ratio of the analyzed peak area to all components (peaks) areas in the sample. Calibration with a standard mixture is required, both to check linearity and as calibration for the sample.

(v) Data acquisition

Computer based systems are extensivly used for the analysis of data from the GC systems. The raw data can be plotted to from the chromatographs in variable scales of components with a retention time and the response axis.

2.6 Surface and bulk characterization

2.6.1 Surface area (BET)

In the field of heterogeneous catalysis, the surface area is an important factor in the catalytic activity. BET serves as the basis for an important analysis technique for the measurement of the specific surface area of a material. There are different methods used to measure surface area and each method can yield different results. Most methods are based on the physisorption of nitrogen and either a single point or multipoint method is used to calculate the surface area. A common and widely used technique for the estimation of surface area is the BET meyhod, named after Brunauer, Emmet and Teller and developed in 1938.

The BET method is widely used in surface science for the calculation of surface areas of solids by physical adsorption of gas molecules. A total surface area S_{total} and a specific surface area S are evaluated by the following equations:

$$S_{\text{BET,total}} = (v_m\,Ns) / V \tag{2.4}$$

$$v_m = v_a(1\text{-}P/P_0) \tag{2.5}$$

where N is the Avogadro's number, S: cross section of the adsorbing species, V: molar volume of adsorbate gas, P: partial pressure of adsorbate gas, ɑ: mass of adsorbent (g).

In the present study the surface areas of the samples were determined by the BET method using a Micrometrics ASAP2000 (Gemini) instrument. Measurement of the surface area was achieved by N_2 physisorption at -196 ºC, the temperature of liquid nitrogen. Before each measurement, the sample was degassed for 1 h at 100 ºC under flowing N_2. The sample tube (with sample) was first evacuated and the void volume of the apparatus measured using helium. Afterwards the sample tube was again evacuated after immersed into liquid nitrogen, followed by adsorption of the nitrogen gas. The pressure drop versus volume of nitrogen adsorbed was then recorded, which could be used to calculate the surface area according to the method described above.

2.6.2 X-Ray diffraction (XRD)

XRD is a versatile, non-destructive technique that reveals detailed information about the crystallographic structure of solid materials.

The technique is based on observing the scattered intensity of an X-ray beam hitting a sample as a function of incident and scattered angle, polarization, and wavelength or energy. Diffraction occurs when electromagnetic radiation impinges on a material with a comparable length scale to the wavelength of radiation. The distances of crystal lattices are between 0.15-0.4 nm in the electromagnetic spectrum of X-ray, which allows diffraction to occur.
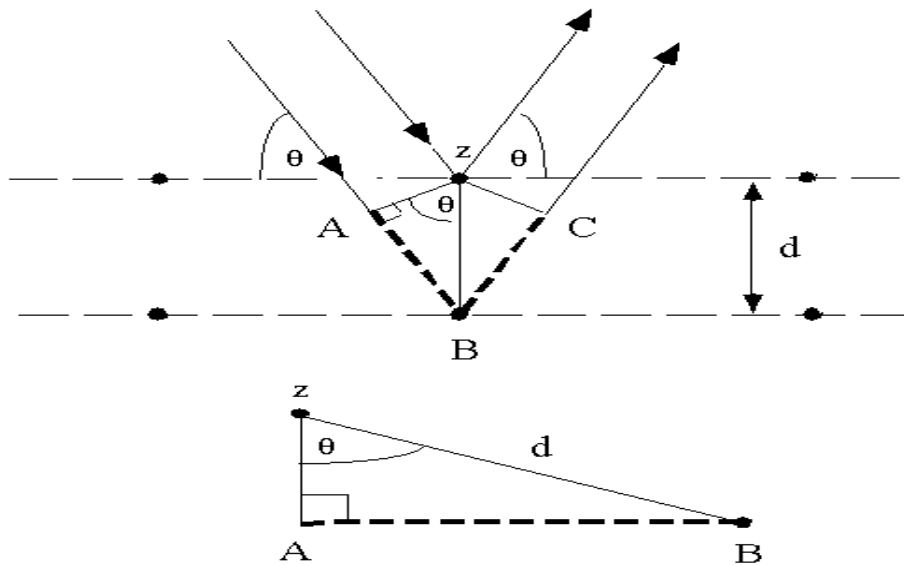
Fig.2.4: A simple illustration of X-ray diffraction [2].

Two X-ray beams with wavelength λ are reflected from two adjacent crystal lattices. The resulting diffraction follows a mathematical equation called Bragg's law.

$$d = n \lambda / 2\sin\theta \qquad\qquad (2.6)$$

where d is the interplanar spacing, θ is the diffraction angle, n is an integer and λ is the wavelength of the radiation. When the distances A-B and B-C are a whole number of wavelengths there will be constructive interference and a reflection will be observed. The equation can be applied to both single crystal and crystalline powders due to the random orientation of the crystallites.

This study used an Enraf Nonius PSD120 diffractometer with a monochromatic [CuKα] source operated at 40 keV and 30 mA. Phase identification was performed by matching experimental patterns to the JCPDS.

2.6.3 X-ray fluorescence (XRF)

X-ray fluorescence (XRF) spectrometry is an elemental analysis technique with broad application. XRF is based on the principle that individual atoms, when excited by an external energy source, emit X-ray photons of a characteristic energy or wavelength. By counting the number of photons of each energy level emitted from a sample, the elements present may be identified and quantified. XRF is capable of analyzing solid, liquid, and thin-film samples for both major and trace (ppm-level) components.

The identification of elements by XRF is possible due to the characteristic radiation emitted from the inner electronic shells of the atoms under certain conditions. The emitted quanta of radiation are X-ray photons whose specific energies permit the identification of their source atoms. X-rays are generated using an X-ray tube and focused onto the surface to be analyzed. At its simplest, the technique examines the signal given by an object which has had X-rays directed at it. This signal shows which chemical elements are present and at what quantity. The technique is capable of great accuracy with clean and flat samples that can be compared with standards of similar, known, composition. Without the limitation of a sample chamber, objects of any size can be investigated without the need for sample removal. In most XRF systems the beam of X-rays incident on the sample are produced with a vacuum tube and created by bombarding a target (such as Rh, W, Cu, or Mo) with highly accelerated electrons.
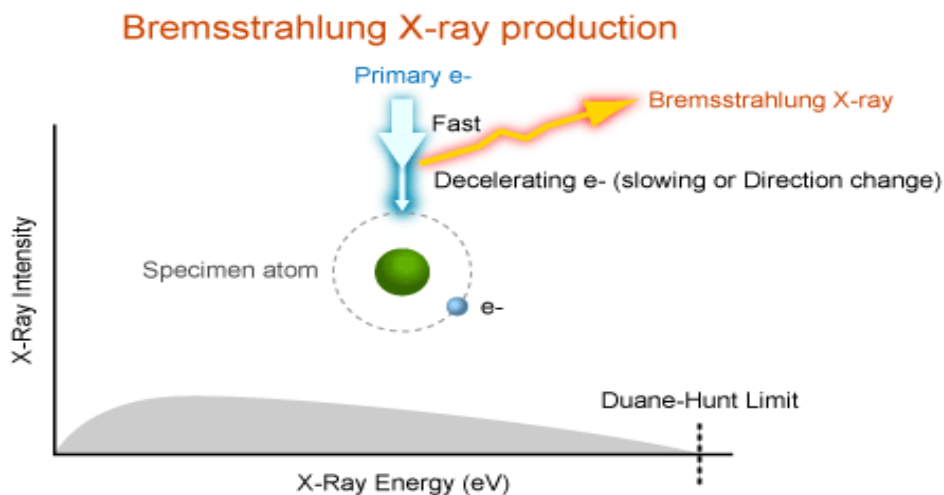
Fig.2.5: Diagram of the Bremsstrahlung effect in XRF [3].

The electrons as shown in Fig.2.5 penetrate the target atoms, they may have their direction changed as they pass near the nucleus of the target atoms causing a sudden deceleration and loss of kinetic energy. In this loss of kinetic energy the electron may emit an X-ray with energy related to the amount of energy lost. As a result a broad spectrum of X-ray energies, known as a Bremsstrahlung continuum, is emitted from the X-ray tube target. This continuum can be adjusted by tube high voltage settings, beam filtering and secondary targets to focus on detection of specific elements within the sample. This capitalizes on the different absorption edges of each element. The accelerated electrons also cause the target to fluoresce. These target characteristic X-rays are also incident on the sample, and must be considered during data analysis.

In the present study, the XRF analysis was performed using Horiba XGT-7000 X-ray analytical microscope fitted with a rhodium X-ray tube operating at 50 kV, with a nickel filter with a spot size of 1.2 mm and a silicon detector.

2.6.4 Scanning electron microscopy (SEM)

Scanning electron microscopy (SEM) is a powerful technique in the examination of materials morphology.The SEM uses a focused beam of high-energy electrons to generate a variety of signals at the surface of sample. The signals that derive from electron-sample interactions reveal information about the sample including external morphology (texture), crystalline structure and orientation of materials making up the sample. In most applications, data are collected over a selected area of the surface of the sample, and a 2-dimensional image is generated that displays special variations in these properties. Areas ranging from approximately 1 cm to 5 μm in width can be imaged in a scanning mode using conventional SEM techniques (magnification ranging from 20 times to approximately 30,000 times, with resolution of 50 to 100 nm).

Accelerated electrons in an SEM carry significant amounts of kinetic energy, and this energy is dissipated as a variety of signals produced by electron-sample interactions when the incident electrons are decelerated in the solid sample. These signals include secondary electrons that produce SEM images. Secondary electrons and backscattered electrons are commonly used for imaging samples: secondary electrons are most valuable for showing morphology and topography on samples. X-ray generation is produced by inelastic collisions of the incident electrons with electrons in discrete orbitals (shells) of atoms in the sample. As the excited electrons return to lower energy states, they yield X-rays that are of a fixed wavelength that is related to the difference in energy levels of electrons in different shells for a given element.

The SEM analysis was performed using a Zeiss Evo-40 series scanning electron microscope in the present work.

2.6.5 Energy dispersive X-ray analysis (EDX)

EDX is an X-ray technique used to identify the elemental composition of a sample. During EDX Analysis, the sample is bombarded with an electron beam inside the scanning electron microscope. The incident beam excites an electron in inner shell prompting its ejection resulting in the formation of an electron hole within the atom's electronic structure. A position vacated by an ejected inner shell electron is eventually occupied by a higher-energy electron from an outer shell. To be able to do so, however, the transferring outer electron must give up some of its energy by emitting an X-ray.

The amount of energy released by the transferring electron depends on which shell it is transferring from, as well as which shell it is transferring to. Furthermore, the atom of every element releases X-rays with unique amounts of energy during the transferring process. Thus, by measuring the amounts of energy present in the X-rays being released by a specimen during electron beam bombardment, the identity of the atom from which the X-ray was emitted can be established.

The EDX detector measures the number of emitted X-rays versus their energy .The energy of the X-rays is characteristic of the element from which X-ray was emitted. The EDX detector converts the energy of each individual X-ray into voltage signal of proportional size. This is achieved through a three stage process. Firstly the X-ray is converted into a charge by an ionization of atoms in the semiconductor crystals. Secondly this charge converted into the voltage signal by the field effect transmitter amplifier. Finally the voltage signal is input the pulse processor for measurement. The output from the amplifier is a voltage ramp where each X-ray appears as a voltage step on the ramp.

The EDX analysis in the present study was carried out on a Zeiss Evo-40 series SEM in conjunction with INCAx-sight EDX detector equipment.

2.6.6 X-ray photoelectron spectroscopy (XPS)

X-ray photoelectron spectroscopy (XPS) is used to characterize the surface region of materials, as it provides information on the elemental composition, the oxidation state of elements and, dispersion of one phase over another by analyzing the energy distribution of electrons ejected from the material when it is exposed to X-rays of a well-defined energy. XPS reveals which chemical elements are present at the surface and the nature of the chemical that exists between these elements. It can detect all of the elements except hydrogen and helium.

XPS is based on photoelectron emission principle. In a common XPS spectrum some of the photo-ejected electrons inelastically scatter through the sample to the surface, while others undergo prompt emission and suffer no energy loss in escaping the surface and into the surrounding vacuum. Once these photo-ejected electrons are in the vacuum, they are collected by an electron analyzer that measures their kinetic energy. An electron energy analyzer produces an energy spectrum of intensity (number of photo-ejected electrons versus time) versus binding energy (the energy the electrons had before they left the atom). Each prominent energy peak on the spectrum corresponds to a specific element.

$$E = h\nu \qquad\qquad\qquad (2.7)$$

There is a threshold in frequency below which light, regardless of intensity, fails to eject electrons from a metallic surface.

$$h\nu_c > e\Phi_m \qquad\qquad\qquad (2.8)$$

where, h- is Planck's constant (6.62×10^{-34} J s), $\nu-$ is the frequency (Hz) of the radiation and Φ_m is the work function.
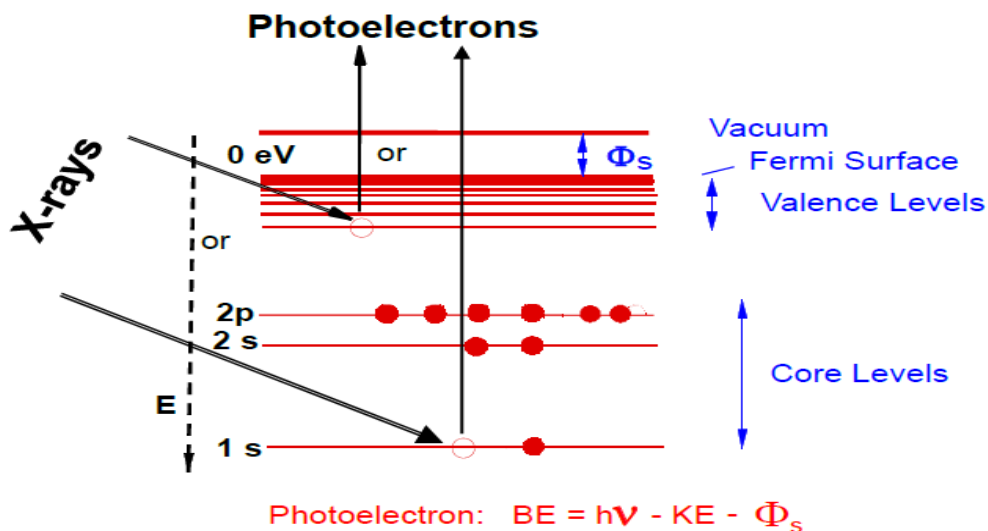
Fig.2.6: Energy distribution of the emitted photoelectrons in XPS [4].

In photoelectron spectroscopy such as XPS, AES (Auger Electron Spectroscopy) and UPS (Ultravilot Photoemission Spectroscopy), the photon energies range from 1200-1500 eV much greater than any typical work function values (2-5 eV). In these techniques, the kinetic energy distribution of the emitted photoelectrons (i.e. the number of emitted electrons as a function of their kinetic energy) can be measured using an appropriate electron energy analyzer and a photoelectron spectrum can thus be recorded.

In the present study, XPS spectra were recorded using a Kratos Axis Ultra-DLD photoelectron spectrometer. Samples were run using a monochromatic aluminum X-ray source (hν =1486.6 eV). A Kratos charge neutralization system was used to minimize sample charging. All high-resolution spectra were run at pass energy of 40 eV, whilst survey spectra were run at energy of 160 eV.

2.6.7 Transmission electron microscopy (TEM)

Transmission electron microscopy (TEM) is useful for understanding the internal microstructure of materials at the nanometer level. It allows real-space images of materials with resolutions on the order of a few tenths to a few nanometers to be obtained, depending on the imaging conditions, and simultaneously obtain diffraction information from specific regions in the images. Variations in the intensity of electron scattering across a thin specimen can be used to image strain fields, defects such as dislocations and second-phase particles, and even atomic columns in materials under certain imaging conditions.

In addition to diffraction and imaging, the high-energy electrons (usually in the range of 100 to 400 keV of kinetic energy) in TEM cause electronic excitations of the atoms in the specimen. Two important spectroscopic techniques make use of these excitations by incorporating suitable detectors into the transmission electron microscope, energy-dispersive X-ray spectroscopy (EDS), and electron energy loss spectroscopy (EELS). Nanometer-scale chemical compositional analysis can be performed by using a focused electron probe. Special distribution of elements can be obtained by scanning the probe over the specimen, or by energy-filtered imaging, a special mode in advanced EELS spectrometer.

Electrons are usually generated in an electron microscope by a process known as thermionic emission from a filament, usually tungsten, in the same manner as a light bulb, or alternatively by field electron emission [5]. The electrons are then accelerated by an electric potential and focused by electrostatic and electromagnetic lenses onto the sample. The transmitted beam contains information about electron density, phase and

periodicity and this beam is used to form an image. Layout of optical components in a TEM is given in Fig. 2.7.

Electron gun

Condensor aperture

Specimen port

Objective aperture

Objective lens

Diffraction lens

Intermediate aperture

Intermediate lens

Projector lenses

Binoculars

Fluorescent screen

Image recording system
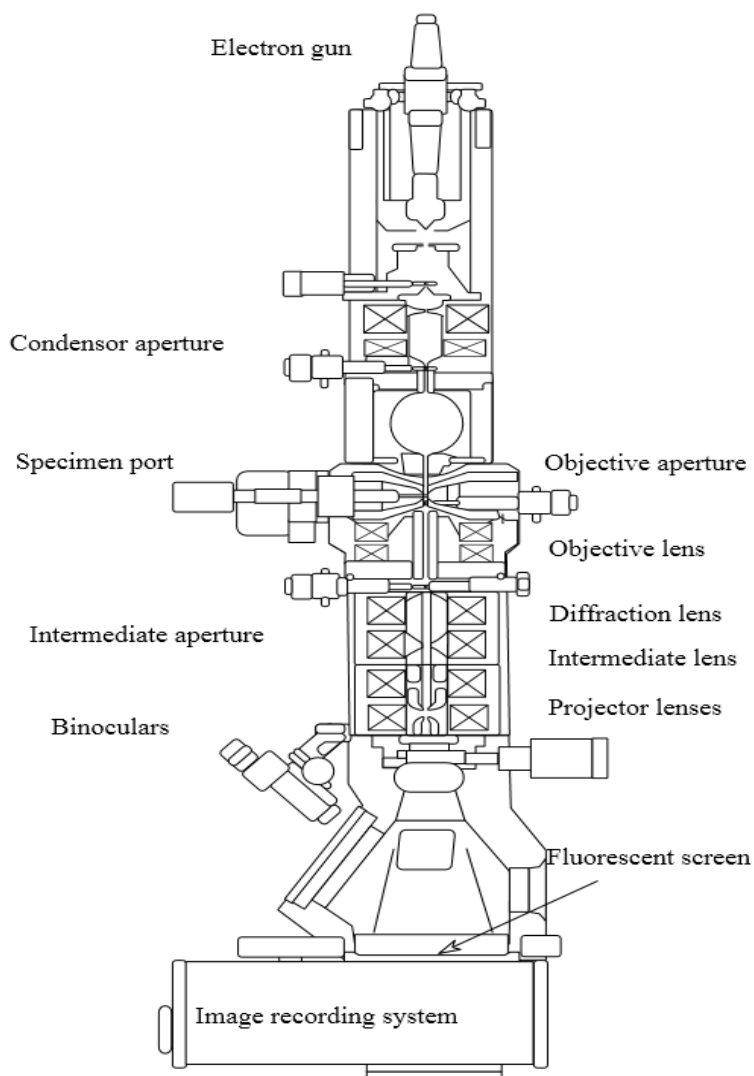
Fig.2.7: Layout of optical components of TEM [5].

In the present study, samples analyzed by TEM were prepared by dipping a carbon-coated copper TEM grid directly into the finely ground dry catalyst powder and then shaking off any loosely bound residue. Scanning transmission electron microscopy

(STEM) high angle annular dark field (HAADF) imaging was used to image the individual nanoparticles at atomic resolution with an aberration corrected JEOL 2200FS (S) TEM operating at 200 kV.

2.6.8 Raman spectroscopy

Raman spectroscopy is useful analytical tool for quickly identifying structure of the catalysts. Vibrational information is specific to the chemical bonds and symmetry of molecules. Therefore, it provides a fingerprint by which the molecule can be identified.

Raman scattering (or the Raman Effect) was discovered in 1928 by C. V. Raman who won the Nobel Prize for his work. Raman spectroscopy offers several advantages for microscopic analysis. Since it is a scattering technique, specimens do not need to be fixed or sectioned. Raman spectra can be collected from a very small volume ($<$ 1 µm in diameter); these spectra allow the identification of species present in that volume. Water does not generally interfere with Raman spectral analysis.

When light is scattered from a molecule or crystal, most photons are elastically scattered. The scattered photons have the same energy (frequency) and, therefore, wavelength, as the incident photons. However, a small fraction of light is scattered at optical frequencies different from, and usually lower than, the frequency of the incident photons. The process leading to this inelastic scatter is termed the Raman effect. Raman scattering can occur with a change in vibrational, rotational or electronic energy of a molecule. If the scattering is elastic, the process is called Rayleigh scattering. If it is inelastic, the process is called Raman scattering.

The Raman scattering arises when a photon is incident on a molecule and interacts with the electric dipole of the molecule. When a probe beam of radiation described by an

electric field E interacts with a material, it induces a dipole moment, μ, in the molecules that make up the material:

$$\mu = a \; x \; E \qquad\qquad (2.9)$$

where, a is the polarizability of the molecule. The polarizability is a proportionality constant describing the deformability of the molecule. In order for a molecule to be Raman-active, it must possess a molecular bond with a polarizability that varies as a function of interatomic distance. Light striking a molecule with such a bond can be absorbed and then re-emitted at a different frequency (Raman-shifted), corresponding to the frequency of the vibrational mode of the bond.

It is a form of electronic spectroscopy, although the spectrum contains vibrational frequencies. In classical terms, the interaction can be viewed as a perturbation of the molecule's electric field. In quantum mechanics the scattering is described as an excitation to a virtual state lower in energy than a real electronic transition with nearly coincident de-excitation and a change in vibrational energy. The scattering event occurs in 10^{-14} seconds or less. The virtual state description of scattering is shown in Fig. 2.8.
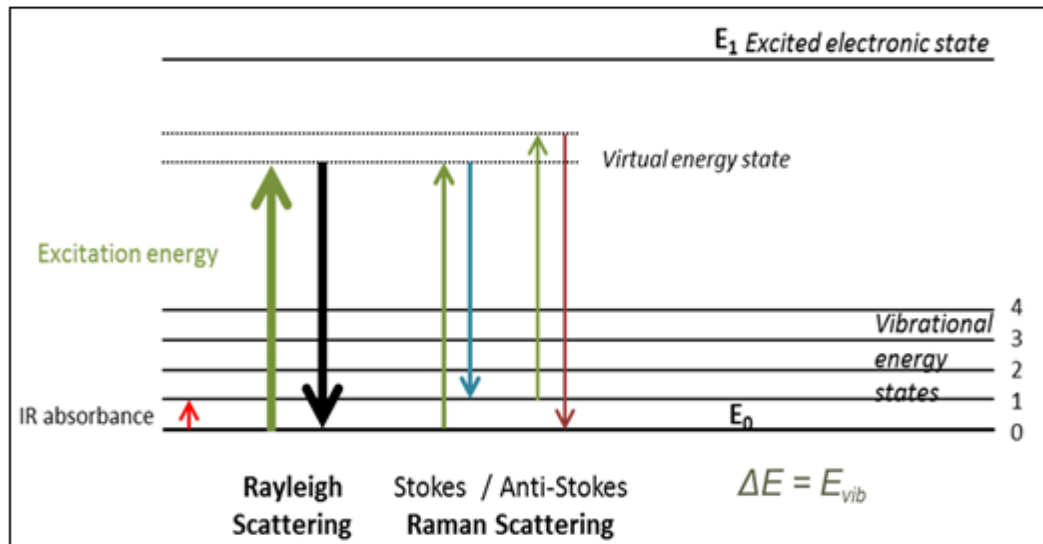
Fig.2.8: Energy-level diagram showing the states involved in Raman signal [6].

The energy difference between the incident and scattered photons is represented by the arrows of different lengths in Fig. 2.8. Numerically, the energy difference between the initial and final vibrational levels, or Raman shift is calculated using equation 2.10.

$$\bar{\upsilon} = (1/\lambda_{incident}) - (1/\lambda_{scattered}) \qquad (2.10)$$

In which $\lambda_{incident}$ and $\lambda_{scattered}$ are the wavelengths (in cm) of the incident and Raman scattered photons, respectively. The vibrational energy is ultimately dissipated as heat. Because of the low intensity of Raman scattering, the heat dissipation does not cause a measurable temperature rise in a material. At room temperature the thermal population of vibrational excited states is low, although not zero. Therefore, the initial state is the ground state, and the scattered photon will have lower energy (longer wavelength) than the exciting photon [6].

A small fraction of the molecules are in vibrationally excited states. Raman scattering from vibrationally excited molecules leaves the molecule in the ground state. The scattered photon appears at higher energy, as shown in Fig. 2.8. This anti-Stokes-shifted Raman spectrum is always weaker than the Stokes-shifted spectrum, but at room temperature it is strong enough to be useful for vibrational frequencies less than about 1500 cm^{-1}. The Stokes and anti-Stokes spectra contain the same frequency information. The ratio of anti-Stokes to Stokes intensity at any vibrational frequency is a measure of temperature. Anti-Stokes Raman scattering is used for contactless thermometry. The anti-Stokes spectrum is also used when the Stokes spectrum is not directly observable, for example because of poor detector response or spectrograph efficiency.

Raman spectroscopy was carried out in the present work with a Renishaw inVia Raman Microscope using a 514 nm laser source. For initial studies, samples were mounted on a microscope slide and spectra recorded under ambient conditions in the open atmosphere.

A series of Raman measurements were also made in an environment cell under controlled conditions. All catalysts were heated from ambient temperature to 150 ºC in a flow of dry nitrogen and spectra were collected at intervals of 10 ºC.

2.6.9 Thermogravimetric analysis (TGA)

Thermogravimetric analysis (TGA) is a method of thermal analysis in which changes in physical and chemical properties of materials are measured as a function of increasing temperature (with constant heating rate), or as a function of time (with constant temperature and/or constant mass loss). The technique can characterize materials that exhibit weight loss or gain due to decomposition, oxidation, or dehydration.

TGA is a type of testing that is performed on samples to determine changes in weight in relation to change in temerature. As many weight loss curves look similar, the weight loss curve may require transformation before results may be interpreted. A derivative weight loss curve can identify the point where weight loss is most apparent [7]. Again, interpretation is limited without further modifications and deconvolution of the overlapping peaks may be required. TGA is a process that utilizes heat and stoichiometry ratios to determine the percent by mass ratio of a solute. If the compounds in the mixture that remain are known, then the percentage by mass can be determined by taking the weight of what is left in the mixture and dividing it by the initial mass. The stoichiometric ratio can be used to calculate the percent mass of the substance in a sample.

In the present study, TGA analysis of the catalyst was carried out using a Setaram Labsys instrument enabling concurrent weight loss with heat flow changes (TG-DTA). The experiments were carried out in an inert N_2 atmosphere from 30 ºC to 600 ºC with a ramp rate of 5 ºC/min.

2.7 References

[1] "Gas Chromatography". *Quantitative chemical analysis* (Chapter) (Fifth Ed.). W. H. Freeman and Company. pp. **675–712**. ISBN 0-7176-2881-8.

[2] B.E. Warren, *X-ray Diffraction*. New York. (1969) ISBN 0-486-66317-5.

[3] V. E. Buhrke, R. Jenkins, D. K. Smith, "A Practical Guide for the Preparation of Specimens for X-Ray Fluorescence and X-Ray Diffraction Analysis". *John Wiley & Sons, Inc.*, (1998) QD96.X2P73 ISBN 0-471-19458-1.

[4] S. Ray, and A.G. Shard, "Quantitative Analysis of Adsorbed Proteins by X-ray Photoelectron Spectroscopy". *Anal. Chem.*, **83** (22) (2011) 8659.

[5] K. Porter, and J. Blum, "A Study in Microtomy for Electron Microscopy". *The Anatomical Record*, **117** (4) (1953) 685.

[6] D. J. Gardiner, *Practical Raman spectroscopy*. Springer-Verlag. (1989) ISBN 978-0-387-50254-0

[7] E. Mansfield, A. Kar, T. P. Quinn and S. A. Hooker, "Quartz Crystal Microbalance for Microscale Thermogravimetric Analysis". *Anal. Chem.*, **82** (24) (2010) 9977.

Chapter 3

Results of metal ratio impact on the catalytic performance of MoV oxide catalysts

3.1 Introduction

This chapter includes the results and discussion of the catalyst preparation by varying the vanadium concentration and using molybdenum as a base metal oxide. A list for all of the catalysts prepared with different metal ratios is given in Table 3.1. Catalytic activity tests were carried out as explained in Chapter 2. The feed consisted of ethane, oxygen and nitrogen in the molar ratio of 40:10:50. The feed and reaction products were analyzed online by a GC equipped with a TCD and FID.

Table 3.1: Catalysts prepared by varying the vanadium concentrations.

Catalyst Ref.	Metal ratio (Mo/V)
$Mo_1V_{0.12}$	1 : 0.12
$Mo_1V_{0.25}$	1 : 0.25
$Mo_1V_{0.40}$	1 : 0.40
$Mo_1V_{0.60}$	1 : 0.60
$Mo_1V_{0.80}$	1 : 0.80
Mo_1V_1	1 : 1

3.2 Experimental results

3.2.1 Effect of vanadium concentration on the catalytic activity

The conversion of ethane and product selectivities of these catalysts was tested at different temperatures (270 - 310 °C). Tables 3.2 - 3.4 presents catalysts testing results for all catalysts. Among these catalysts series, $Mo_1V_{0.40}$ shows the highest activity with 70 % selectivity to ethene and 15 % conversion of ethane at low temperature (270 °C), although it produces a significant amount of acetic acid (AA) and a lower amount of carbon oxide (CO_x). Mo_1V_1 was used as a reference as this gives the lowest ethene selectivity and highest carbon oxide formation. The catalyst with the lowest vanadium concentration ($Mo_1V_{0.12}$) shows poor activity and high selectivity to carbon oxide formation, the same behavior as seen with the catalyst prepared with the highest concentration of vanadium (Mo_1V_1). However, the carbon monoxide formation is high with low vanadium concentration and increases rapidly with increasing concentration of vanadium from 1:0.60 – 1:1.

Table 3.2: Catalytic activity results at 270 ºC.

Cat.	Conv. (%)		Selectivity (%)				Yield (%)
Ref.	C_2H_6	O_2	CO_2	CO	C_2H_4	AA	C_2H_4
$Mo_1V_{0.12}$	2.8	4.4	8.6	34.7	55.6	1.1	1.6
$Mo_1V_{0.25}$	11.3	31.6	4.7	15.2	65.8	14.3	7.5
$Mo_1V_{0.40}$	16.7	60.4	3.4	6.6	69.6	20.4	10.3
$Mo_1V_{0.60}$	11.2	28.1	8.7	16.6	59.3	15.4	6.6
$Mo_1V_{0.80}$	9.2	23.9	8.9	20.7	57.3	13.1	5.3
Mo_1V_1	5.7	13.7	9.1	44.5	39.7	6.7	2.3

Reaction conditions: Pressure = 70 psig, Temp. = 270 ºC, feed ratio = ethane: oxygen: nitrogen (40:10:50), catalyst weight = 1 g, feed flow = 25 ml/min.

Table 3.3: Catalytic activity results at 290 ºC.

Cat.	Conv. (%)		Selectivity (%)				Yield (%)
Ref.	C_2H_6	O_2	CO_2	CO	C_2H_4	AA	C_2H_4
$Mo_1V_{0.12}$	4.0	8.5	9.9	37.6	50.9	1.6	2.1
$Mo_1V_{0.25}$	16.1	46.8	5.1	16.9	60.6	17.5	9.8
$Mo_1V_{0.40}$	21.8	80.2	6.4	8.8	66.5	18.4	14.5
$Mo_1V_{0.60}$	17.2	62.7	10.1	20.4	52.7	16.9	9.1
$Mo_1V_{0.80}$	14.8	54.1	10.4	24.0	51.0	14.6	7.6
Mo_1V_1	9.9	47.3	11.6	48.1	28.4	11.9	2.8

Reaction conditions: Pressure = 70 psig, Temp. = 290 ºC, feed ratio = ethane: oxygen: nitrogen (40:10:50), catalyst weight = 1 g, feed flow = 25 ml/min.

Table 3.4: Catalytic activity results at 310 ºC.

Cat.	Conv. (%)		Selectivity (%)				Yield (%)
Ref.	C_2H_6	O_2	CO_2	CO	C_2H_4	AA	C_2H_4
$Mo_1V_{0.12}$	6.0	14.6	11.4	39.4	47.3	1.9	2.8
$Mo_1V_{0.25}$	19.1	71.3	7.8	16.5	57.5	18.2	11
$Mo_1V_{0.40}$	23.9	98.6	8.6	10.4	62.9	20.1	15
$Mo_1V_{0.60}$	21.2	88.1	11.6	22.4	48.3	17.7	10.2
$Mo_1V_{0.80}$	17.4	68.8	12.4	26.1	45.1	15.4	7.9
Mo_1V_1	12.7	56.4	13.2	50.3	24.2	12.3	3.2

Reaction conditions: Pressure = 70 psig, Temp. = 310 ºC, feed ratio = ethane: oxygen: nitrogen (40:10:50), catalyst weight = 1 g, feed flow = 25 ml/min.

Catalytic activity data shows that the catalyst prepared with composition $Mo_1V_{0.40}$ gives ethane conversion of 22 % with 67 % selectivity to ethene at 290 °C. This catalyst shows higher activity at all the reaction conditions tested and gives highest yield of ethene 15 % at 310 °C. Catalyst $Mo_1V_{0.40}$ is more active, as reported by many researchers, than a catalyst with a 2.5:1 molar ratio of Mo: V in a molybdenum and vanadium mixed oxides catalyst which has 5 % ethane conversion with 86 % selectivity to ethene at similar process conditions [1-2].

In a recent study, a bimetallic catalytic system prepared with 2.5:1 ratio of molybdenum vanadium did not give 100 % ethene selectivity even at the lowest ethane conversion. Using $Mo_8V_2Nb_1O_x$, Thorsteinson reported 100 % ethene selectivity for a ratio (2.5:1) of molybdenum vanadium in mixed metal oxides compositions, although the experimental conditions are in that case very dissilar to the conditions used in the present experiments.

3.2.2 Effect of feed composition on the catalytic activity

Based on the result of tests (Table 3.2 - 3.4), $Mo_1V_{0.40}$ was selected as an optimum catalyst and used for further studies. In the first instance, the feed composition was changed in order to see the effect of ethane concentration on the catalyst performance. Four different ethane concentrations were introduced into the feed gas while the oxygen concentration was kept constant in the feed gas. Feed concentrations ratio is given in Table: 3.5.

Table 3.5: Ethane concentration variation in the feed gas.

Feed Gas	Mole (%)			
	Feed-1	Feed-2	Feed-3	Feed-4
Ethane	50	40	30	15
Oxygen	10	10	10	10
Nitrogen	40	50	60	75

In these experiments, the catalyst ($Mo_1V_{0.40}$) was tested for four different feed gas composition at different reaction temperatures (250 – 310 ºC) to optimize the feed gas ratio.

3.2.2.1 Ethane concentration impact at 250 ºC.

Table 3.6: Testing results with varying ethane concentration in the feed at 250 ºC

Feed	Conv. (%)		Selectivity (%)				Yield (%)
Ref.	C_2H_6	O_2	CO_2	CO	C_2H_4	AA	C_2H_4
Feed-1	6.9	25.8	2.6	5.4	75.6	16.4	5.2
Feed-2	8.9	36.4	3.1	5.7	77.1	14.1	6.9
Feed-3	13.4	30.7	5.3	7.1	69.8	17.8	9.4
Feed-4	17.3	23.1	6.9	8.3	65.3	19.5	11.3

Reaction conditions: Pressure = 70 psig, temp. = 250 ºC, catalyst wt. = 1 g, feed flow = 25 ml/min.

3.2.2.2 Ethane concentration impact at 270 ºC.

Table 3.7: Testing results with varying ethane concentration in the feed at 270 ºC

Feed	Conv. (%)		Selectivity (%)				Yield (%)
Ref.	C_2H_6	O_2	CO_2	CO	C_2H_4	AA	C_2H_4
Feed-1	13.3	46.6	3.1	6.1	68.7	22.1	9.2
Feed-2	16.7	60.4	5.4	6.6	69.6	18.4	10.2
Feed-3	18.2	56.1	6.9	7.6	63.6	21.9	11.6
Feed-4	22.4	41.6	8.8	9.6	55.8	25.8	12.5

Reaction conditions: Pressure = 70 psig, temp. = 270 ºC, catalyst wt. = 1 g, feed flow = 25 ml/min.

At low temperature (250 - 270 ºC), when the ethane and oxygen ratio changes from 50:10 to 15:10 in the feed gas the ethane conversion increases from 7 to 22 % and the distribution of other products is slightly affected by the change in the feed composition. With a fixed concentration of O_2 in the feed, the oxygen conversion increases with

increasing concentration of ethane. Ethene selectivity behavior depends mainly on ethane conversion but COx behaves different and show highest ethene selectivity with Feed-2 (composition of ethane 40 %, oxygen 10 % and nitrogen 50 %) with low selectivities of COx and AA.

3.2.2.3 Ethane concentration impact at 290 ºC.

Table 3.8: Testing results with varying ethane concentration in the feed at 290 ºC.

Feed	Conv. (%)		Selectivity (%)				Yield (%)
Ref.	C_2H_6	O_2	CO_2	CO	C_2H_4	AA	C_2H_4
Feed-1	17.8	67.5	4.5	7.1	59.4	29	10.6
Feed-2	21.8	80.2	6.4	8.1	66.5	20.3	14.5
Feed-3	24.7	69.7	9.9	9.6	56.6	23.9	14
Feed-4	27.4	51.3	12.1	11.7	49.1	28.2	13.5

Reaction conditions: Pressure = 70 psig, temp. = 290 ºC, catalyst wt. = 1 g, feed flow = 25 ml/min.

3.2.2.4 Ethane concentration impact at 310 ºC.

Table 3.9: Testing results with varying ethane concentration in the feed at 310 ºC.

Feed	Conv. (%)		Selectivity (%)				Yield (%)
Ref.	C_2H_6	O_2	CO_2	CO	C_2H_4	AA	C_2H_4
Feed-1	22.2	95.6	6.2	7.6	57.3	28.9	12.7
Feed-2	23.9	98.6	8.6	10.4	60.9	20.1	14.6
Feed-3	28.6	95.7	11.3	10.9	51.1	27.1	14.5
Feed-4	33.6	91.4	18.2	13.2	40.7	29.9	13.7

Reaction conditions: Pressure = 70 psig, temp. = 310 ºC, catalyst wt. = 1 g, feed flow = 25 ml/min.

Catalytic activity tested at all temperatures shows that the catalyst has highest selectivity to ethene with Feed-2 with low carbon oxide formation. Catalyst activity increases with decreasing concentration of ethane in the feed and the selectivity to ethene also decreases

with the formation of more carbon oxide in the products. Hoever, there is no significant change in the acetic acid formation. With a fixed concentration of oxygen in the feed, the oxygen conversion increases with increasing concentration of ethane.

As expected, the ethane conversion is increased with temperature to a maximum at 290 °C and then remained more or less constant. This levelling-off appears to be due to non-availability of surplus oxygen in the reaction mixture. However, the ethane conversion is highest in Feed-4 (ethane 15 %) with high carbon monoxide and carbon dioxide selectivities of 13 % and 18 % respectively at 310 ºC, while Feed-2 (ethane 40 %) shows highest activity in terms of having high selectivity to ethene with low carbon oxide formation. The catalyst activity increases with decreasing ethane concentration in the feed from 50 % to 15 % whilst generating a large amount of carbon oxide and low ethene formation with no significant changes in acetic acid selectivity.

3.2.3 Temperature effect on catalyst ($Mo_1V_{0.40}$) activity.

Fig. 3.1 shows clearly the temperature dependence of ethane conversion to ethene, carbon dioxide and carbon monoxide selectivities for tested temperatures (250 - 310 ºC) for the $Mo_1V_{0.40}$ catalyst with 25 ml/min. of Feed-2. Ethene selectivity decreases rapidly with increasing temperature, while carbon oxide and AA selectivities increase slightly.

However, low (250 ºC) temperature reaction shows low ethane conversion with high selectivity to ethene and low formation of carbon oxide and AA. At higher temperatures (310 ºC), selectivity of ethene decreases as the deep oxidation starts and increases carbon oxide and AA formation.
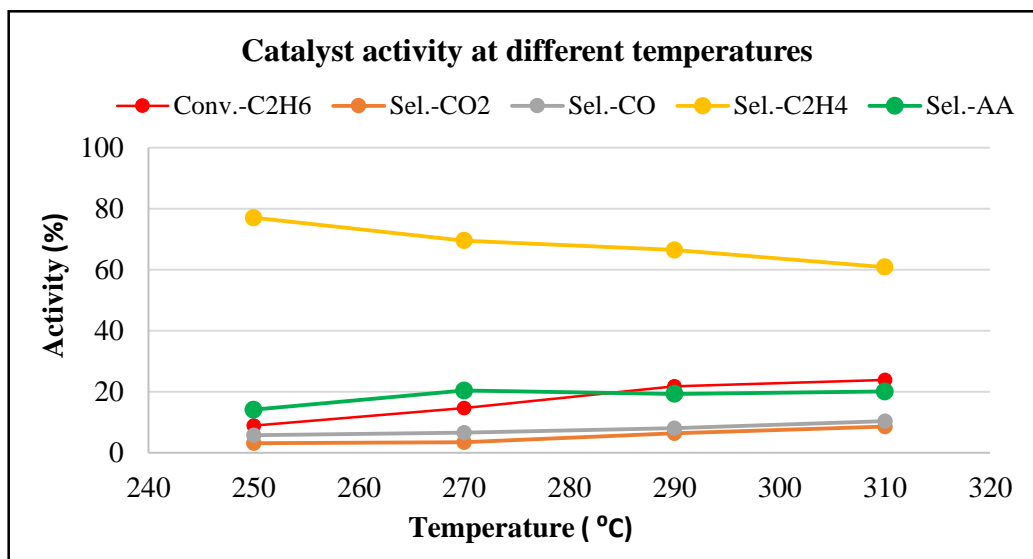
Fig.3.1: $Mo_1V_{0.40}$ catalyst activity with Feed-2 at different temperature .

3.2.4 Pressure effect on catalyst ($Mo_1V_{0.40}$) activity.

Selected catalyst ($Mo_1V_{0.4}$) was further tested at different pressures from atmospheric to 200 psig to observe catalytic behavior. Catalytic data shows that the catalyst activity at atmospheric pressure is moderate but has high selectivity to ethene at three different temperatures tested. At atmospheric pressure, the catalytic activity increases with temperature with a slight increase in both carbon oxide and acetic acid formation.

(i) Catalytic activity data at atmospheric pressure.

Catalytic activity is low at atmospheric pressure and at low temperatures. However, at high temperatures ethane conversion is high with high ethene yield. Low pressure favours lower selectivity to the CO_x and acetic acid, however this slightly increases with temperature. At atmospheric pressure, the most favourable condition is a high temperature which results in a high ethane conversion with a high yield of ethene.

Table 3.10: Temperature impact on catalytic activity at atmospheric pressure.

Temp.	Conv. (%)		Selectivity (%)				Yield (%)
(°C)	C_2H_6	O_2	CO_2	CO	C_2H_4	AA	C_2H_4
270	10.2	26.5	5.9	9.6	74.3	10.2	7.6
290	16.7	58.4	7.3	12.1	68.2	12.4	11.4
310	21.0	88.6	8.9	15.3	61.5	14.3	12.9

Reaction conditions: Pressure = atmospheric, feed gas = ethane: oxygen: nitrogen (50:10:40), catalyst wt. = 1 g, feed flow = 25 ml/min.

(ii) Catalytic activity data at 70 psig pressure.

At 70 psig, catalyst activity slightly increases at the three tested temperatures as compared to atmospheric pressure test. At this pressure, the catalyst shows higher acetic acid formation which also increases with temperature, whilst the carbon oxide selectivity remains low. Catalyst performance data at the three different temperatures and constant pressure (70 psig) are given in Table 3.11.

Table 3.11: Temperature impact on catalytic activity at 70 psig pressure.

Temp.	Conv. (%)		Selectivity (%)				Yield (%)
(°C)	C_2H_6	O_2	CO_2	CO	C_2H_4	AA	C_2H_4
270	13.3	43.6	5.5	7.8	69.9	16.8	10.1
290	17.8	67.5	6.4	8.8	66.4	18.4	13.8
310	22.2	95.6	7.2	11.6	58.3	22.9	12.9

Reaction conditions: Pressure = 70 psig, feed gas = ethane: oxygen: nitrogen (50:10:40), catalyst wt. = 1 g, feed flow = 25 ml/min.

(iii) Catalytic activity data at 140 psig pressure.

At 140 psig, the catalytic activity is higher than at 70 psig. The acetic acid selectivity increases with higher temperature, whilst carbon oxide formation increases marginally. At 200 psig, the catalytic activity remains similar to that at 140 psig, while AA and CO_x have higher selectivity, both increasing with greater temperature.

Table 3.12: Temperature impact on catalytic activity at 140 psig pressure.

Temp.	Conv. (%)		Selectivity (%)				Yield (%)
(ºC)	C_2H_6	O_2	CO_2	CO	C_2H_4	AA	C_2H_4
270	16.0	58.1	5.2	6.8	65.3	22.7	10.5
290	23.6	93.1	6.8	7.7	59.4	26.1	14
310	25.4	98.3	10.0	8.2	52.5	28.3	13.4

Reaction conditions: Pressure = 140 psig, feed gas = ethane: oxygen: nitrogen (50:10:40), catalyst wt. = 1 g, feed flow = 25 ml/min.

(iv) Catalytic activity data at 200 psig pressure.

Table 3.13: Temperature impact on catalytic activity at 200 psig pressure.

Temp.	Conv. (%)		Selectivity (%)				Yield (%)
(ºC)	C_2H_6	O_2	CO_2	CO	C_2H_4	AA	C_2H_4
270	18.5	67.8	10.7	7.6	57.9	23.8	10.7
290	24.5	95.6	11.2	8.9	53.1	26.8	13
310	26.1	99.6	12.9	9.3	47.5	30.3	12.4

Reaction conditions: Pressure = 200 psig, feed gas = ethane: oxygen: nitrogen (50:10:40), catalyst wt. = 1 g, feed flow = 25 ml/min.
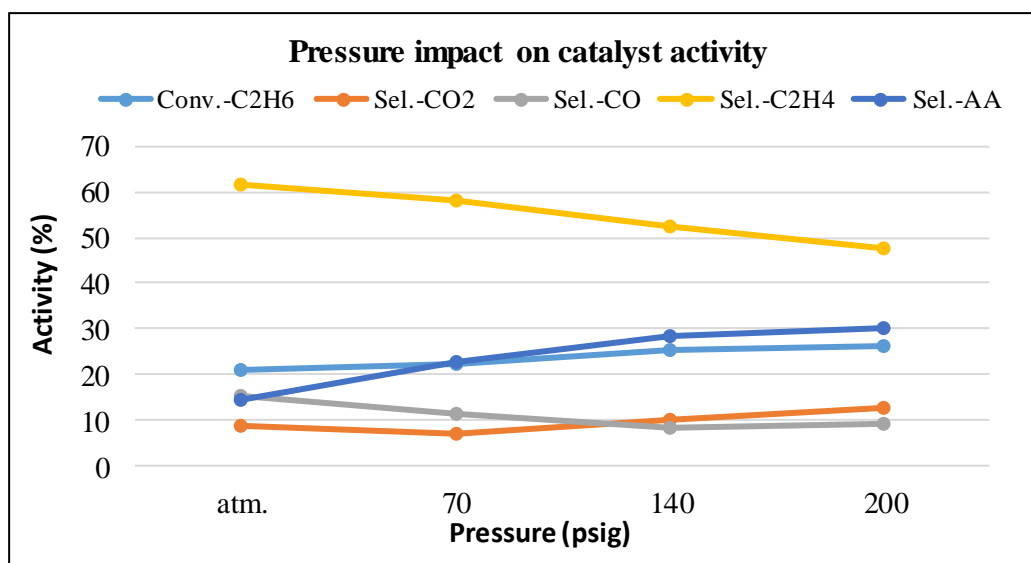
Fig.3.2: Pressure impact on $Mo_1V_{0.4}$ catalyst activity at 310 ºC.

At high temperature (310 ºC), high pressure favours acetic acid selectivity and this increases rapidly when pressure increases from atmospheric to 200 psig, as shown in Fig. 3.2. However, at 310 ºC, ethane conversion and carbon oxide selectivity do not change significantly at higher pressure (140 – 200 psig) and shows that high pressure is not favourable for the ODH of ethane as shown in Fig. 3.2.

3.3 Gas hourly space velocity (GHSV) impact on the catalyst activity

The selected catalyst ($Mo_1V_{0.4}$) was tested for ethane ODH at different temperatures (270, 290, 310 and 330 ºC) with different feed flows to see the GHSV impact on the catalyst activity and selectivity to ethene.

3.3.1 Experimental results and discussions

Catalytic results were obtained for the ODH of ethane to ethene at different GHSVs are shown in Tables 3.14 - 3.17 at atmospheric pressure. Ethene, carbon dioxide and carbon monoxide, acetic acid (AA) were the main reaction products. At atmospheric pressure, ethene selectivity remains high, while the AA and COx selectivities were low at all tested temperature. From these results, it can be concluded that the activity decreases as GHSV increases. The catalytic activity increases with increasing temperature but the ethene selectivity decreases.

Ethane conversion levels were varied by changing the GHSV to determine the relative contributions of primary and secondary reaction pathways to ethene, CO_x and AA formation. Acetic acid selectivity first increased slightly then fell again with increasing GHSV by 4-7 % while ethene selectivity concurrently decreased (from 89 to 77 %), consistent with involvement of the ethene as a reactive intermediate [3, 4]. The non-zero acetic acid selectivity, evidenced by extrapolation to lower ethane conversion (Fig. 3.3),

suggest, however, that a substantial fraction of AA forms via direct oxidation of ethane [5]. At high GHSV, ethene selectivity increases but AA selectivity does not.

Table 3.14: GHSV impact at 270ºC, and at atmospheric pressure.

GHSV	Conv. (%)		Selectivity (%)				Yield (%)
(h^{-1})	C_2H_6	O_2	CO_2	CO	C_2H_4	AA	C_2H_4
780	9.3	29.8	7.5	11.5	76.7	4.3	8.7
1350	6.5	16.6	5.8	8.4	80	5.9	5.2
1620	5.4	12.2	5	6.9	81.7	6.4	4.4
1890	4.8	10.9	4.1	5.9	83.8	6.2	4.0
2250	4	9.6	3.5	5	85.9	5.6	3.4
3000	2.9	5.4	2.8	3.9	88.7	4.6	2.6

Reaction conditions: Pressure = atmospheric, Temp. = 270ºC, feed gas = ethane: oxygen: nitrogen (50:10:40), catalyst wt. = 1 g.
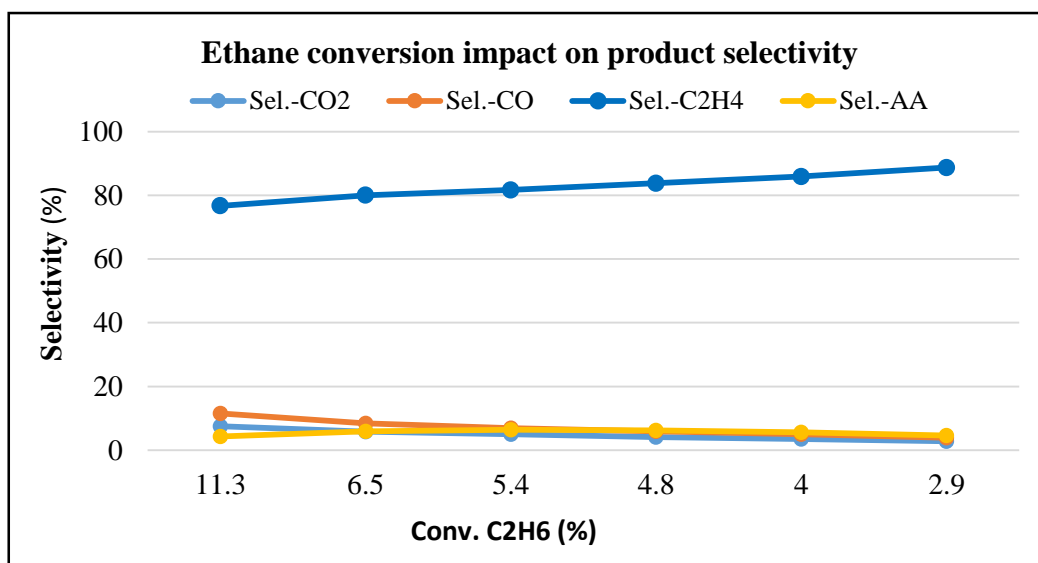
Fig.3.3: Ethane conversion versus products selectivity at 270 °C.

Reaction temperatures were varied to see the GHSV impact on catalytic activity of the catalyst, and the data is presented in Tables 3.14 - 3.17. Ethane conversion increases with increasing temperature at all tested GHSVs. However, there is no significant change in

AA selectivity at these reaction temperatures. The CO_x selectivity increases rapidly with increasing ethane conversion and reaction temperature [6].

Table 3.15: GHSV impact at 290 ºC and at atmospheric pressure.

GHSV	Conv. (%)		Selectivity (%)				Yield (%)
(h^{-1})	C_2H_6	O_2	CO_2	CO	C_2H_4	AA	C_2H_4
780	15.6	39.9	8.9	13.5	72.1	5.5	11.2
1350	9.8	18.2	7.3	8.7	76.2	7.8	6.1
1620	7.6	16.0	5.1	7.1	79.2	8.5	5.2
1890	6.3	14.6	4.9	6.8	80.9	7.4	4.4
2250	5.1	13.6	4.7	6.1	82.1	7.1	4.2
3000	4.7	12.7	3.8	5.9	83.3	6.9	3.9

Reaction conditions: Pressure = atmospheric, Temp. = 290ºC, feed gas = ethane: oxygen: nitrogen (50:10:40), catalyst wt. = 1 g.

Activity result at 290 °C and atmospheric pressure show that the conversion decreases as the GHSV increases. Temperature impact at atmospheric pressure has a much lower impact on the AA selectivity, while the carbon oxide selectivity significantly changes with GHSV. Similar trends were observed when catalysts were tested at 310 and 330 °C. However, high reaction temperature favours greater carbon oxide (CO_x) formation.

Table 3.16: GHSV impact at 310 ºC and at atmospheric pressure.

GHSV	Conv. (%)		Selectivity (%)				Yield (%)
(h^{-1})	C_2H_6	O_2	CO_2	CO	C_2H_4	AA	C_2H_4
780	18.2	54.8	13.6	17.1	62.5	6.8	11.4
1350	13.9	48.7	8.3	13.6	69.7	8.5	9.7
1620	10.6	42.3	7.4	12.2	71.7	8.7	7.8
1890	9.3	35.2	6.9	11.2	72.5	9.4	6.4
2250	7.9	31.7	6.6	11	73.2	9.1	5.8
3000	6.3	22.3	6.3	9.5	75.4	8.9	4.8

Reaction conditions: Pressure = atmospheric, Temp. = 310ºC, feed gas = ethane: oxygen: nitrogen (50:10:40), catalyst wt. = 1 g.

Table 3.17: GHSV impact at 330 ºC and at atmospheric pressure.

GHSV	Conv. (%)		Selectivity (%)				Yield (%)
(h^{-1})	C_2H_6	O_2	CO_2	CO	C_2H_4	AA	C_2H_4
780	25.4	92.0	12	19.2	59.6	9.1	16.3
1350	20.1	64.7	10.2	18.2	62.8	8.9	12.6
1620	17.8	59.3	9.4	16.4	65	9.2	11.7
1890	15.4	55.3	9	15.7	67	8.3	10.3
2250	13.5	50.9	8.9	15.2	68.1	7.8	9.2
3000	10.8	36.7	7.9	11.7	72.8	7.5	7.9

Reaction conditions: Pressure = atmospheric, Temp. = 330ºC, feed gas = ethane: oxygen: nitrogen (50:10:40), catalyst wt. = 1 g.

The catalyst was tested at two different pressures; atmospheric and 70 psig at constant temperature (270 °C). The main impact of reaction pressure was on the selectivity to acetic acid. In the product distribution, ethene selectivity decreases due to an increase in AA formation, whilst ethane conversion increases from 3-11 % to 8-20 % at different GHSVs. Results are presented in Tables 3.14 and 3.18.

Table 3.18: GHSV impact at 270ºC and at 70 psig pressure.

GHSV	Conv. (%)		Selectivity (%)				Yield (%)
(h^{-1})	C_2H_6	O_2	CO_2	CO	C_2H_4	AA	C_2H_4
780	20	98.6	8.8	12.7	61.2	17.3	12.2
1350	15.8	56.5	6.3	9	69	15.6	10.9
1890	12	36.8	4.8	7.7	71.8	15.8	8.6
2250	10.5	30.1	4.4	7.1	72.8	15.6	7.6
3120	9.4	25.3	4	6.6	74.5	15	7
3630	7.9	21.2	3.1	5.4	76.7	14.7	6.1

Reaction conditions: Pressure = 70 psig, Temp. = 270ºC, feed gas = ethane: oxygen: nitrogen (50:10:40), catalyst wt. = 1 g.

Fig. 3.4 shows that the ethane conversion is inversely related to GHSV. This study was also conducted at various temperatures. These results suggest that the oxidation of ethane occurs mainly at the catalyst surface through a heterogeneous mechanism, and that the product formation does not inhibit the reaction [7]. The yield of ethene (C_2H_4) product increases proportionally with decreasing GHSV, whilst AA formation does not increase significantly.

At higher GHSV the yield of C_2H_4 decreases whereas the carbon oxide yield increases significantly as result of ethene over-oxidation to carbon oxide. Therefore as the GHSV decreases the selectivity to carbon oxide increases and the selectivity to ethene decreases. However sum of these products remains unchanged.
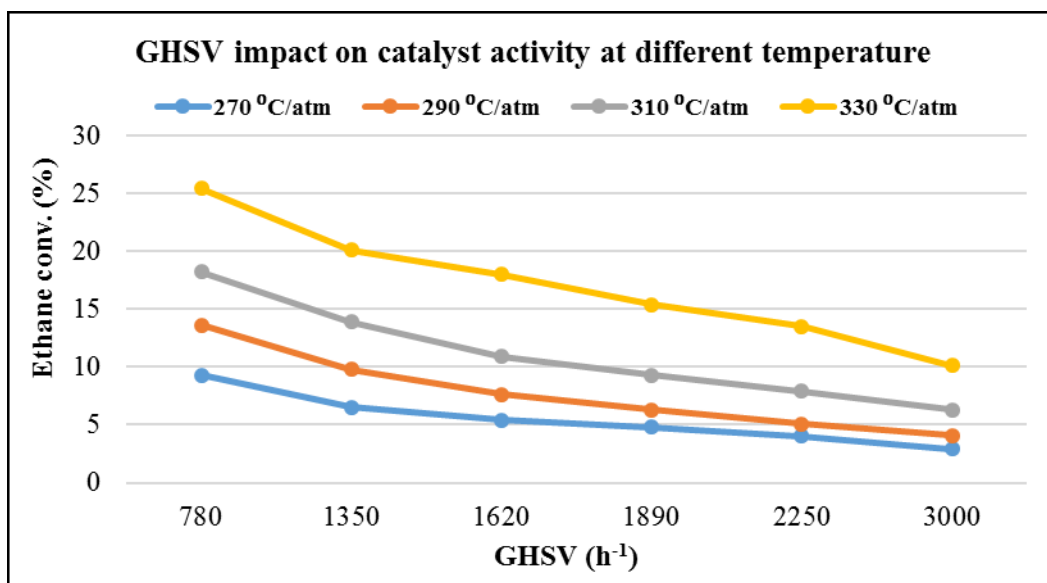
Fig.3.4: GHSV effect on ethane conversion at different temperatures.

3.3.2 Conclusion

Conversion of ethane decreases with increasing GHSV and hence ethene selectivity increases with the GHSV. Catalytic activity increases with increasing temperature. Catalytic performance data shows that by increasing temperature, there is a very small

change in AA (5 - 10 %) formation, whilst the carbon oxide formation increases drastically due to partial combustion reactions of ethene to CO_x [8]. Similar catalytic behavior is seen with decreasing GHSV.

Conversion of ethane also increases with increasing pressure. Data shows that pressure has a large impact on AA formation, whilst the carbon oxide has low formation. With increasing temperature or pressure, catalytic activity increases with a subsequent decrease in ethene selectivity, consistent with the involvement of ethene as a reactive intermediate for the formation of AA [9]. At lower ethane conversion, AA formation does not change significantly even at high reaction pressures.

3.4 Results of catalyst characterization

3.4.1 BET

The surface area (BET) of the catalyst was measured using Micrometrics ASAP2000 (Gemini) apparatus as described in Chapter 2. The surface area of these catalysts was in the range of 11-49 m^2/g as given in Table 3.19. Catalyst ($Mo_1V_{0.40}$) has a surface area of 21 m^2/g and shows high activity towards ethane oxidative hydrogenation to ethene.

Table 3.19: Surface area of catalysts varying with Mo and V ratio.

Cat. Ref.	Surface area (m^2/g)
$Mo_1V_{0.12}$	11
$Mo_1V_{0.25}$	17
$Mo_1V_{0.40}$	21
$Mo_1V_{0.60}$	49
$Mo_1V_{0.80}$	28
Mo_1V_1	26

The surface area of the catalyst increases with increasing Mo: V ratio until (1:0.6) after which it decreases. The surface area of the catalyst prepared with the lowest ratio of Mo and V (1:0.12) has a low surface area.

3.4.2 XPS

XPS was performed by using the Kratos Axis Ultra-DLD spectrometer as detailed in Chapter 2. The binding energies (BE) of O (1s), C (1s), Mo ($3d_{5/2}$), and V ($2p_{3/2}$) for MoV oxide catalysts are reported in Table 3.20. In the literature, the standard binding energy values are 232.2 ± 0.2 eV for (Mo^{6+}), 516.6 ± 0.1 eV for (V^{5+}), and 515.9 ± 0.4 eV for (V^{4+}) oxides and these match with literature [10-13].

Of the samples studied, the Mo photopeak is characteristic of Mo^{6+} by its binding energy (BE), while reduced Mo species such as Mo^{5+} (230.8-231.8 eV) or Mo^{4+} [10-11] are absent. XPS data as shown in Table 3.1 shows a good trends of V^{5+} and V^{4+} area ratio with the variation of metal (Mo : V) ratio. Area (%) of V^{5+} is higher when vanadium concentration was minimum ($Mo_1V_{0.12}$) and start decreasing till Mo: V (1: 0.25) and after that it increases with vanadium concentration. Same behavior with V^{4+}, first increases and then decrease with vanadium concentration. Concentration of both V^{5+} and V^{4+} is equal in catalytst $Mo_1V_{0.40}$ (1: 0.25).

Table 3.20: Binding energies of MoV catalysts calcined at 350°C.

Cat. Ref.	Name	BE (eV)	FWHM (eV)	Atom (%)
$Mo_1V_{0.12}$	O 1s	530.9	2.71881	48.91
	C 1s	284.9	3.28633	34.67
	$V2p_{3/2}$	516.9	2.67982	1.86
	$Mo3d_{5/2}$	232.9	5.06633	14.57
$Mo_1V_{0.25}$	O 1s	530.5	2.74981	49.78
	C 1s	284.5	2.93690	35.82
	$V2p_{3/2}$	516.5	2.75401	2.58
	$Mo3d_{5/2}$	232.5	5.09253	13.82
$Mo_1V_{0.40}$	O 1s	530.8	3.10955	50.24
	C 1s	284.8	3.51211	35.00
	$V2p_{3/2}$	516.8	2.65931	3.83
	$Mo3d_{5/2}$	232.8	5.22010	11.02
$Mo_1V_{0.60}$	O 1s	530.5	2.71903	50.18
	C 1s	284.5	2.94377	30.61
	$V2p_{3/2}$	516.5	2.80031	6.57
	$Mo3d_{5/2}$	232.5	5.09382	13.64
$Mo_1V_{0.80}$	O 1s	530.5	2.71534	49.78
	C 1s	284.5	3.10670	30.31
	$V2p_{3/2}$	516.5	2.87955	7.27
	$Mo3d_{5/2}$	232.5	5.35963	12.63
Mo_1V_1	O 1s	530.5	2.73434	52.39
	C 1s	284.5	2.89255	26.95
	$V2p_{3/2}$	516.5	2.80241	10.33
	$Mo3d_{5/2}$	232.5	5.28462	10.34

Table 3.21: XPS results concentration of V and Mo oxidation in the MoV catalysts.

Cat. Ref.		BE (eV)	FWHM (eV)	Area (%)
$Mo_1V_{0.12}$	$V2p_{3/2}$ - (V^{5+})	517.6	1.36403	70.02
	$V2p_{3/2}$ - (V^{4+})	516.4	1.32491	29.98
	$Mo3d_{5/2}$	233.2	1.24751	60.62
	$Mo3d_{3/2}$	236.3	1.25663	39.38
$Mo_1V_{0.25}$	$V2p_{3/2}$ - (V^{5+})	517.6	1.38655	59.29
	$V2p_{3/2}$ - (V^{4+})	516.5	1.34191	40.71
	$Mo3d_{5/2}$	233	1.32773	60.78
	$Mo3d_{3/2}$	236.2	1.32262	39.22
$Mo_1V_{0.40}$	$V2p_{3/2}$ - (V^{5+})	517.4	1.32661	48.72
	$V2p_{3/2}$ - (V^{4+})	516.4	1.41755	51.28
	$Mo3d_{5/2}$	232.7	1.35551	60.33
	$Mo3d_{3/2}$	235.9	1.36762	39.67
$Mo_1V_{0.60}$	$V2p_{3/2}$ - (V^{5+})	517.5	1.49801	64.82
	$V2p_{3/2}$ - (V^{4+})	516.4	1.30903	35.18
	$Mo3d_{5/2}$	232.9	1.36082	60.53
	$Mo3d_{3/2}$	236.1	1.36804	39.47
$Mo_1V_{0.80}$	$V2p_{3/2}$ - (V^{5+})	517.6	1.45093	75.07
	$V2p_{3/2}$ - (V^{4+})	516.3	1.17484	24.93
	$Mo3d_{5/2}$	233.1	1.46575	60.51
	$Mo3d_{3/2}$	236.2	1.45663	39.49
Mo_1V_1	$V2p_{3/2}$ - (V^{5+})	517.6	1.40334	74.72
	$V2p_{3/2}$ - (V^{4+})	516.3	1.20861	25.28
	$Mo3d_{5/2}$	233	1.47164	60.38
	$Mo3d_{3/2}$	236.1	1.47037	39.62

The comparison of atomic ratios in the MoV catalyst series reveals the influence of vanadium on the surface composition. The addition of V to Mo (V/Mo = 0.20 to 1.0), results in an increase in the amount of vanadium present on to the surface of the catalyst (and also show that the amount of molybdenum on the surface decreases).The amount of

oxygen determined from the surface composition is lower than when calculated from the bulk stoichiometry, when all V assumed to be V^{4+}. The relative amounts of V^{5+} and V^{4+} are given in Tables 3.21 and 3.22 after peak decomposition.

Table 3.22: XPS experiments atomic ratios and stoichiometry of MoV catalysts.

Catalyst	BE (eV)			Atomic ratios			
Ref.	Mo^{6+}	V^{5+}	V^{4+}	V/Mo	O/V	O/Mo	V^{5+}/V_{total}
$Mo_1V_{0.12}$	233.2	517.6	516.4	0.20	13.67	3.36	0.70
$Mo_1V_{0.25}$	233.0	517.6	516.5	0.26	13.07	3.38	0.59
$Mo_1V_{0.40}$	232.7	517.4	516.4	0.36	14.73	5.33	0.49
$Mo_1V_{0.60}$	232.9	517.5	516.4	0.41	9.01	3.68	0.65
$Mo_1V_{0.80}$	233.1	517.6	516.3	0.58	6.85	3.94	0.75
Mo_1V_1	233.0	517.6	516.3	1.00	5.07	5.07	0.75

The V^{5+}/V^{total} ratio ranges from 0.49-0.75 as shown in Table 3.22, which shows the reducibility of vanadium. When the catalysts are prepared with a moderate amount of vanadium ($V_{0.25}$-$V_{0.60}$), this ratio is lower than the catalysts containing lower or higher vanadium content. This means that the reducibility has increased, which may be a result of less vanadium present in the mixed MoV phase(s). The use of a vacuum, necessary in XPS apparatus, is also known to induce the reduction of some V^{5+}, but this occurs only if these ions are not properly stabilized in an oxide matrix [14]. The relative amount of V^{4+} is highet in the catalyst $Mo_1V_{0.25}$, which means that the number reducible vanadium sites are greatest. The amount of V^{4+} decreases at greater concentrations of vanadium and in the $Mo_1V_{0.12}$ catalyst.

3.4.3 XRD

XRD patterns of the materials were obtained as described in Chapter 2. X-ray diffraction patterns of all catalysts are presented in Fig.3.5.

In XRD, two main types of diffraction patterns are observed as the ratio of Mo:V in the catalysts is varied (Fig. 3.5); (i) crystalline patterns for samples with a low vanadium content, (ii) almost amorphous patterns for the catalyst with 0.25 vanadium content. A commn feature to all MoV catalysts is the presence of peaks at d (Å) / 2θ = 3.46 / 25.7°.

Many α-MoO$_3$ phases have been identified in the catalysts containing a vanadium ratio of 0.12 and 1 as shown in Fig. 3.5. The majority of the α-MoO$_3$ peaks are shifted compared to the standard pattern (JCPDS 76-1003) which may be the result of a modification by vanadium, V$_x$Mo$_{1-x}$O$_{3-0.5x}$ or due to the formation of oxygen vacancies, such as MoO$_{3-x}$. While the materials prepared with varying vanadium ratio are similar, a common phase is due to the hexagonal defective oxide h-MoO$_3$, their XRD patterns being very similar to V$_{0.12}$Mo$_{0.88}$O$_{2.94}$ catalyst (JCPDS 81-2414).
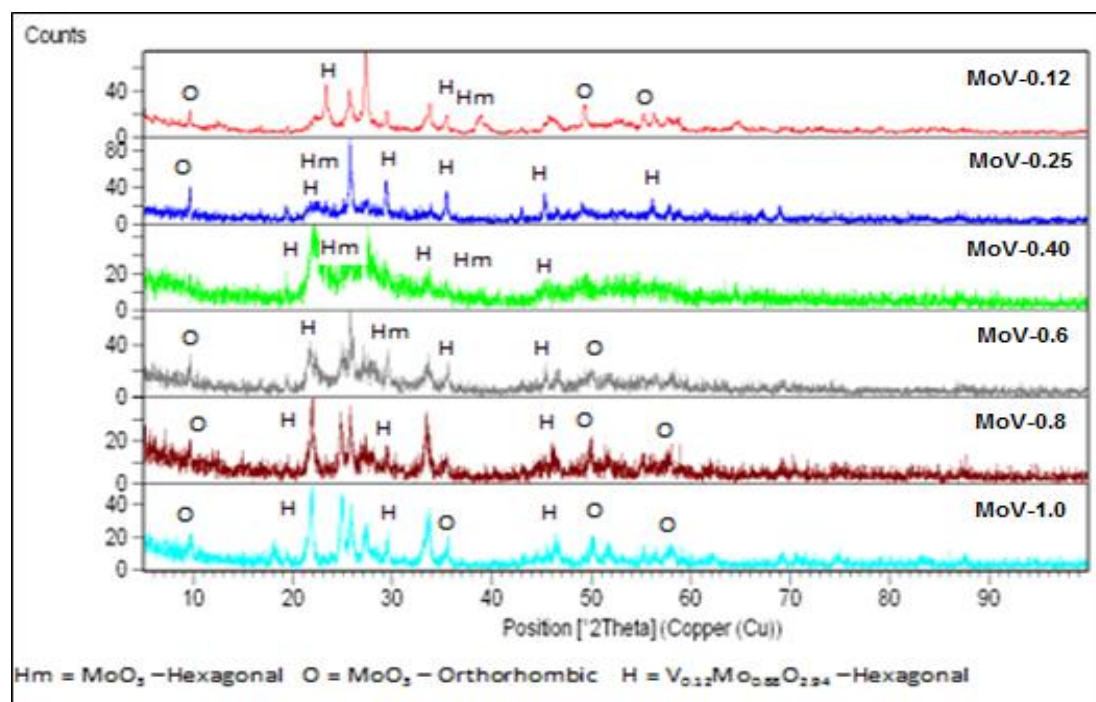
Fig.3.5: XRD patterns of catalysts varying with (MoV) molar ratio.

The pattern of Mo$_1$V$_{0.40}$ catalyst exhibits a disordered character (Fig. 3.5); several broad reflections at d-spacing [Å] 10.55, 3.95, 3.27 and 1.8 have been assigned to particles of α-

MoO$_3$ by Mestl [15], emphasising the nanocrystalline character of that material. Peaks at $2\theta \approx 7.8$, 8.7 and 22.2° (the latter being the most intense) correspond to (200), (210) and (001) planes and are characteristic of the θ-Mo$_5$O$_{14}$ structure [16]. The pattern of V$_6$Mo$_4$O$_{25}$ (JCPDS 34-0527) shows intense reflections at d (Å)/2θ = 10.92/8.08 and 4.00/22.2°. This is very close to that of (Nb$_{0.09}$Mo$_{0.91}$)O$_{2.80}$ (JCPDS 27-1310) which occurs with the catalyst V/Mo=0.12. Because of the amorphous character of the pattern, it is not possible to determine whether (Mo-X)$_5$O$_{14}$ (JCPDS 31-1437), (V$_{0.95}$Mo$_{0.97}$)$_5$O$_5$ (JCPDS 77-0649) or a ternary solid solution VOMoO$_4$ (JDPDS 18-1454) are the closest matching structure. The pattern of Mo$_1$V$_{0.40}$ (Fig. 3.5) exhibits the main peaks of h-MoO$_3$ (or of V$_x$Mo$_{1-x}$O$_3$-$_{0.5x}$) superimposed on the preceding pattern.

3.4.4 SEM

MoV based catalysts were analyzed for surface morphology using SEM as described in Chapter 2. The SEM images reveal that large parts of the MoV mixed oxide consist of coarse and irregularly shaped particles.

The catalyst sample Mo$_1$V$_{0.12}$ was composed of both coarse and fine irregularly shaped particles (Fig. 3.6). The surface of the particles contained cracks and bundles of thin flake like crystals arranged in a flower-like morphology. All of the remaining catalyst samples were composed of irregular shaped particles of variable size. For catalyst sample Mo$_1$V$_{0.25,}$ the individual particles had both rough and smooth sides. The surface contained cracks and fine irregularly shaped particles. The surface of catalyst sample Mo$_1$V$_{0.40}$ contained cracks and fine irregularly shaped particles.The individual particles of catalyst sample Mo$_1$V$_{0.60}$ had generally rough surfaces. The individual particles of catalyst sample Mo$_1$V$_{0.80}$ and catalyst sample Mo$_1$V$_1$ had both smooth and rough surfaces. The surfaces contained cracks and fused fine particles and long elongated flakes.
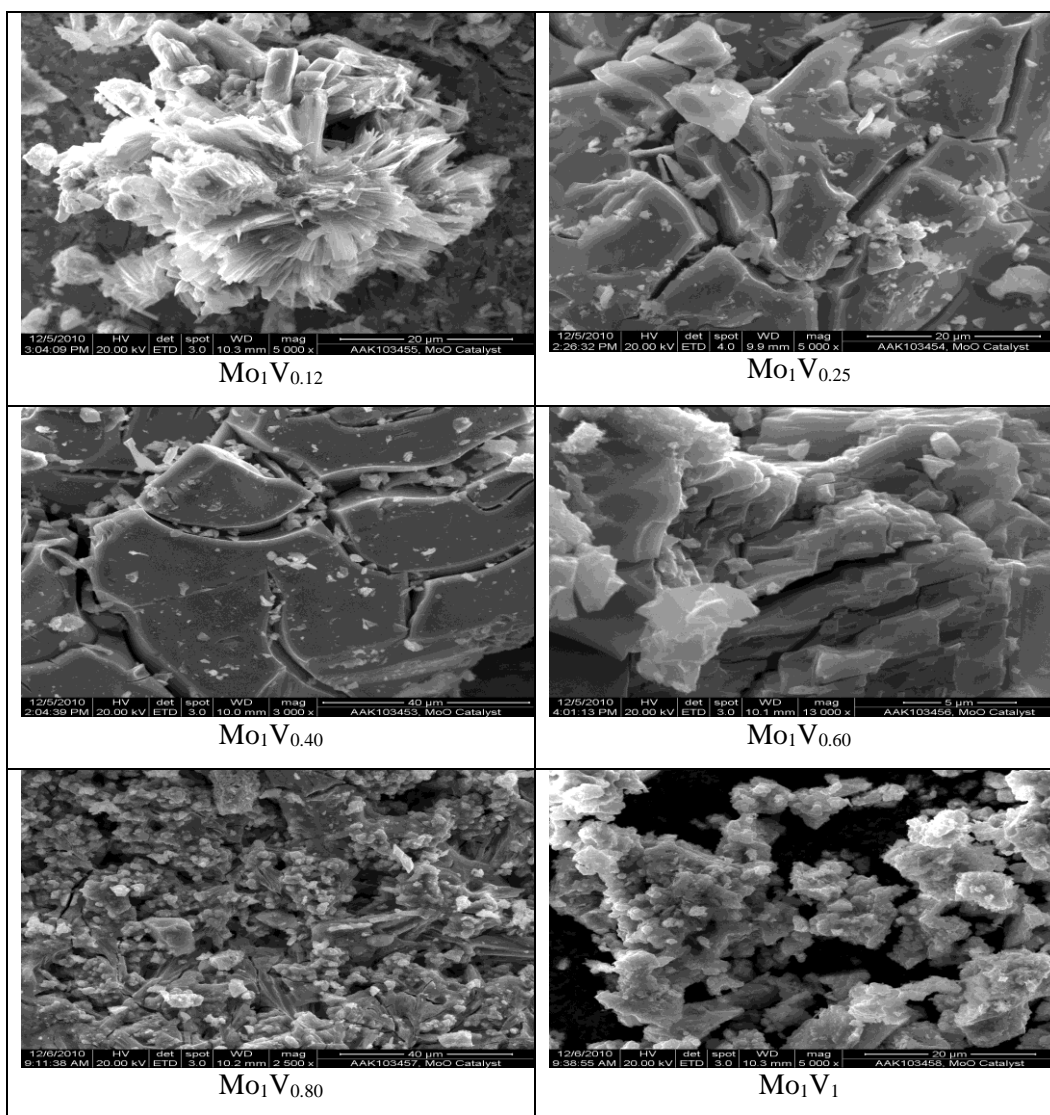
Fig.3.6: SEM images of catalysts with varying (MoV) molar ratio.

3.4.5 EDX

The elemental contents of surface particles were analyzed by EDX combined with SEM. Secondary electron (SE) imaging and backscattered electron (BSE) imaging modes of operation were used in combination with EDX analysis to investigate the elemental distribution of Mo, V and O. The elemental compositions of different regions in the BSE image were determined by EDX. The EDX analysis suggested the presence of O, Mo and

V in all catalysts that were prepared with varying vanadium concentration.Their surface compositions are given in Table 3.23.

Table 3.23: Elemental concentration (wt %) of the catalysts with varying MoV molar ratio.

Cat. Ref.	O	Mo	V
$Mo_1V_{0.12}$	33	61	6
$Mo_1V_{0.25}$	32	60	8
$Mo_1V_{0.40}$	30	58	12
$Mo_1V_{0.60}$	32	50	18
$Mo_1V_{0.80}$	31	48	21
Mo_1V_1	30	44	26

EDX analysis revealed that all catalysts contained both Mo and V and the matrix of material was confirmed which showed the presence of V in all samples. The variation in elemental concentration of Mo and V for all catalysts was comparable.

3.5 Discussion

In the present study results revealed that the activity and selectivity depends on the ratio of the base (MoV) binary components and it varies with the ratio. The catalytic activity data obtained show that the catalysts having 2.5:1 ratio of molybdenum and vanadium gives best results.

The catalytic properties of the mixed MoV oxide have been influenced by several parameters. The nature and the crystallinity of phases and the surface composition depend on the ratio of V/Mo, the method of preparation of the precursor and the calcination temperature. Chemical analyses show that the vanadium concentration is the determining factor for active phase formation. Extensive works carried out by Desponds [1] on the binary catalytic system prior to the addition of a third transition metal (Nb)

enhance the catalytic activity toward ethane ODH. Desponds [1] made a series $(Mo_4V_1O_x, Mo_4Nb_1O_x, V_5Nb_1O_x)$ of binary catalysts and found that $Mo_4V_1O_x$, was the most active catalyst. Desponds also prepared catalysts of $Mo_4V_1O_x$ with and without the addition of oxalic acid in the preparation step and discovered that catalysts prepared with oxalic acid performed better than those prepared without.

By comparing the catalytic activities and the ethene selectivities of the binary catalysts and the three component catalysts, it was shown that three component catalysts performbetter. This is an agreement with the findings of Burch and Swarnkar [17] who observed a strong improvement in the efficiency of the catalysts due to the addition of a third chemical component. Similarly, Thorsteinson et al. [2] found that the $Mo_8V_2Nb_1O_x$ catalyzed ethane oxidation exclusively to ethene at low temperature (215 ^{o}C), whereas a temperature of 500 ^{o}C was necessary for the catalyst without niobium. However this current study on binary catalyst systems proves that it is possible to achieve a high activity even at low temperatures without the addition of a third metal.

Moreover the activity and selectivity depend on the ratio of the base (MoV) binary components. A high activity is achieved with a Mo and V ratio of 2.5:1 and a third component can improve the ethene selectivity while the product distribution is not severely altered. If the ratio of Mo and V is changed from (2.5:1) then the activity and selectivity will decrease even after the addition of a third component (Nb). The superiority, in terms of selectivity, of a 2.5:1 ratio ofmolybdenum and vanadium is not unique in this case but improves greatly upon previous reports on binary catalytic system. Many examples can be found in the results published by Thorsteinson et al. [2], from binary to multicomponent with vanadium catalytic system.
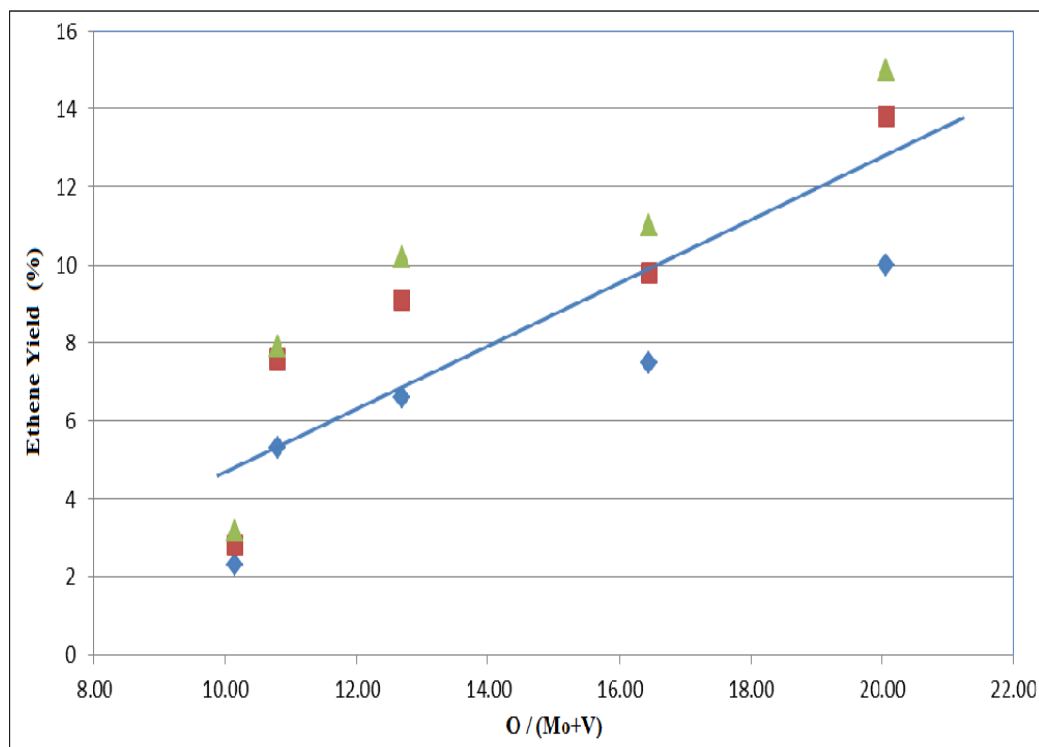
Fig.3.7: Plot of catalyst activity vs O/(Mo+V) ratio at different temperatures (◆ 270 ºC; ■ 290 ºC; ▲ 310 ºC).

The primary reason for the varying performances of the synthesized catalysts with different Mo/V ratios (Tables 3.1 -3.4) can be understood when the XPS results presented in Tables 3.20 and 3.21 are taken into consideration. Figure 3.7 shows the variation of catalyict activity with O / (Mo+V) ratios – the ratio of surface oxygen to base binary metal components at three temperatures. It is clear from Fig. 3.7 that catalytic activity, and hence the ethane conversion, increases with increasing O/(Mo+V) ratios, with an initial rapid increase before leveling off. The observed profile suggests that changes in O/(Mo+V) ratios determine the amount of O_2 available for ethane ODH. Further to this, the observed trend of Fig. 3.7 suggests that the dependency of ethane conversion on surface O_2 concentration is in agreement with previously published work by Dinse [18].
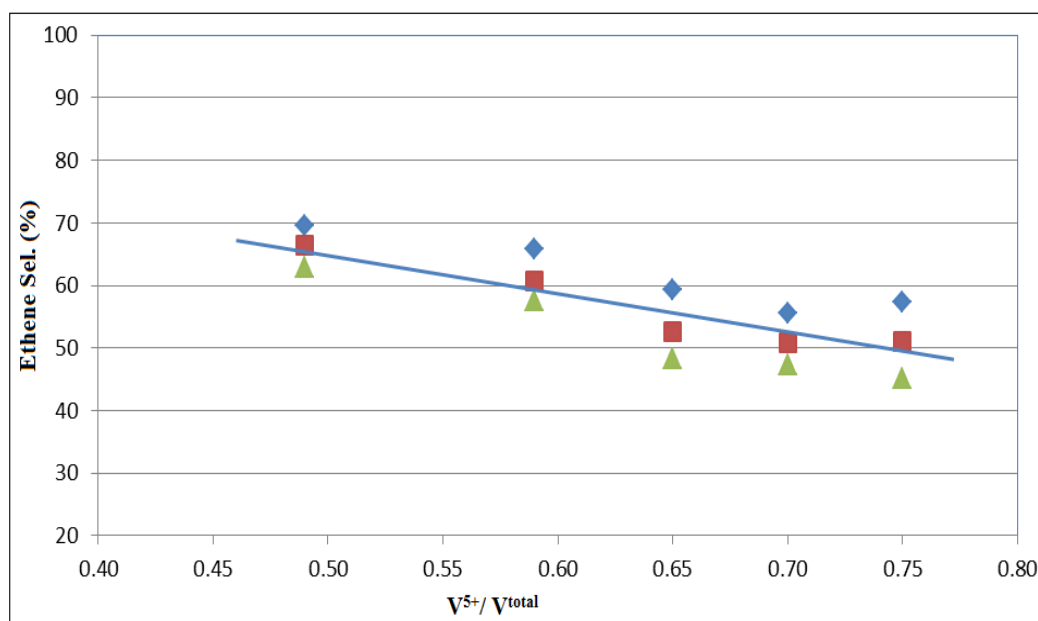
Fig.3.8: Catalyst selectivity vs V^{5+}/V^{total} ratio at different temperatures (◆ 270 ℃; ■ 290 ℃; ▲ 310 ℃).

The influence of the oxidation state of vanadium on ethane ODH selectivity can be seen by combining catalyst performance testing results with XPS results, as shown in Fig. 3.8. V^{5+}/V^{total} depicted in Fig. 3.8 is the ratio of vanadium in the 5+ oxidation state to total vanadium cations present (i.e., 4+ and 3+ states). It is assumed that a change in this ratio is due to the reduction of V^{5+} to V^{4+} and V^{3+}. It can be seen from Fig. 3.8 that, in general, ethane ODH selectivity decreases monotonically with an increasing ratio of V^{5+}/V^{total}. The observed trend can be rationalized by the adsorption strength and Lewis acidity of vanadium cations which decreases in the order $V^{5+} > V^{4+} > V^{3+}$ [18]. Due to the strong acidity of V^{5+}, it can be postulated that these cations adsorbed strongly to the catalyst surfaces causing some of the produced ethane to be further converted to secondary products, such as carbon oxide. In contrast, at lower ratios of V^{5+}/V^{total} the less strongly adsorbing V^{4+} and V^{3+} are more prevalent leading to minimal combustion of the ethene product to side products.

The catalytic activity data obtained in the present study show that an oxide mixture having 2.5:1 atomic proportion of molybdenum and vanadium gives the best results. The very low carbon dioxide and carbon monoxide selectivity observed with this ratio (2.5:1) indicates that the total oxidation of ethane is inhibited.

The tests performed on the binary series of catalysts composed of molybdenum and vanadium show several interesting features; $Mo_1V_{0.12}$ is the poorest catalyst of the series, Mo_1V_1 inhibits the total oxidation of ethane to carbon dioxide as compared the other ratios and $Mo_1V_{0.4}O_x$ catalysts are still the most efficient in the series of the binary catalysts. As reported by Oyama [19], the addition of a third component to the most active MoV system is not enough to have a significant effect on the activity; the rate of formation of carbon oxide is reduced as compared to $Mo_4V_1O_x$ catalysts.

According these findings, it appears that the activity and selectivity of these catalysts depend on the molybdenum and vanadium ratio. This ratio can be altered to considerably enhance the activity and selectivity by inhibiting the total oxidation reaction. In the present study, the 2.5:1 ratio between molybdenum and vanadium is optimum.

Thus, during the ODH of ethane it appears that carbon oxide are being formed mainly due to the direct oxidation of ethane and to lesser extent due to the secondary oxidation of ethene. This is in agreement with the findings of Burch et al. [17] who observed that most of the carbon monoxide and carbon dioxide was produced directly from ethane using their $Mo_1V_3Nb_1O_x$ catalyst. Lunsford [20] also observed on a lithium-promoted magnesium oxide catalyst that the oxidation of ethane yielded most of the carbon oxide formed during the reaction. Burch [17] reported a first order rate with respect to ethane partial pressure over a $Mo_6V_3Nb_1O_x$ catalyst. The reaction order with respect to oxygen showed a more complex pattern. The reaction order was almost independent of the

oxygen partial pressure at low temperature, whereas the reaction was half order for oxygen partial pressure below 1 psig at high temperature. The first order dependence with respect to the ethane partial pressure was consistent with a mechanism in which the breaking of a C-H bond is rate determining. The dependence of the oxygen reaction order on the temperature was explained in terms of lattice oxygen composition and the speed of reoxidation of the catalyst.

Therefore, at low ethane conversion and at low temperature, the reoxidation of the catalyst is so fast that it is not a rate limiting process. However, at high conversion of ethane at high temperature, the reoxidation is rate limiting if the oxygen partial pressure is low. This means that the reaction rate is dependent on oxygen partial pressure. The lability of the lattice oxygen had been demonstrated by Thorsteinson [2]. They also reported that the presence of vanadium increased the oxidation rate of the molybdenum dioxide. It has been found [17] using pulse experiments that molecular oxygen may be responsible for total oxidation of ethane whereas lattice oxygen is involved only in ethene formation.

It can be reasonably assumed that the breaking of a C-H bond is also rate limiting for the $Mo_1V_{0.40}$ catalyst and as a consequence, the reaction is first order with respect to ethane partial pressure for these catalysts. Therefore, the results obtained by varying ethane: oxygen ratio, which shows that the ethane conversion increases when the ethane: oxygen ratio is decreased from 5:1 to 1.5:1 in the feed. Moreover the rates of formation of the carbon oxide increased with oxygen partial pressure. At high oxygen partial pressure, the carbon oxide formation rate increases rapidly with increasing temperature.

Phases in the materials are primarily crystalline in the $Mo_1V_{0.12}$, $Mo_1V_{0.25}$, $Mo_1V_{0.80}$, and Mo_1V_1 catalysts and amorphous in $Mo_1V_{0.40}$ and $Mo_1V_{0.60}$, as shown in Fig. 3.3. During

calcination of the precursors up to 350 °C, the remaining oxalates and ammonium groups are eliminated as CO_2, and NH_3 or NO, depending on the atmosphere, heating rate and precursor type. In particular, it is well known [21] that the oxidation of ammonia to NO_x occurs because vanadium and or molybdenum undergo reduction. In the presence of vanadium, mixed hydrated hexagonal oxides isotopic to h-MoO_3, such as $A_xV_xMo_{1-x}O_3$ (x=0.13-0.20) and $H_xV_xMo_{1-x}O_3$ ($0.06 \leq x \leq 0.18$), have also been synthesized [22-23]. These phases are stable as long as ammonium or alkaline cations and/or protons remain in the channels. According to Dupont [22], the heating of $H_{0.13} V_{0.13} Mo_{0.87}O_3$ in air at 350 °C leads to the formation of hexagonal ($V_{0.13} Mo_{0.87}$)O_3, which is stable up to 460 °C. Moreover, the authors showed that above this temperature this solid is irreversibly transformed into a stable orthorhombic mixed oxide to α-MoO_3, which preserves the same V/Mo= 0.13/0.87 ratio. With the exception of α-MoO_3 which is most likely V-doped and V_2O_5 which are typically observed, hexagonal mixed oxides such as ($V_{0.12}$ $Mo_{0.88}$)$O_{2.94}$ or $V_{0.13} Mo_{0.87}$)$O_{2.925}$ remain stable.

Alternatively, θ-$(VMo)_5O_{14}$ could serve as a basis which would stabilize or isolate surface patches of $(Mo,V)O_x$. In both hypotheses, the main active sites are most likely to be the vanadium atoms, which according to XPS analyses contain a near surface slightly enriched with vanadium. In such cases the interphases must be coherent for the redox V^{5+}/V^{4+} to occur at the boundaries between θ-$(VMo)_5O_{14}$ and $(Mo,V)O_x$, or to help O^{2-} diffusion to the surface [24-26]. This redox system would proceed faster with an increased vanadium concentration or with the addition of other elements (Nb, Pd) to the catalytic system. The possibility of a complementary redox system between Mo^{6+} and Mo^{5+} at the steady state cannot be ruled out. However, if it proceeds, the rate of reoxidation of $Mo5^+$ to Mo^{6+} would be greatly enhanced by the neighboring vanadium, in the presence of which Mo^{5+} species are known to be rather unstable.

3.6 Conclusion

The present work, devoted to the study of MoV oxide catalysts, indicate that the composition and the properties of the catalytically active phases in the MoV oxide system are determined by the Mo:V ratio. A comparison of the catalytic properties and phase compositions indicate that the variation in the MoV oxide activity and selectivity can be due to variation in the phase compositions. However, solid solutions of MoO_3 in vanadium oxides have low catalytic activity and selectivity [27]. Compounds of vanadium and molybdenum shift the ethane ODH towards ethene formation and have different activity and selectivity depending on the phases formed during the catalyst preparation. Differences in the catalytic properties of these phases can be due to many factors: structure, Mo: V ratio, oxygen binding energies, valance state of vanadium and molybdenum, etc.

The type, amount and characteristics of the oxides, identified by several methods of analysis, depend on the vanadium concentration in Mo-containing catalysts. The catalysts are characterized by the presence of several crystalline oxide structures including hexagonal and orthorhombic (α-MoO_3) molybdenum trioxide, which are likely to contain vanadium. Varying the vanadium concentration in the Mo V catalysts affects the stability of these crystalline oxides. This is particularly evident in the case of hexagonal MoO_3 (or h-$Mo_{1-x}V_xO_{3-0.5}$) which formsα-MoO_3 (or α-$Mo_{1-x}V_xO_{3-x/2}$), resulting in a lower catalytic performance [28-31]. The catalysts which have 1: 2.5 ratio of vanadium to molybdenum have amorphous structures that are likely to be composed of nanocrystalline $Mo_{1-x}V_xO_{3-0.5}$ oxides. The high degree of disorder in the stacking of these layered oxides is attributed to ions of V, sandwiched between the layers if they are not inserted in the constituent oxides. The catalysts with a 1:2.5 vanadium ratio in molybdenum ($Mo_1V_{0.40}$), are more selective to ethene and mildly selective to oxidation products (CO_2) and which is due to

synergetic effects instead of the very specific properties of any given phases [32-38]. Indeed, the fact that an excess of vanadium and molybdenum, compared to the known θ-$V_{0.07}Mo_{0.93}O_{2.80}$ or $V_{0.13}Mo_{0.87}O_{2.925}$ is needed to ensure high catalytic performance in ethane oxidation, must also be taken into account.

The $Mo_1V_{0.12}$ and Mo_1V_1 catalysts have low activity at the tested operating process conditions. The range of conversion of ethane is smaller ($Conv._{C2H6} = 4$ - 10 mol %, depending on T_c) and these catalysts have lower ethene selectivity and higher oxidation products than V:Mo of 0.12-0.60 ($Mo_1V_{0.12}$ - $Mo_1V_{0.60}$), which have moderate conversion ($Conv._{C2H6} = 16$ - 25 mol %, depending on T_c) of ethane, with high ethene selectivity and low oxidation products. However, these poorly active catalysts give more partial combustion products and proportionally higher CO_x than those with a lower vanadium concentration on the surface.

The products obtained by ethane ODH are mainly ethene, carbon monoxide, carbon dioxide and AA. Experiments were carried out at different reaction conditions while maintaining the same GHSV. When examining the activity of the catalysts with varying vanadium content that were calcined at 350 °C, important observations were noted. Very low vanadium ($Mo_1V_{0.12}$) and very high vanadium contents (Mo_1V_1) are poorly active ($Conv._{C2H6} = 3$, 6 mol %) catalysts, while the ethane conversion varies and strongly depends on temperature, e.g. - the ethane conversion is almost doubled on increasing reaction temperature by only 20 ºC. The selectivity to carbon oxide when compared with the total selectivity ($S_{EE} + S_{AA}$) is also higher for these catalysts. However, catalysts with moderate vanadium ratios are more active and have less selectivity to carbon oxide.

The catalyst $Mo_1V_{0.40}$ shows optimum activity with the highest yield to ethene. This catalyst was further studied to optimize the ethane concentration in feed while keeping

oxygen concentration constant in all ratios as shown in Table 3.4. The ethane conversion is lower when the ethane concentration (50 mol %) is greater and conversion increases when the ethane concentration in the feed is decreased, while oxygen behavior is reverse except in higher ethane concentration feed. Due to a constant concentration of oxygen, its conversion decreases with decreasing ethane concentration in the feed. The feed ratio ethane and oxygen (40:10) shows maximum conversion of both reactants over the selected catalyst (Table 3.5 and 3.6).

Reaction temperature and pressure both impact upon the catalytic activity. Three temperatures at different pressures from atmospheric to 200 psig have been studied using the $Mo_1V_{0.4}$ catalyst. Increasing the temperature or pressure results in a higher conversion of ethane as shown in Tables 3.7 to 3.11. Higher temperature increases the ethane conversion and results in an increase of COx at the expense of ethene, whilst the selectivity of AA has not changed significantly. Pressure also increases ethane consumption during the reaction over the selected catalyst but with a lower degree of impact. Pressure has a direct impact on AA formation at the expense of ethene while carbon oxide formation remains stable. The activity of the selectedcatalyst can be maximized at mild temperature and pressure to obtain maximum yield of ethene during the ethane ODH.

Experimental data indicate that the most promising results occur at a temperature of 290 ℃ for 70 psig pressure. This temperature and pressure results in the lowest amount of carbon oxide formation and greater activity in terms of ethane conversion and ethene selectivity. However, at a higher temperature of 310 ℃, the conversion increases, which is associated with an increase in carbon oxide formation due to a high consumption of oxygen as the temperature increases. There is also a significant impact on the AA selectivity which increases with temperature and pressure in the reaction process.

3.7 References

[1] O. Desponds, R. L. Keiski, G. A. Somorjai, *Catal. Lett.* **19** (1993) 17.

[2] E. M. Thorsteinson, T. P. Wilson, F. G. Young, P. H. Kasai, *J. Catal.* **52** (1978) 116.

[3] P. Botella, A. Dejoz, J. M. Lopez Nieto, P. Concepcion, M. I. Vazquez, *Appl. Catal. A* **98** (2006) 16.

[4] P. Concepcion, P. Botella, A. Dejoz, J. M. Lopez Nieto, *Appl. Catal. A* **278** (2004) 45.

[5] K. Ruth, R. Burk, R. Keiffer, *J. Catal.* **175** (1998) 27.

[6] P. Botella, J. M. Lopez Nieto, B. Solsona, A. Mifsud, F. Marquez, *J. Catal*. **209** (2002) 445.

[7] Y. Liu, P. Cong, R.D. Doolen, Sh. Guan, V. Markov, L. Woo, S. Zeyss, U. Dingerdissen, *Appl. Catal. A: Gen*. **254** (2003) 59.

[8] D. Linke, D. Wolf, M. Baerns, O. Timpe, R. Schlogl, S. Zeyb, U. Dingerdissen, *J. Catal*. **16** (2002) 16.

[9] J. M. Oliver, J. M. Lopez Nieto, P. Botella, A. Mifsud, *Appl. Catal. A* **257** (2004) 67.

[10] L. Dambies, C. Guimon, S. Yiacoumi, E. Guibal, *Colloid Surf. A*. **177** (2001) 203.

[11] D. Kim, S. V. Kagwade, C. R. Clayton, *Surf. Interf. Anal.* **26** (1998) 155.

[12] *http://www.lasurface.com/*.

[13] *http://www.srdata.nist.gov*.

[14] J. P. Nogier, M. Delamar, *Catal. Today* **123** (1990) 417.

[15] G. Mestl, Ch. Linsmeier, R. Gottschall, R. Dieterle, J. Find, D. Herein, J. Jager, Y. Uchida, R. Schlogl, *J. Mol. Catal. A: Chem*. **162** (2000) 463.

[16] M. Mezourki, B. Taouk, L. Tessier, E. Bordes, P. Courtine, *Stud. Surf. Sci. Catal*. **75** (1993) 753.

[17] R. Burch, R. Swarnkar, *Appl. Catal*. **70** (1991) 129.

[18] A. Dinse, S. Khennache, B. Frank, Ch. Hess, R. Herbert, S. Wrabetz, R. Schloegl, R. Schomacker, *J. Mol. Catal. A: Chem*. **307**, 1-2 (2009) 43.

[19] S. T. Oyama, G. A. Somorjai, *J. Phys. Chem*. **94** (1990) 5022.

[20] J. H. Lunsford, E. Morales, *J. Catal.* **118** (1989) 255.

[21] X. Gao, J. M. Jeng, I. E. Wachs, *J. Catal.* **118** (2002) 209.

[22] L. Dupont, D. larcher, M. Touboul, *J. Solid State Chem*. **143** (1999) 41.

[23] Y. Hu, P. K. Davies, *J. Solid State Chem*. **119** (1995) 176.

[24] E. Bordes, P. Courtine, *Appl. Catal. A: Gen.* **157** (1997) 45.

[25] E. Bordes, P. Courtine, *Stud. Surf. Sci. Catal*. **110** (1997) 177.

[26] E. Bordes, *Top. Catal*. **15** (2001) 131.

[27] A. Dejoz, J. M. Lopez Nieto, F. Marquez, M. I. Vazquez, *Appl. Catal. A: Gen.* **250** (2003) 287.

[28] W. Ueda, K. Oshihara, *Appl. Catal. A* **200** (2000) 135.

[29] T. Ushikubo, K. Oshima, A. Kayou, M. Vaarkamp, M. Hatano, *J. Catal.* **169** (1997) 394.

[30] P. Botella, E. Garcia-Gonzalez, A. Dejoz, J. M. Lopez Nieto, M. I. Vazquez, J. Gonzalez-Calbet, *J. Catal.* **225** (2004) 428.

[31] T. Katou, D. Vitry, W. Ueda, *Catal. Today* **91-92** (2004) 237.

[32] D. Vitry, J. L. Dubois, W. Ueda, *J. Mol. Catal. A: Chem.* **220** (2004) 67.

[33] A. Corma, J. M. Lopez Nieto, N. Paredes, *J. Catal*. **144** (1993) 425.

[34] X. Gao, P. Ruiz, Q. Xin, X. Guo, B. Delmon, *J. Catal*. **148** (1994) 56.

[35] O. Baerns, V. Buyevskaya, A. Brueckner, R. Jentzsch, E. Kondratenko, M. Langpape, D. Wolf, *Stud. Surf. Sci. Catal*. **140** (2001) 55.

[36] G. Grubert, E. Kondratenko, S. Kolf, M. Baerns, P. Greem, R. Parton, *Catal. Today* **81** (2003) 337.

[37] J. Urschey, A. Kuehnle, W. F. Maier, *Appl. Catal. A: Gen*. **252** (2003) 91.

[38] A. Corma, J. M. Serra, E. Argente, V. Botti, S. Valero, *Chem. Phys. Chem*. **3** (2002) 939.

Chapter 4

Results of oxalic acid addition on MoV oxide catalyst activity for the oxidative dehydrogentation (ODH) of ethane

4.1 Introduction

MoV catalysts have been investigated extensively for their high selectivity to lower molecular weight alkenes, especially ethene [1-2]. The catalyst preparation is mostly performed by the hydrothermal method. However, it is difficult to control key properties such as crystal structure, particle shape, and surface area that determine the performance of the catalysts, hence reproducibility is difficult. The studies presented in this chapter focus mainly on the improvement of the preparation method and the characterization of the catalysts. Parameters such as pH, temperature, molybdate solution temperature, and rate of addition can be altered in order to produce the desired catalytic phase with high ethene selectivity. In the present study, the variables investigated include the final pH of the obtained precipitated slurry (achieved via the addition of different acids), the

temperature of precipitation, and the calcination temperature of precursor materials. Optimum preparation conditions have been achieved on the basis of the catalytic performance. The effects of reaction variables (reaction temperature and pressure) have also been studied in order to define the optimum reaction conditions for further studies. Particular effort was made to collect stable product data in the gas phase to ensure full mass balance.

The objective of this chapter is to determine the optimum mass of oxalic acid for addition at the precursor stage of catalyst preparation of molybdenum vanadium oxide catalysts ($Mo_1V_{0.4}$), and to identify the optimum preparation conditions with respect to catalytic activity.

For this study, seven catalysts (with 2.5:1 ratios of Mo and V) were prepared with different masses of oxalic acid in the preparation step to observe the role of oxalic acid for ethane ODH to ethene. The details of oxalic acid addition are given in Table 4.1. All catalysts were prepared by precipitating precursor solutions and drying the slurry at 120 ºC in an oven for 16 h as described in Chapter 2.

Table 4.1: Slurry pH with different amount of oxalic acid used in catalysts.

Catalyst Ref.	Oxalic acid (g)	Slurry pH
MoV-0	0.0	5.43 @ 81 ºC
MoV-1	1.0	4.76 @ 81 ºC
MoV-2.5	2.5	4.34 @ 81 ºC
MoV-5	5.0	3.71 @ 81 ºC
MoV-7.5	7.5	3.56 @ 80 ºC
MoV-10	10.0	3.21 @ 80 ºC
MoV-12.5	12.5	1.67 @ 81 ºC

4.2 Experimental results

All prepared catalysts were tested as discussed in Chapter 2. The experiments were carried out at 70 psig in a fixed bed tubular reactor at different temperatures (270 - 310 ºC). A stabilization period of 2 h was maintained for all catalysts tested to have steady state data collection. Reactants and products were analyzed by online GC. The catalytic performance data are presented in Tables 4.2 - 4.4.

4.2.1 Catalyst testing data at 270 ºC.

Table 4.2: ODH of ethane data on MoV oxide catalysts at 270 ºC.

Catalyst	Conv. (%)		Selectivity (%)				Yield (%)
Ref.	C_2H_6	O_2	CO_2	CO	C_2H_4	AA	C_2H_4
MoV-0	1.4	5.7	6.4	38.1	55.1	0.3	0.8
MoV-1	3.7	11.3	10.3	24.1	64.5	1.1	2.4
MoV-2.5	11.7	43.9	6.1	17.2	69.2	7.5	8.1
MoV-5	18.3	66.8	5.1	8.9	71.2	14.9	13.1
MoV-7.5	19.1	71.3	3.4	8.5	71.8	16.3	13.7
MoV-10	17.5	58.8	3.1	7.3	77.1	12.5	13.5
MoV-12.5	5.5	17.1	3.8	11.4	70.3	14.5	3.9

Reaction conditions: Pressure = 70 psig, temp. = 270 ºC, feed gas = ethane: oxygen: nitrogen (40:10:50), catalyst wt. = 1 g, feed flow = 25 ml/min.

Catalysts prepared with varying amounts of oxalic acid were calcined at 350 ºC in air, and tested at the same process conditions to compare their activity. Catalytic activity data shows that the catalyst prepared without oxalic acid has the lowest activity, compared with catalysts prepared with oxalic acid. Selectivity to ethene increases with increasing oxalic acid addition but carbon oxide selectivity decreases with the exception of the catalyst prepared with 12.5 g of oxalic acid. Maximum ethene selectivity is obtained with the catalyst prepared with 10 g oxalic acid. Acetic acid (AA) selectivity initially increases with oxalic acid addition, reaching a maximum upon the addition of 7.5 g of oxalic acid.

4.2.2 Catalyst testing data at 290 ºC.

Table 4.3: ODH of ethane data on MoV oxide catalysts at 290 ºC.

Catalyst	Conv. (%)		Selectivity (%)				Yield (%)
Ref.	C_2H_6	O_2	CO_2	CO	C_2H_4	AA	C_2H_4
MoV-0	2.7	9.4	8.5	48.0	43.1	0.4	1.2
MoV-1	5.9	18.4	12.4	31.7	54.5	1.5	3.2
MoV-2.5	18.5	60.6	8.1	19.1	61.6	11.2	11.4
MoV-5	23.1	91.5	6.4	10.2	65.2	18.2	15.1
MoV-7.5	24.2	90.9	5.9	9.3	64.4	20.3	15.6
MoV-10	21.8	88.1	4.6	8.7	69.2	17.5	15.1
MoV-12.5	8.3	29.1	6.1	12.4	63.0	18.6	5.2

Reaction conditions: Pressure = 70 psig, temp. = 290 ºC, feed gas = ethane: oxygen: nitrogen (40:10:50), catalyst wt. = 1 g, feed flow = 25 ml/min.

4.2.3 Catalyst testing data at 310 ºC.

Table 4.4: ODH of ethane data on MoV oxide catalysts at 310 ºC.

Catalyst	Conv. (%)		Selectivity (%)				Yield (%)
Ref.	C_2H_6	O_2	CO_2	CO	C_2H_4	AA	C_2H_4
MoV-0	3.6	16.4	9.5	50.7	39.3	0.6	1.4
MoV-1	7.4	31.9	14.7	34.4	49.0	1.8	3.6
MoV-2.5	25.0	93.8	10.3	21.6	55.0	13.1	13.8
MoV-5	27.6	99.8	6.8	11.7	62.2	19.3	17.2
MoV-7.5	27.8	100	5.9	10.6	63.1	20.5	17.6
MoV-10	26.6	96.6	6.1	10.2	67.7	16.1	18.0
MoV-12.5	12.9	52.7	7.0	15.8	59.5	17.7	7.7

Reaction conditions: Pressure = 70 psig, temp. = 310 ºC, feed gas = ethane: oxygen: nitrogen (40:10:50), catalyst wt. = 1 g, feed flow = 25 ml/min.

Although the catalytic activity increases for all catalysts as temperature increases from 270 ºC to 310 ºC, the product selectivity remains almost constant. Catalysts prepared with little or no oxalic acid have low ethane conversion as well as low selectivity towards

ethene formation. However catalyst prepared by adding more oxalic acid (2.5 - 10 g) showed increased ethane conversion as well as increased ethene selectivity.

At the highest temperature, the catalytic activity increased to a maximum as oxygen is almost fully consumed. At this temperature carbon oxide and acetic acid (AA) formation increase while ethene selectivity decreases, though the activity behavior remains the same for all catalysts.

4.3 Results and discussion

Catalytic activity data showed very clearly a modification in the catalytic property or the active center of the catalysts upon addition of oxalic acid. The main products obtained by ODH of ethane are ethene, carbon monoxide, carbon dioxide and AA. Experimental data shows that oxygen conversion increases with temperature and reached 100% with the MoV-7.5 at 310 °C. The catalyst prepared without oxalic acid has very poor activity at all three tested temperatures. Selectivity to ethene and carbon oxide is 40 and 60 mol % respectively, with a very small (∼1 mol %) formation of AA (Fig.4.2).
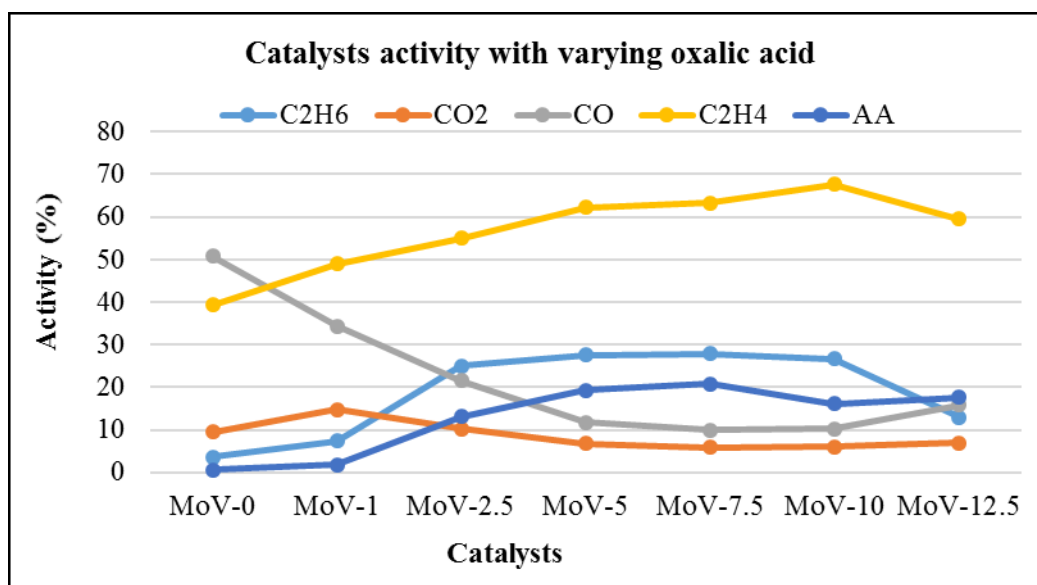
Fig.4.1: Catalytic activity trends of catalysts varying with oxalic acid at 310 ºC.
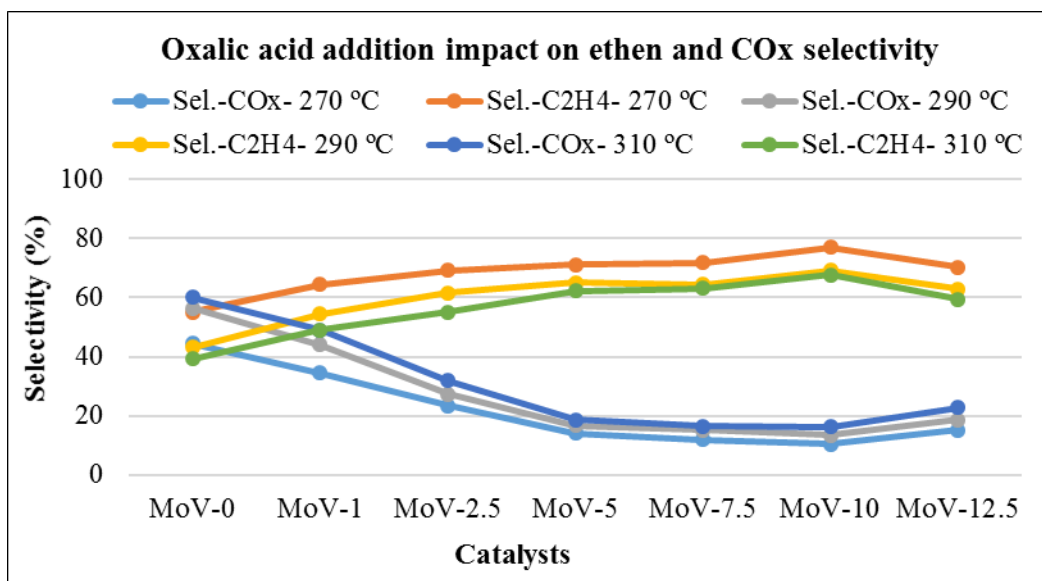
Fig.4.2: Selectivity to ethene (C_2H_4) and carbon oxide (CO_x) vs. reaction temperature for all catalysts.

Examining the catalytic activity behavior at different reaction temperatures (between 270 and 310 °C), two trends were observed (except for the case of MoV-0): activity first increases with increasing mass of oxalic acid and then begins to decrease with an excess addition of oxalic acid, whereas the conversion varies strongly with increasing reaction temperature. This trend is the same for all temperatures. Catalytic activity data are given in Tables 4.2 - 4.4. The formation of carbon monoxide compared to that of carbon dioxide is also quite informative. The $S_{CO}/S_{CO}+S_{CO2}$ amounts to 0.8-0.7 for the catalysts prepared with lower amounts of oxalic acid and the catalysts are less active, whereas $S_{CO}/S_{CO}+S_{CO2}$ remains constant at 0.6 for all the catalysts prepared with more than 5 g oxalic acid and the activity is high.

It has been reported that addition of oxalic acid during catalyst preparation by slurry or hydrothermal methods strongly influences both the nature of the phases and their catalytic activity [1-2]. The variation in amount of oxalic acid results in significant changes in the phase composition and catalytic characteristics [2] due to the fact that the

oxidation states of elements and the nature of crystalline phases in the catalyst depend on the oxalic acid content.

These findings matched those of Popova et al. [3] over MoVNbTe oxide catalysts for propane ammoxidation which showed that catalysts prepared without the addition of oxalic acid have low activity which increases with the addition of oxalic acid, added with niobium in the preparation slurry. The addition of oxalic acid resulted in increased activity and ethene selectivity with decreased carbon oxide formation, whilst AA formation also increases slowly. Selectivity to ethene decreases with increasing temperature, while the carbon oxide selectivity increases (Fig.4.2). This indicates that the reaction performance is highly temperature dependent.

Thorsteinson [4] studied catalysts consisting of a mixture of the oxides of molybdenum and vanadium as well as the with the addition of third metals for ODH of ethane at various process conditions. Kinetics of the process were performed and it was found that under super-atmospheric pressures AA becomes a coproduct of the reaction. The rate equation for AA production shows a first order dependence which means that it is independent of partial pressure of ethane and dependent on ethene and oxygen pressures. Similarly, the expression for the production of CO_x is independent of the ethane partial pressure. This suggests that the primary product of ethane ODH is ethene and that acetic acid and carbon oxide are formed by its subsequent oxidation.

Further to this, a significant change in the product selectivity is also observed with the catalysts prepared with oxalic acid. There is a decrease in the total oxidation products such as carbon monoxide and carbon dioxide, while the product selectivity to ethene and AA increases and is constant until an excess amount of oxalic acid is used.

4.4 Results of catalyst characterization

MoV catalysts with oxalic acid showed that the oxidation states of V and Mo are changed to an optimum redox level, which enhances the ODH function of the MoV and decreases the number of active sites responsible for the total oxidation; this can be verified by Raman spectroscopy, XRD, XPS and TEM analysis of the material.

4.4.1 BET

The catalyst prepared without oxalic acid has a surface area of 12 m^2/g. The surface area increases with the addition of oxalic acid. Catalysts prepared with zero/low or higher than 10 g of oxalic acid have a surface area of 12 - 14 m^2/g and have low catalytic activity; whilst the catalysts prepared with 2.5 - 10 g of oxalic acid have a high surface area 18 - 23 m^2/g and show good catalytic activity. The surface area of the catalysts prepared by varying oxalic amount is given in Table 4.5.

Table 4.5: Surface area of catalysts prepared with different amounts of oxalic acid.

Cat. Ref.	Oxalic acid (g)	Surface area (m^2/g)
MoV-0	0	12
MoV-1	1	13
MoV-2.5	2.5	18
MoV-5	5	23
MoV-7.5	7.5	20
MoV-10	10	21
MoV-12.5	12.5	14

4.4.2 Raman spectroscopy

To analyze the nature of the surface species of bulk MoO_3, and V_2O_5 samples were calcined at 350 °C prior Raman spectroscopy. Fig. 4.3 shows Raman spectra of bulk

MoO$_3$ and bulk V$_2$O$_5$, obtained by calcining ammonium molybdate and ammonium metavandate precursor. The major vibrational modes of MoO$_3$ are located at 995, 819, 667 and 290 cm^{-1} and have been assigned to the Mo=O stretching mode, the Mo-O-Mo asymmetric stretching mode, the Mo-O-Mo symmetric stretching mode, and M=O bending mode, respectively. The Raman spectra for the bulk V$_2$O$_5$ displayed bands of 406, 528, 702, and 996 cm^{-1}, all of which are characteristic of crystalline V$_2$O$_5$. The 996 cm^{-1} band is assigned to the vibration of the short vanadium and oxygen bond normally regarded as a V=O species.
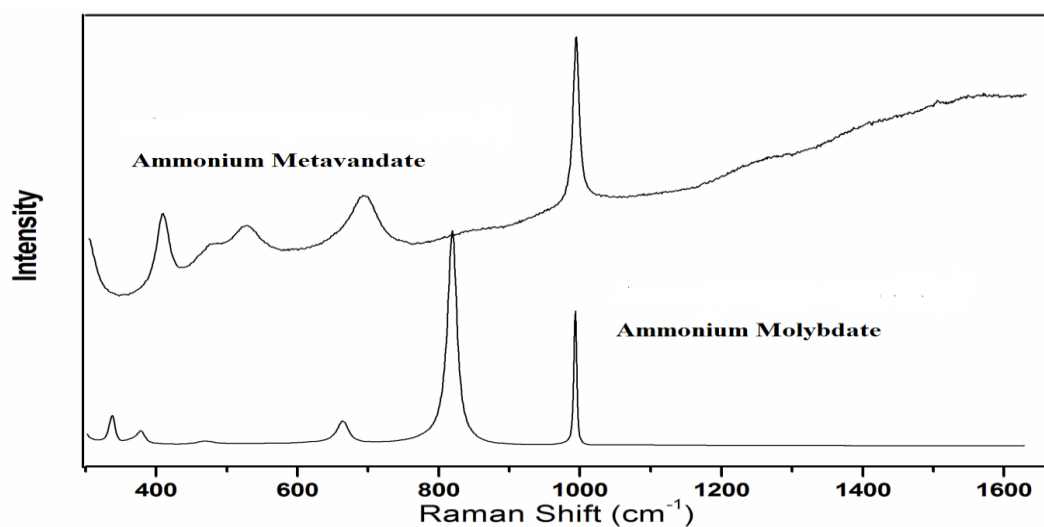
Fig.4.3: Raman analysis result for bulk salts of molybdenum (ammonium molybdate) and vanadium (ammonium metavandate) after calcination at 350 °C.

Fig. 4.4 shows Raman spectra of MoV oxide catalysts prepared by addition of different amounts of oxalic acid. The first two samples prepared with 0 g and 1 g of oxalic acid showing main bands at 996, 820, and 406 cm^{-1} have poor activity, while other catalysts showing broad and low intensity bands in these positions have greater catalytic activity.
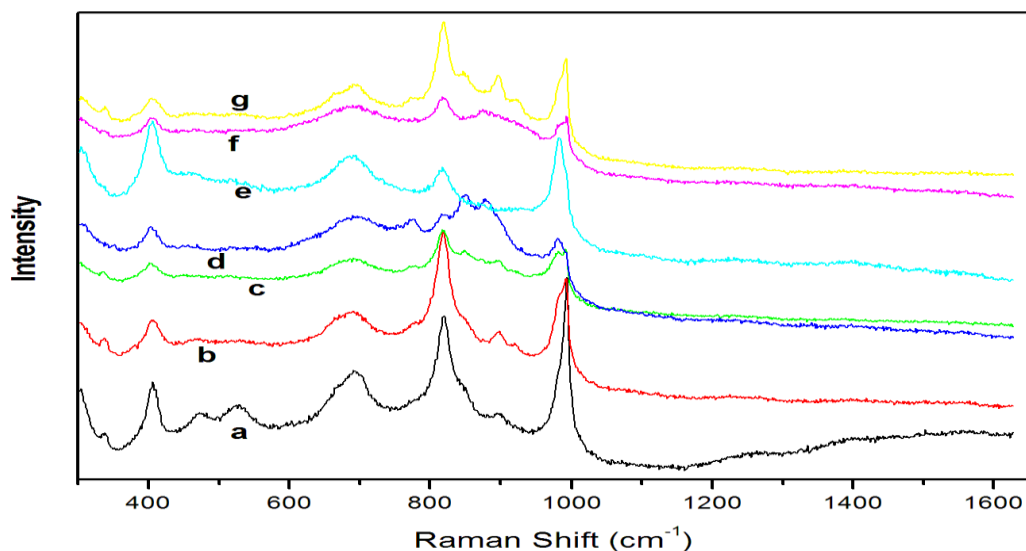
Fig.4.4: Raman spectra of catalysts prepared by varying oxalic acid amount; MoV-0-(a), MoV-1-(b), MoV-2.5-(c), MoV-5-(d), MoV-7.5-(e), MoV-10-(f), MoV-12.5-(g).

The Raman spectra of all MoV oxides catalysts are characterized by an intense peak in the range 950-820 cm^{-1}, a wide medium peak centered ca. 700 cm^{-1} and a small sharp peak at 407 cm^{-1}. Slight differences seem to be related to the addition of different amounts of oxalic acid in the catalyst preparation. In MoV oxide, some lines assigned to MoO$_3$ (particularly the vibration of Mo-O-Mo and Mo=O bonds at 820 and 995 cm^{-1}, respectively) are more intense as seen in Fig.4.4. Lines observed at 995, 820, 700 and 405 cm^{-1} are slightly shifted and contain more peaks with the addition of more oxalic acid. Raman lines at 860-940 cm^{-1} are assigned to the M-O-M stretching mode of polycrystalline M-M-O mixed metal oxide while those ca. 1000 cm^{-1} are assigned to the M=O (or M′=O) stretching mode. In particular, lines at 932 and 873 cm^{-1} are related to M-O-V phases. Mestl [5], in their study of an Mo-V-O system doped with tungsten, assigned lines at 940-860 cm^{-1} and a broad peak at ca. 700 cm^{-1} to a nanocrystalline Mo$_5$O$_{14}$-type mixed oxide with partial substitution of Mo by V and/or W. Niobium and tungsten also affects the crystallinity of Mo mixed oxide [6]. Therefore the present samples do have the same phase and do contain (VMo)$_5$O$_{14}$. However, hexagonal mixed

oxides also present as shown by their main line located in the same range, in accordance with the XRD patterns. However, a noticeable difference exists between the catalyst without oxalic acid and those with oxalic acid; the characteristic lines of nanocrystalline Mo_5O_{14} types disappeared or their intensity considerably decreases with oxalic acid. However, the latter modification occurs simultaneously with a relatively strong increase of the intensity of hexagonal molybdenum oxide [h-MoO_3] type's lines.

Raman spectral adsorption bands of MoO_3 at 810, 662 and 340 cm^{-1} were observed for the materials prepared without oxalic acid. These are shifted or disappear (in d, e, f spectra in Fig. 4.4) with the addition of oxalic acid, especially the intense band at 810 cm^{-1}. The addition of oxalic acid led to an anisotropic deformation of vanadium oxide parallel to the (010) plane and a chaotic degradation of molybdenum oxide. In this case, the supporting of vanadium oxide on molybdenum and surface coverage of the latter with V_2O_5 took place; this is reflected in a decrease of the adsorption band at 810 cm^{-1}.

4.4.3 XRD

XRD patterns of the bulk salts of ammonium molybdate and ammonium metavandate without any treatment showed crystalline structures. When these salts were calcined at 350 ºC for 4 h, the XRD showed a more crystalline structure as given in Fig. 4.5. XRD patterns of bulk salts of ammonium molybdate and ammonium metavandate calcined at 350 °C (Fig. 4.5) correspond to several Mo phases containing ammonium, including ammonium heptamolybdate tetra-hydrate (JCPDS 70-1707), $(NH_4)_2Mo_4O_{13}$ (JCPDS 80-0757) and an intense line at 8.3 ° which is isostructural to hexagonal molybdenum oxide h-MoO_3, the structure of which is known to be stabilized by ammonium ions and/or protons [7-8].
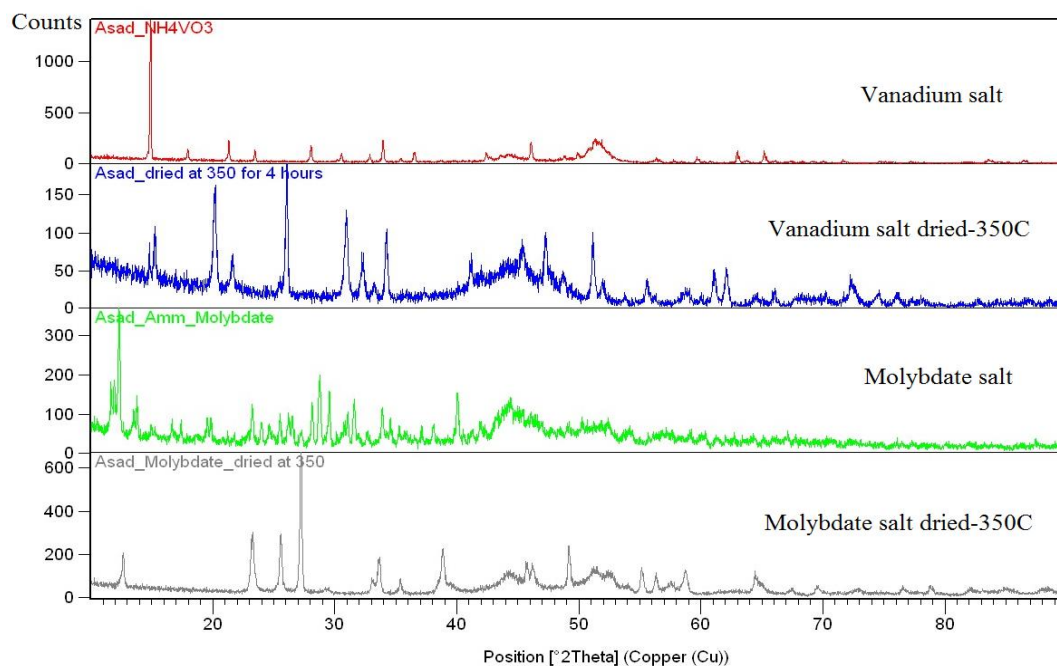
Fig.4.5: XRD patterns of vanadium and molybdenum salt (normal and dried at 350 ºC).

The catalysts prepared with addition of oxalic acid showed a significant change in their morphology where the structure changes from crystalline to amorphous. The catalysts prepared with little or no oxalic acid showed crystalline structure. The same behavior is seen with MoV-12.5 which clearly shows a crystalline structure as shown in Fig. 4.6. However, the catalysts prepared by the addition of 5 - 10 g of oxalic acid show amorphous structure and have higher activity than the catalysts with crystalline structures. The catalysts with amorphous character (Fig. 4.6) centered at $2\theta = 22.2$ ° and the broad line at 25.5 ° (corresponding to several lines) may be assigned to NH_4VO_3, but also to Mo_5O_{14} (called θ-phase) stabilized by vanadium [9], respectively. The other patterns also exhibit a partly amorphous character with a small number of sharp lines belonging to ammonium vanadium oxides $(NH_4)V_yO_z$ (including NH_4VO_3) and V_2O_5.

A feature common to all MoV oxide catalysts is the presence of reflections at $d(Å)/2\theta=4.0/22.2$ ° and $d(Å)/2\theta= 3.46/25.7$ °. In addition to h-MoO₃, several phases have

been identified in these samples. The fact that most of h-MoO_3 is shifted compared to the standard patterns (JCPDS 21-0569) may be due to a modification by vanadium or to the formation of oxygen vacancies, as in MoO_{3-x}. The presence of Mo_5O_{14}-type structure is ascertained by the strong reflections at $d(\text{Å})/2\theta = 4.02/22.2\,°$ and $3.56/25.54\,°$.
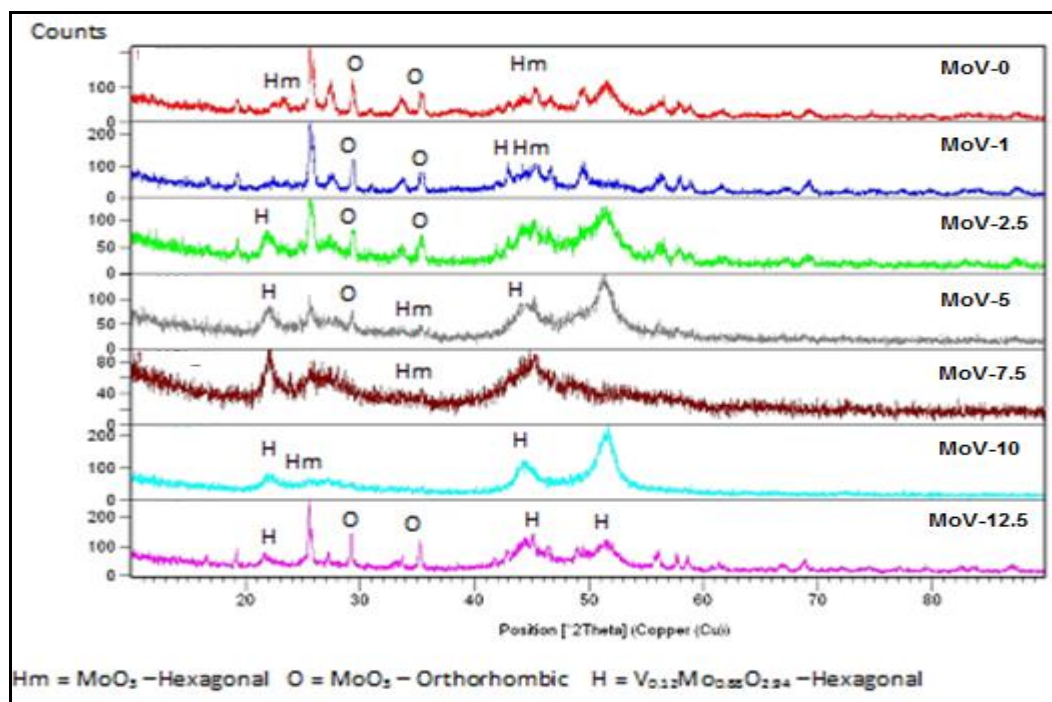
Fig.4.6: XRD patterns of catalysts prepared by varying oxalic acid amount.

The phases and crystallinity of the synthesized materials as seen in Fig. 4.6 depict sharp diffraction reflections for MoV-0 and MoV-12.5 and the peaks are well matched with a standard data card (JCPDS 21-0569; a=10.53 Å and c=14.9 Å) and indexed as hexagonal phase MoO_3. The intense peak at 27.8 $°$ is associated with the (210) plane of h-MoO_3 as bulk molybdate oxide (Fig.4.5) shifted towards a higher diffraction angle (2θ) in MoV oxide materials, revealing the changes in the inter-planar distance (d_{210}). The d_{210} value of synthesized material is 3.43 Å, which is lower than pure bulk molybdate oxide (3.46 Å). The reflection intensities of the MoO_3 decrease to a lesser extent with the addition of oxalic acid.

112

4.4.4 XPS

Binding energies (BE) were referenced to O *1s* core (530.40 eV). The area of Mo and V $(3d_{3/2}, 3d_{5/2})$, $(2p_{3/2})$ peaks was measured for each sample and the surface stoichiometry determined. Signals were deconvoluted in order to obtain the relative amount of oxidized and reduced cations. The extreme values were obtained from bulk stoichiometry by considering the cations in their oxidized or reduced forms, respectively given in Table 4.7.

MoV-0
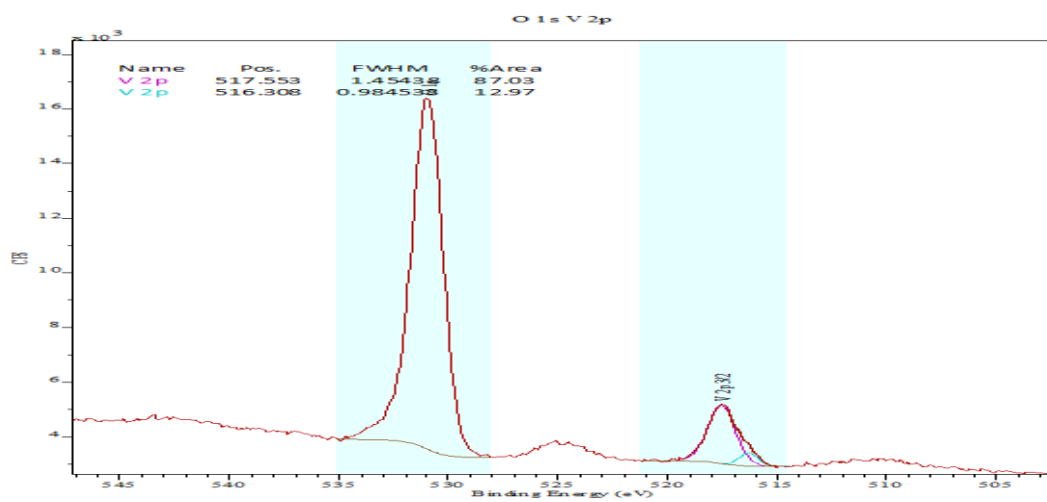
MoV-1
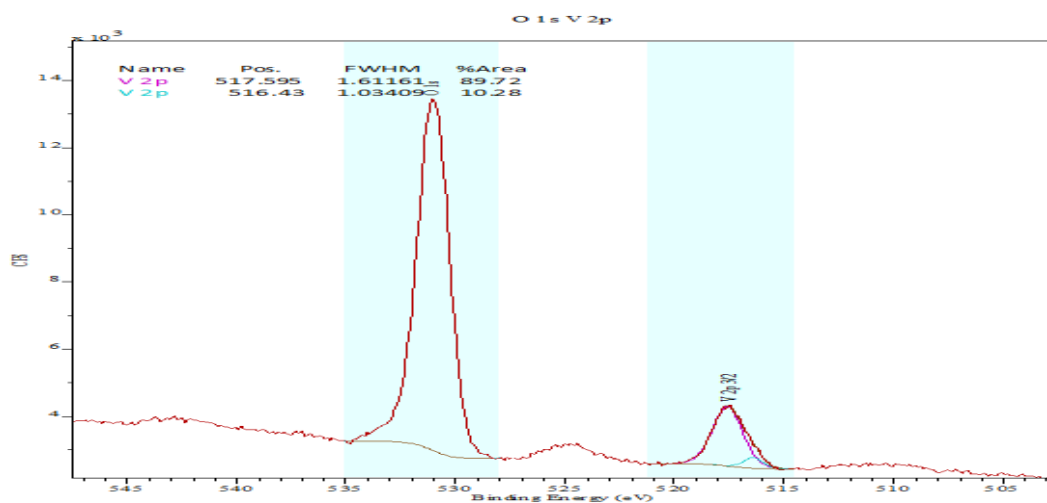
MoV-2.5
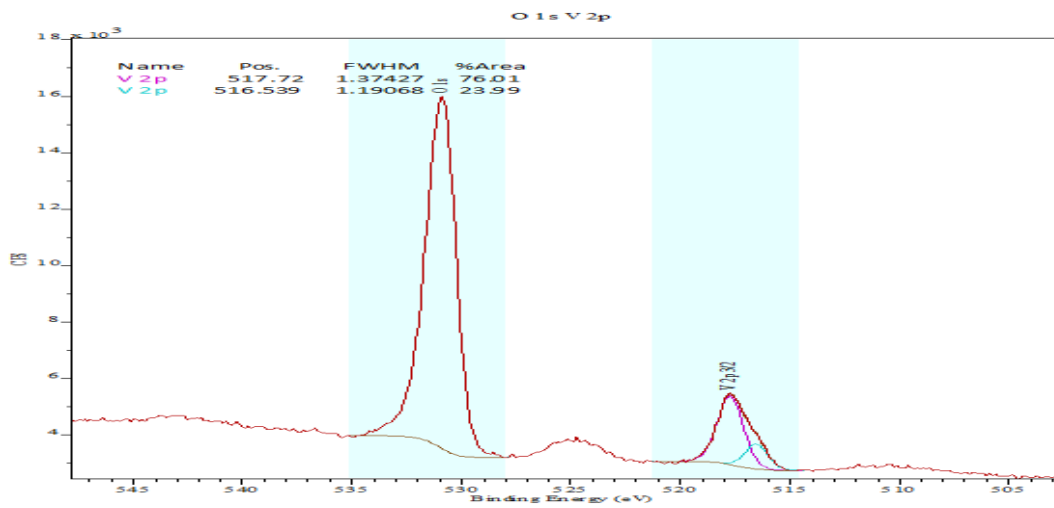
MoV-5.0
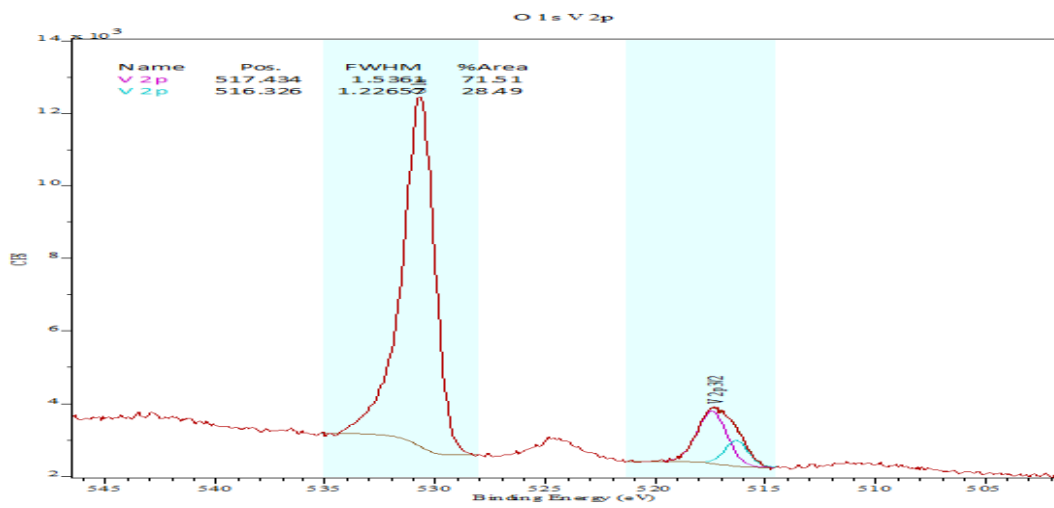
MoV-7.5
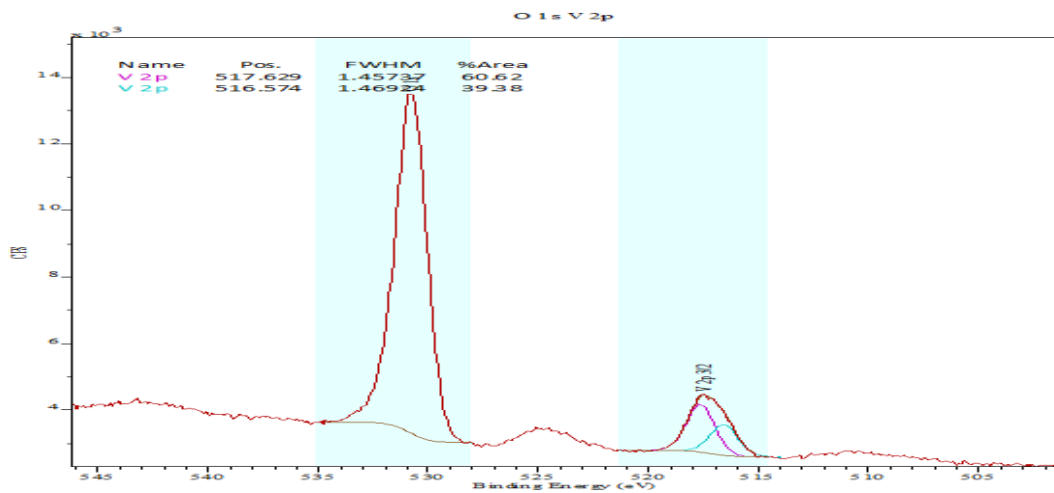
MoV-10
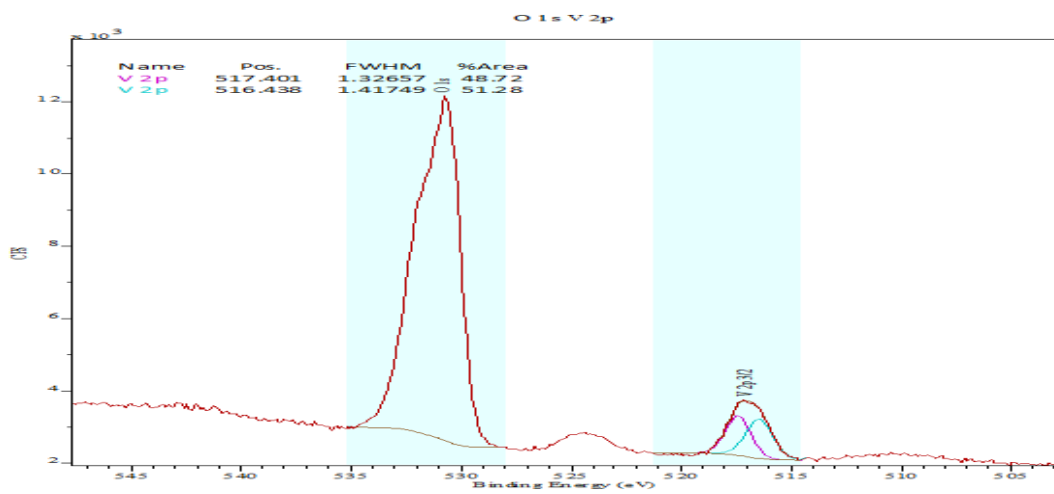
MoV-12.5
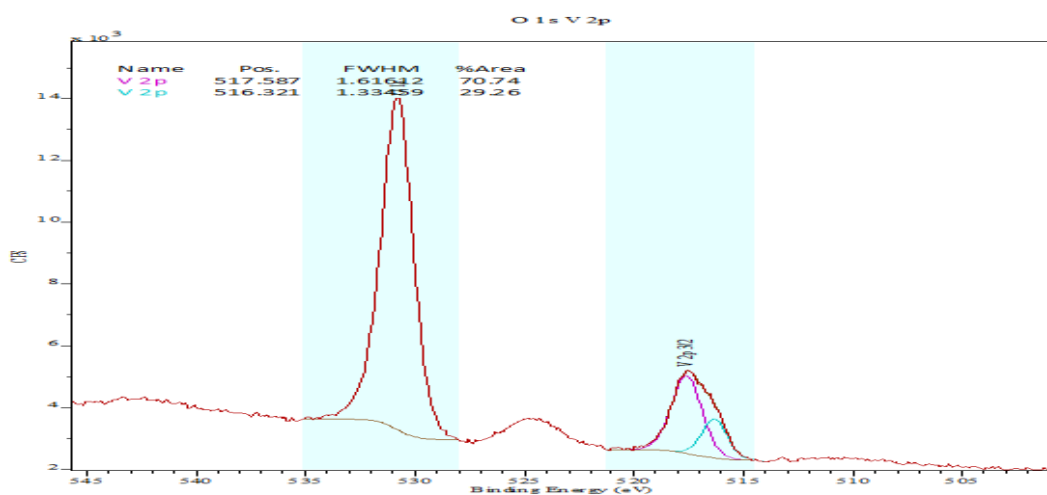
Fig.4.7: X-ray photoelectron spectra of catalysts showing 'V' binding energies prepared by varying oxalic acid amount.

The surface coverage of vanadium oxide was investigated by XPS as shown in Fig. 4.7. In these catalyst samples, Mo photopeaks, characteristic of Mo^{6+}, are determined by the BE as well as full width half maximum (FWHM) values. The standard values of these cations, as detailed in literature, are 232.4 ± 0.2 eV for Mo^{6+}, $230.8 - 231.8$ eV for Mo^{5+}, 516.6 ± 0.1 eV for V^{5+}, and 515.9 ± 0.4 eV for V^{4+} oxides [10-14]. These match with those of the samples, as shown in Table 4.6.

115

Table 4.6: XPS results of V concentrations in the MoV catalysts varying with oxalic acid amount.

Cat. Ref.	V	BE (eV)	FWHM (eV)	Area (%)
MoV-0	$V2p_{3/2}$ (V^{5+})	517.6	1.45438	87.03
	$V2p_{3/2}$ (V^{4+})	516.3	0.98454	12.97
MoV-1	$V2p_{3/2}$ (V^{5+})	517.6	1.61161	89.72
	$V2p_{3/2}$ (V^{4+})	516.4	1.03409	10.28
MoV-2.5	$V2p_{3/2}$ (V^{5+})	517.7	1.37427	76.01
	$V2p_{3/2}$ (V^{4+})	516.5	1.19068	23.99
MoV-5	$V2p_{3/2}$ (V^{5+})	517.4	1.5361	71.51
	$V2p_{3/2}$ (V^{4+})	516.3	1.22657	28.49
MoV-7.5	$V2p_{3/2}$ (V^{5+})	517.6	1.4573	60.52
	$V2p_{3/2}$ (V^{4+})	516.6	1.46924	38.38
MoV-10	$V2p_{3/2}$ (V^{5+})	517.4	1.32657	48.72
	$V2p_{3/2}$ (V^{4+})	516.4	1.41749	51.28
MoV-12.5	$V2p_{3/2}$ (V^{5+})	517.6	1.61612	70.74
	$V2p_{3/2}$ (V^{4+})	516.3	1.33459	29.26

The calculated values of oxidation state of vanadium can be explained with the equation proposed by Coulston [15] for individual vanadium oxides. In the presence of certain types of atoms (V and Mo in the present case), the capability of the oxygen atom to withdraw electron density from them should be taken into account and the so-called group shift [16-17] should be determined by the summation of Madelung energies over all types of atoms. The amount of oxygen, determined from the surface composition, is lower than when calculated from the bulk stoichiometry (where all V is assumed to be V^{4+}).

The XPS data in Table 4.7 shows that the V/Mo ratio remains the same in catalysts prepared with the addition of oxalic acid from 1 - 10 g, while the reducibility of vanadium is enhanced. This ratio decreases with the addition of oxalic acid, as the

reducibility has increased. The O/V value changes with increasing addition of oxalic acid, and shows different oxygen stoichiometry, while the O/Mo ratios do not change greatly. The relative amount of V^{4+} is smaller in the cases of MoV-0 and MoV-1, meaning the vanadium is less reducible when there is little or no oxalic acid used. XPS data clearly shows that the reducibility of vanadium is highly dependent on the presence of oxalic acid.

Table 4.7: Atomic ratios and stoichiometry of MoV catalyst varying with oxalic acid.

Catalysts	Binding energies (eV)			Atomic ratio			
Ref.	Mo^{6+}	V^{5+}	V^{4+}	V:Mo	O:V	O:Mo	$V^{5+}:V_{total}$
MoV-0	233.1	517.6	516.3	0.22	11.34	3.29	0.87
MoV-1	233.2	517.6	516.4	0.24	11.39	3.51	0.90
MoV-2.5	233.1	517.7	516.5	0.28	9.51	3.65	0.76
MoV-5	232.9	517.4	516.3	0.26	10.55	3.63	0.72
MoV-7.5	233.0	517.6	516.6	0.25	9.58	3.18	0.61
MoV-10	232.7	517.4	516.4	0.26	9.87	3.43	0.51
MoV-12.5	233.1	517.6	516.3	0.36	7.35	4.06	0.71

4.4.5 TEM

The Transmission electron microscopy (TEM) utilizes energised electrons to provide morphological, compositional and crystallographic information on samples. TEM images were obtained for the samples in order to study the oxalic acid impact on the catalysts morphologic and crystallographic properties. MoV-0 shows agglomerations of needle like particles or "nano-rods" of non-uniform length and width interconnected with an amorphous top layer, indicated by the arrow in the images. The catalyst also shows a significant amount of small <20 nm particles inter-dispersed within the needles, shown in Fig.4.8. MoV-1 has the same morphology but fewer small particles compared to the samples prepared without the addition of oxalic acid.

MoV-0
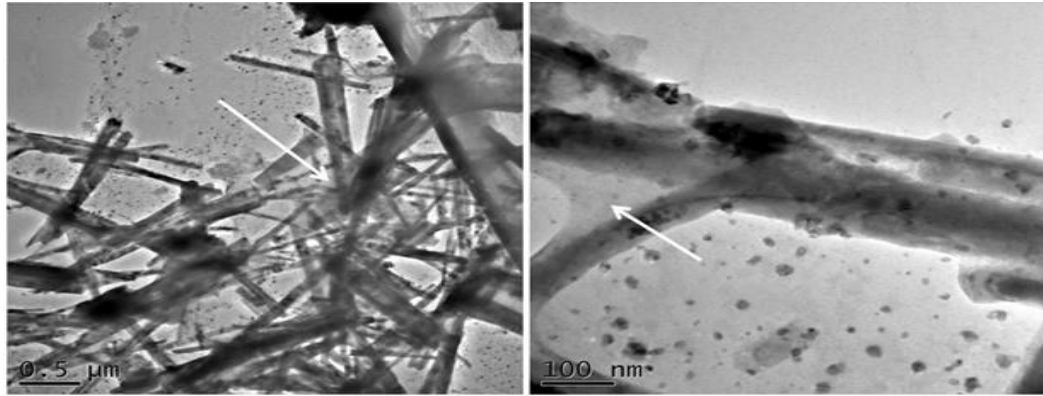
MoV-1
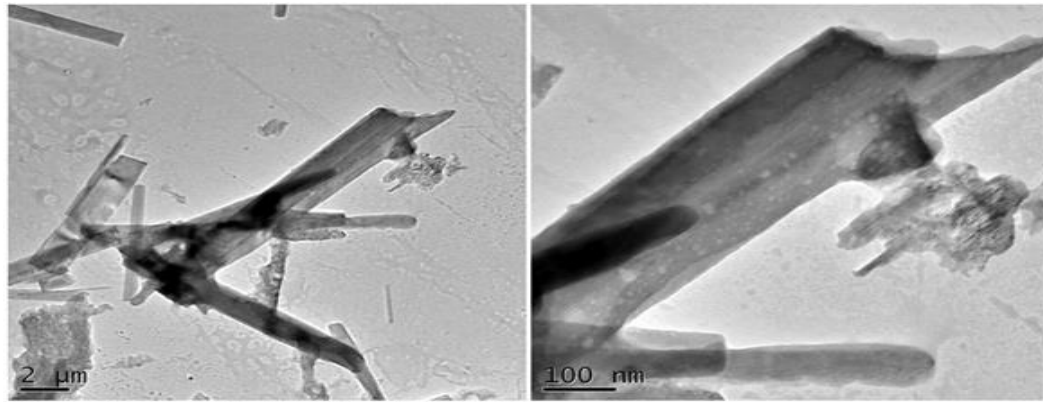
MoV-2.5
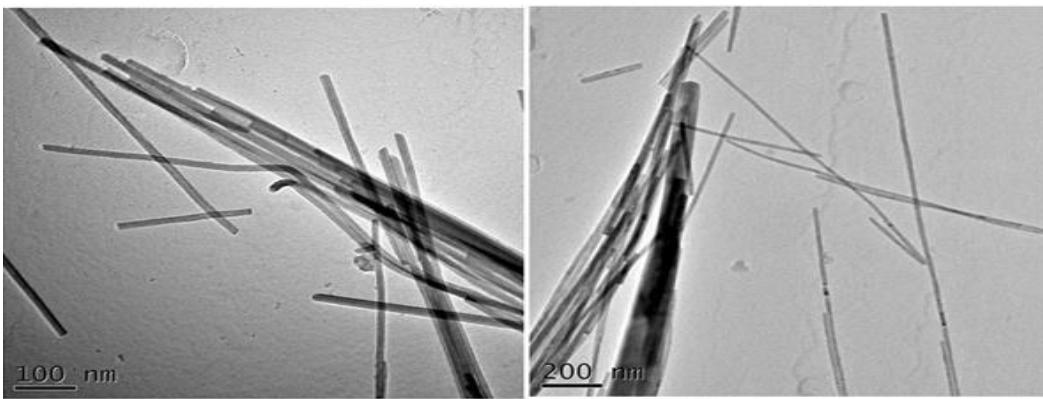
MoV-5
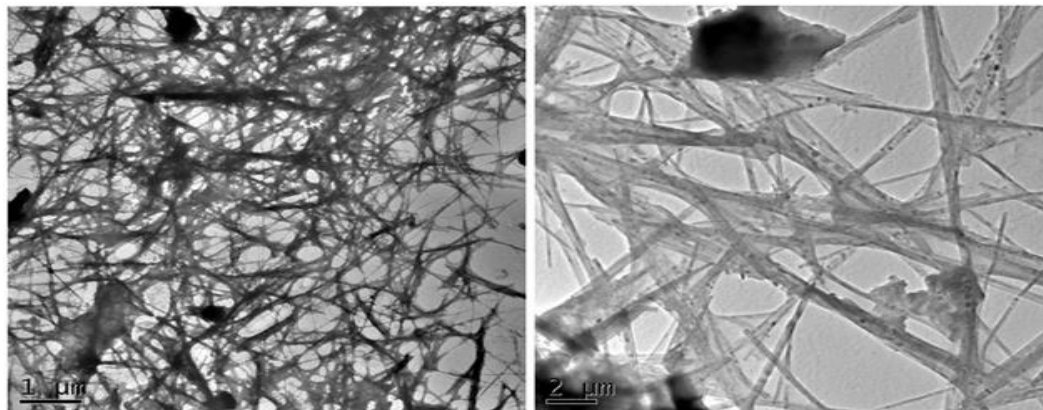
MoV-7.5
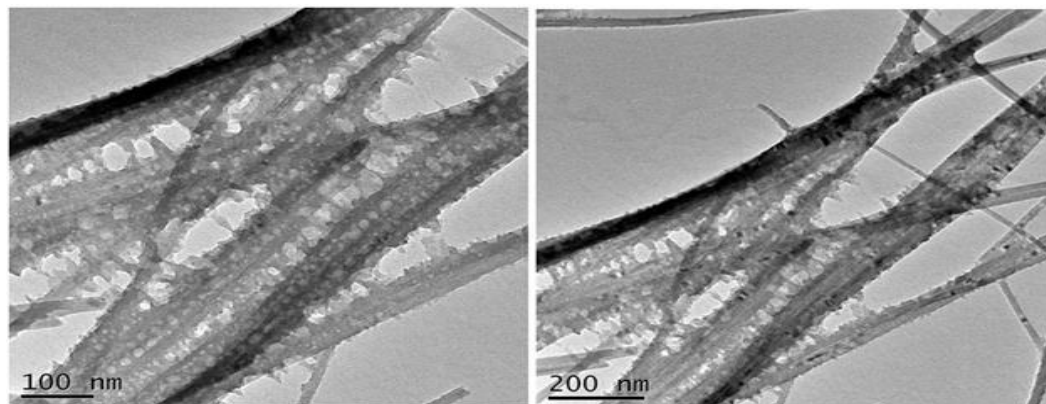
MoV-10
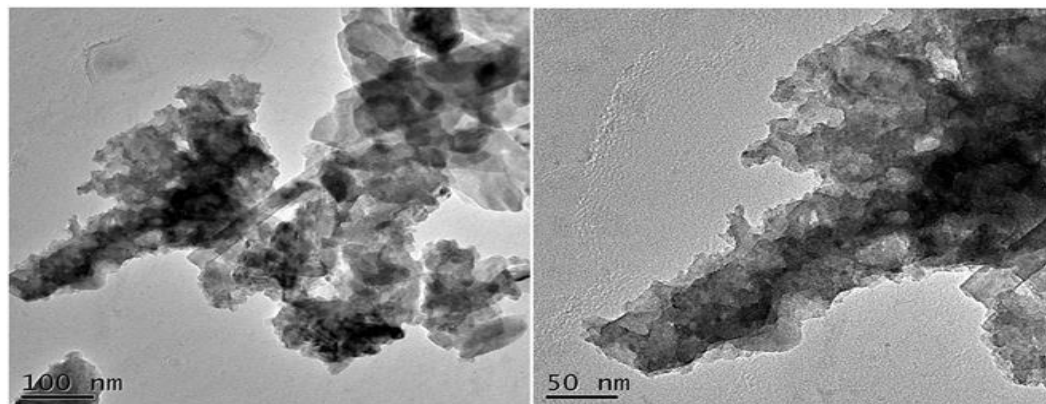
MoV-12.5
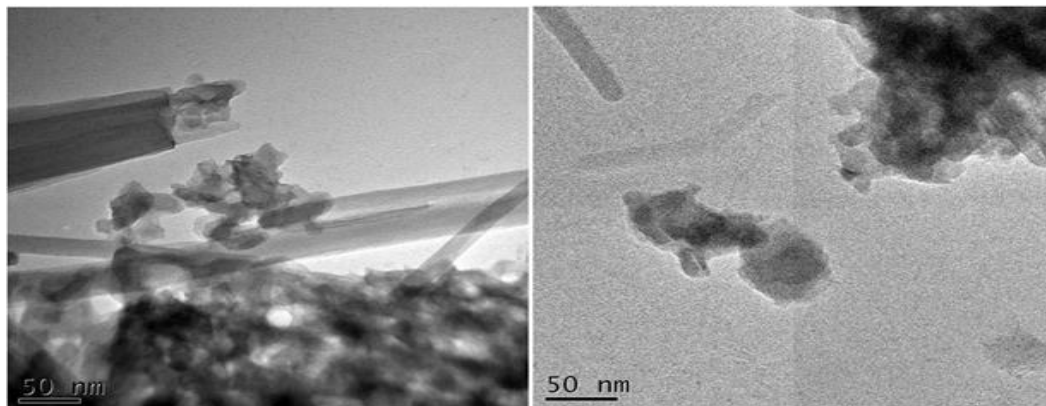
Fig.4.8: TEM images of catalysts prepared with different amount of oxalic acid.

Addition of 2.5 g of oxalic acid in the sample preparation affects the morphology of the sample as very uniform rods of micrometre (µm) sized length and equal width are formed. MoV-5 shows "nano-rods" beginning to grow into one-another via an amorphous over layer, as seen in the top of the right hand side image, and is no longer uniform as

seen in sample MoV-2.5. Upon further addition of oxalic acid, 7.5 g (MoV-7.5), the formation of "saw" or "tooth" like growths along the edges of the rods growing into other rods are visible. For MoV-10, the morphology changed completely and only a few nano-rods are present. The material comprises of agglomerations, and amorphous and crystalline particles of irregular structure. The structure of MoV-12.5 is the same as that of MoV-10, but is more crystalline and less amorphous.

4.4.6 SEM and EDX

Surface morphology was examined for all catalysts using SEM and EDX analysis. All samples were composed of irregular particles with variable sizes. The individual particles contained a variable content of surface particles and surface cracks. The particles in sample MoV-0 were composed of agglomerated coarse crystals of different shapes, whilst the surface of sample MoV-1 shows a depression with fine crystals. The surface of sample MoV-2.5 has coarse flakes and irregular particles. The surfaces of the particles in samples MoV-5, MoV-7.5 and MoV-10 contain embedded fine needle like crystals, whilst sample MoV-12.5 shows a more crystalline surface [Fig.4.9].

The elemental composition of catalysts with the general formula MoV prepared with adding different amount of oxalic acid was determined by EDX. EDX analysis of multiple particles in all samples showed the presence of O, Mo and V and showed that the relative concentration of the elements are not affected, as evident from Table 4.8. Compositional variability was observed in almost all samples.

MoV-0   MoV-1

MoV-2.5   MoV-5

MoV-7.5   MoV-10
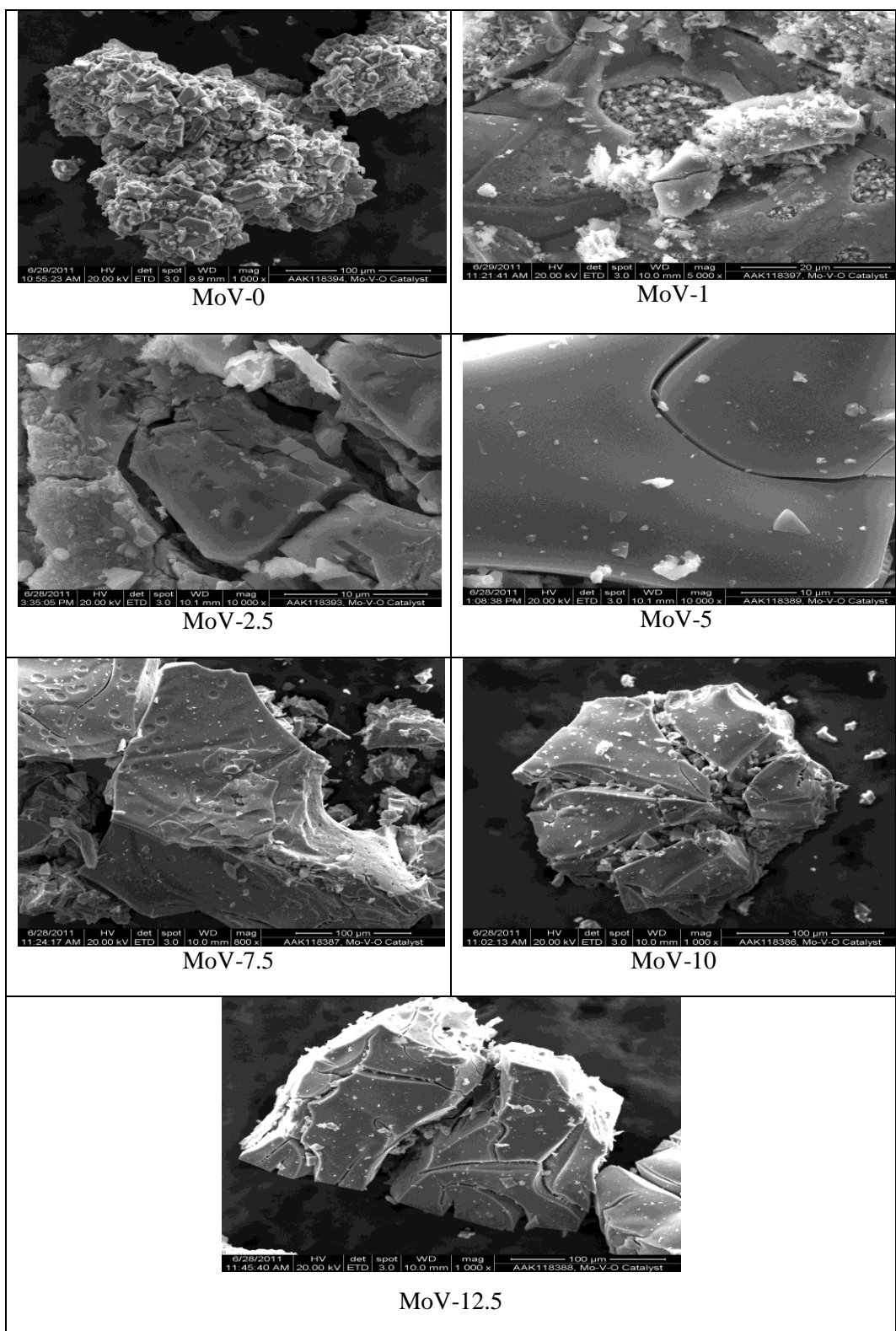
MoV-12.5

Fig.4.9: SEM images of catalysts prepared by varying oxalic acid amount.

Table 4.8: Elemental content of particles determined by EDX (wt %).

Cat. Ref.	O	Mo	V
MoV-0	33.0	57.2	9.8
MoV-1	28.5	58.3	13.2
MoV-2.5	28.9	56.0	14.0
MoV-5	31.7	55.4	11.7
MoV-7.5	32.2	55.6	12.3
MoV-10	32.6	55.2	13.2
MoV-12.5	30.1	59.3	10.7

4.5 Effect of the calcination temperature on the catalyst performance

The MoV-10 catalyst was further prepared as described in Chapter 2, and calcined at different temperatures of 200, 350, 400, 450 and 700 ºC. These catalysts were denoted as MoV-200, MoV-350, MoV-400, MoV-450 and MoV-700 respectively, as given in Table 4.9. These samples were tested in a fixed bed reactor as detailed in Chapter 2. The catalytic experiments were carried out for these samples at three different temperatures; 290 ºC, 310 ºC and 340 ºC, while pressure, feed flows and feed ratios were kept constant to determine the effect on catalytic activity. These samples were further characterized with BET total surface area analysis. XPS, XRD, SEM and EDX were also conducted.

Table 4.9: Catalysts calcined at different temperature.

Catalyst Ref.	Calcination temp. (°C)
MoV-Un	Uncalcined
MoV-200	200
MoV-350	350
MoV-400	400
MoV-450	450
MoV-700	700

4.5.1 Results of calcined catalysts

Catalysts calcined at different temperatures were tested at the same process conditions keeping pressure, feed flow and catalyst amount constant. Reaction temperatures were varied to evaluate the catalytic activities.

4.5.1.1 Reaction temperature impact on calcined catalyst activity

Calcined catalysts were tested at different reaction temperatures (290 - 340 °C), and their catalytic activity data are given in Tables 4.10 - 4.12. The catalytic activity of the catalyst first increases as the calcination temperature increases from 200 - 350 °C and then starts to decreases at higher calcination temperatures. The catalysts calcined at higher temperatures behave differently; MoV-450 calcined at 450 °C has a high CO selectivity, whilst MoV-700 calcined at 700 °C has a higher CO_2 selectivity with low ethane conversion.

Table 4.10: Catalyst activity results at 290 ºC and 70 psig pressure.

Catalyst	Conv. (%)		Selectivity (%)				Yield-(%)
Ref.	C_2H_6	O_2	CO_2	CO	C_2H_4	AA	C_2H_4
MoV-Un	1.8	8.2	16.5	10.8	70.1	2.7	1.3
MoV-200	2.9	9.6	10.5	12.0	72.9	4.6	2.1
MoV-350	21.8	68.9	4.3	8.4	68.8	18.5	15.0
MoV-400	10.1	33.5	5.3	11.2	61.9	21.6	6.3
MoV-450	5.7	12.1	8.3	48.1	37.6	6.0	2.1
MoV-700	0.8	1.5	34.4	10.6	55.0	0.0	0.4

Reaction conditions: Pressure = 70 psig, temp. = 290 ºC, feed gas = ethane: oxygen: nitrogen (40:10:50), catalyst wt. = 1 g, feed flow = 25 ml/min.

The increasing reaction temperature favours the formation of carbon monoxide and carbon dioxide, while AA selectivity remains constant. In the product distribution the carbon oxide selectivity increases and ethene selectivity decreases with increasing

reaction temperature. Catalysts calcined at 350 °C and 400 °C show high activity with high ethane conversion and low carbon monoxide and carbon dioxide formation, while also showing high AA formation, compared with the catalysts calcined at other temperatures.

Table 4.11: Catalyst activity results at 310 ºC and 70 psig pressure.

Catalyst	Conv. (%)		Selectivity (%)				Yield-(%)
Ref.	C_2H_6	O_2	CO_2	CO	C_2H_4	AA	C_2H_4
MoV-Un	2.7	10.6	19.6	13.6	63.2	3.6	1.8
MoV-200	4.3	12.1	10.9	19.1	64.7	5.2	2.8
MoV-350	27.2	96.6	6.7	11.3	66.6	15.4	18.2
MoV-400	14.2	47.0	6.6	15.2	57.9	20.3	8.2
MoV-450	7.1	23.5	8.8	53.4	32.8	5.0	2.3
MoV-700	1.7	3.6	35.8	11.3	49.2	3.7	0.8

Reaction conditions: Pressure = 70 psig, temp. = 310 ºC, feed gas = ethane: oxygen: nitrogen (40:10:50), catalyst wt. = 1 g, feed flow = 25 ml/min.

Table 4.12: Catalyst activity results at 340 ºC and 70 psig pressure.

Catalyst	Conv. (%)		Selectivity (%)				Yield-(%)
Ref.	C_2H_6	O_2	CO_2	CO	C_2H_4	AA	C_2H_4
MoV-Un	4.8	14.2	23.8	17.6	53.9	4.7	2.6
MoV-200	6.2	21.6	12.0	24.3	56.1	7.6	3.5
MoV-350	28.4	99.4	8.4	12.5	62.4	16.7	17.7
MoV-400	22.0	95.8	9.6	19.9	53.1	17.4	11.7
MoV-450	11.7	57.2	10.7	57.6	27.1	4.6	3.2
MoV-700	2.3	5.6	40.2	11.2	44.3	4.4	1.0

Reaction conditions: Pressure = 70 psig, temp. = 340 ºC, feed gas = ethane: oxygen: nitrogen (40:10:50), catalyst wt. = 1 g, feed flow = 25 ml/min.

This data clearly shows a modification in the catalytic properties of the catalysts at various calcination temperatures for both oxygen and ethane conversion. These catalysts

show a clear trend in ethane conversion (Fig. 4.10). The optimum performance is achieved with the catalyst calcined at 350 ºC which has low carbon oxide formation and high ethane conversion. The decrease in activity of the catalysts calcined above 350 °C could be due to a decrease in surface area or the formation of different phases or crystallinity of the materials, as discussed in the characterization sections.
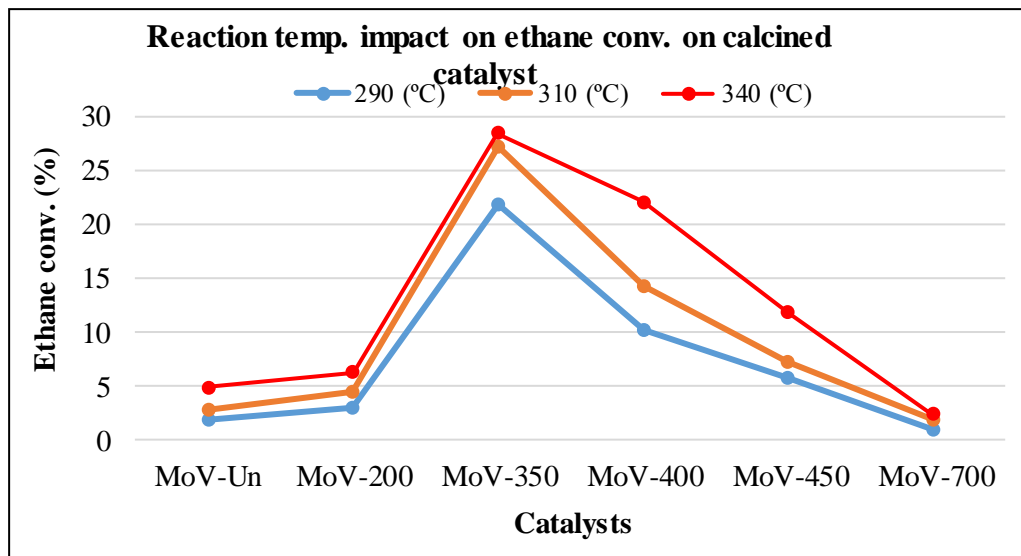
Fig.4.10: Ethane conversion vs. temperature for different calcined catalysts.

Both ethene selectivity and ethane conversion first increase, then decrease above 350 °C. The behavior of the catalysts varies at higher calcinations temperatures. The catalyst samples calcined at 450 °C and 700 °C show very different activity. The activity of MoV-450 does not increase with increasing reaction temperature, and only carbon monoxide formation increases significantly whilst the activity of sample MoV-700 decreases drastically and produces only carbon dioxide with increasing reaction temperature. The catalyst calcined at the lowest temperature, 200 ºC, has very low conversion of ethane and high selectivity towards ethene formation. The catalyst calcined at the moderate temperature of 350 ºC shows very high activity, with high ethane

conversion, high ethene selectivity and low CO_X formation. The catalysts calcined at 400

- 450 ℃, show significant change in their activity.

4.5.2 Characterization of catalysts calcined at different temperatures

 (i) BET

Table 4.13 shows the surface area of the MoV oxide catalysts calcined at different temperatures. The BET data shows the influence that calcination temperature has on the surface area of the samples. There is a small decrease in the surface area from uncalcined materials to calcined 400 ℃ (MoV-400), whilst there is sharp decrease in surface area from the samples calcined at 450 to 700 ℃. Sample MoV-700 shows a large loss in surface area which could be due to the formation of the bulk phase at 700 ℃.

Table 4.13: Surface area of catalysts calcined at different temperature.

Catalyst	Surface area (m^2/g)	
Ref.	Before calcination	After calcination
MoV-Un	25	25
MoV-200	24	24
MoV-350	23	20
MoV-400	24	19
MoV-450	23	15
MoV-700	24	2

(ii) XRD

The XRD patterns of the uncalcined sample and samples calcined at different temperatures show typical changes from amorphous to crystalline morphology. The comparison pattern presented in Fig. 4.11 shows some initial peaks being shifted from the amorphous phase.

126
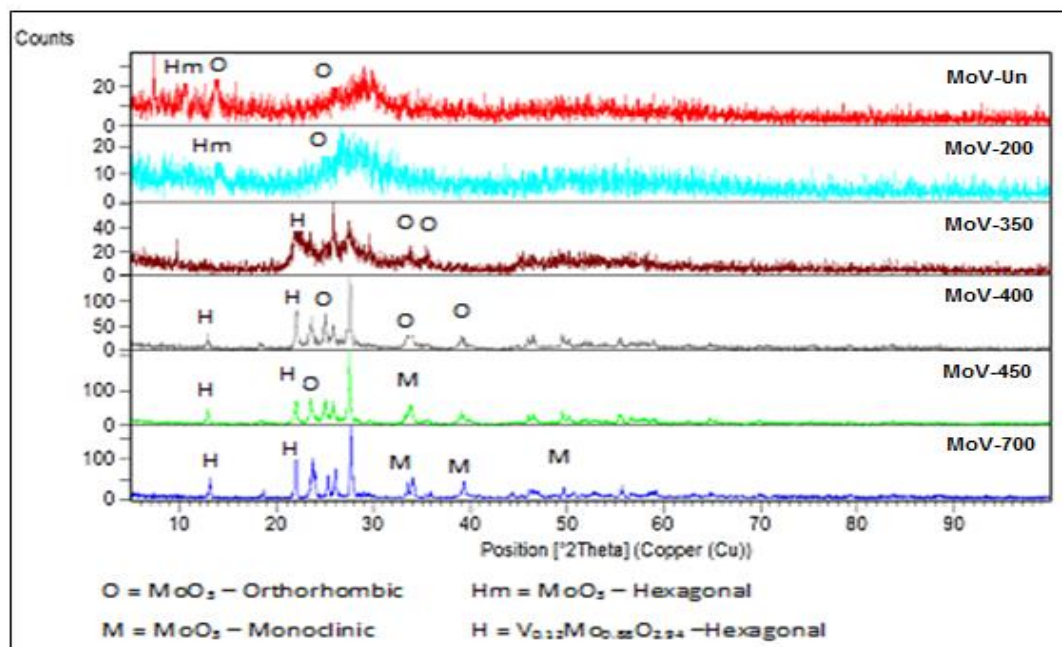
Fig.4.11: XRD patterns of calcined catalysts at different temperature.

Fig. 4.11 depicts the XRD patterns for the catalysts calcined at various temperatures. They contain reflection lines of different phases which were found to evolve as the calcination temperature was increased. The MoV-350 sample is amorphous with hexagonal phases observed. At the calcination temperature of 400 °C, crystalline structure starts to emerge with orthorhombic and hexagonal phases. For samples calcined at temperatures higher than 400 °C, the presence of the orthorhombic phase decreases and hexagonal phases becomes more prominent. However, at 700 °C the sample becomes more crystalline in structure with monoclinic phases. This phase transition is clearly evident from the diffractogram of samples calcined at different temperatures.

(iii) XPS

Binding energies (BE) of C, O, Mo and V and reduced vanadium species of the catalyst samples are given in Table 4.14-4.15, which match with literature values [10-11].

127

Table 4.14: Chemical content and their binding energies of all calcined catalysts.

Catalyst	Binding Energies (eV)				Contents (At %)				Ratio
Ref.	C1s	O1s	Mo3d	V2p	C1s	O1s	Mo3d	V2p	V:Mo
MoV-Un	284.5	530.7	232.5	516.8	30.4	56.0	9.9	3.7	0.37
MoV-200	284.5	530.7	232.6	516.9	28.2	56.2	11.4	4.2	0.37
MoV-350	284.5	530.4	232.8	517.4	24.1	56.3	13.5	6.1	0.45
MoV-400	284.4	530.6	233	517.6	23.8	56.4	14	5.8	0.41
MoV-450	284.5	530.6	232.9	517.4	23.8	56.9	13.9	5.4	0.39
MoV-700	286.2	530.5	232.8	516.7	24.4	57.8	14.5	3.2	0.22

Table 4.15: Oxidation ratios of V^{4+} and V^{5+} and their binding energies of catalysts.

Catalyst	BE (eV)			FMHM (eV)			Ratio
Ref.	V2p	$V2p^{5+}$	$V2p^{4+}$	V2p	$V2p^{5+}$	$V2p^{4+}$	$V^{4+}:V^{5+}$
MoV-Un	516.8	-	-	1.867	-	-	-
MoV-200	516.9	-	-	1.979	1.75	0.67	0.07
MoV-350	517.4	517.3	516.2	1.812	1.36	1.16	0.32
MoV-400	517.6	517.6	516.5	1.913	1.34	0.98	0.26
MoV-450	517.4	517.4	516.3	1.553	1.43	0.95	0.17
MoV-700	516.7	-	-	0.28	-	-	-

All calcined catalyst with V2p and Mo3d peaks have BEs of 516.8 and 232.6 respectively, which are typical for V (V) and Mo (VI). The uncalcined catalyst and the calcined catalyst at 700 °C do not show the presence of V^{5+} and V^{4+}. However, all catalysts show V and Mo content. The atomic ratio of catalyst MoV-700 is the lowest compared to the other samples, as shown in Table 4.14. Catalyst MoV-700 has a low V content possibly due to elemental vanadium caused by the calcination at 700 °C.

(iv) SEM and EDX

Surface morphology with elemental composition analysis of all calcined catalysts was carried out with SEM and EDX, as explained in Chapter 2. All samples were composed of irregular particles having variable size, as shown in Fig. 4.11.
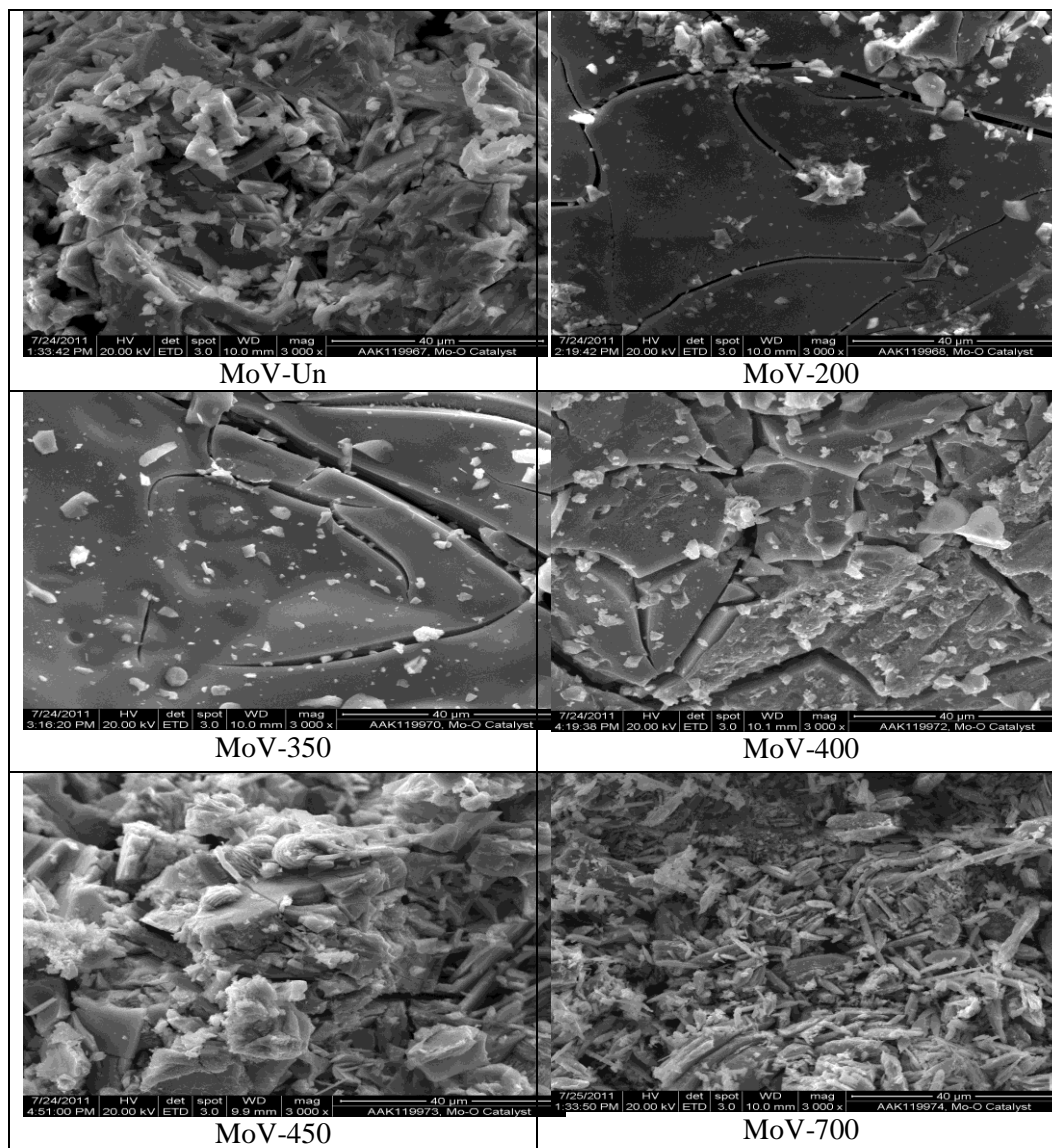
Fig.4.12: SEM images of samples calcined at different temperature.

The individual particles have variable contents of surface particles with surface cracking. The rough surfaces generally contained embedded and agglomerated crystals of variable size, as in Fig. 4.11. MoV-Un and MoV-200 both show embedded crystal like features.

MoV-350 and MoV-400 both show fine structure with cracks and surface attached particles. MoV-450 and MoV-700 show agglomerated surface crystals and the catalyst shows much lower activity towards ODH of ethane.

Table 4.16: Elemental content of particles determined by EDX (wt %).

Cat. Ref.	C	O	Mo	V
MoV-Un	1.7	43.3	44.8	9.3
MoV-200	1.6	48.1	42.0	8.3
MoV-350	0.0	32.8	55.4	11.8
MoV-400	0.0	31.0	55.4	13.6
MoV-450	0.0	30.4	56.3	13.4
MoV-700	0.0	32.7	56.3	11.1

EDX analysis of multiple particles in all samples showed the presence of O, Mo and V. The MoV-Un and MoV-200 samples showed a small amount of carbon. Compositional variability was observed in almost all samples, as shown in Table 4.16.

4.6 Catalyst reproducibility and stability test

Catalyst $Mo_1V_{0.40}$ with a molybdenum and vanadium ratio of 2.5:1 was prepared in three different batches to determine the reproducibility of catalyst activity and product selectivity. These catalysts were prepared using the same preparation procedure (temperature, pH and drying time), calcined at 350 ºC for 4 h in air and labeled MoV-350-1, MoV-350-2 and MoV-350-3.

4.6.1 Results of reproduced catalysts

Catalytic activity data of the three batches is presented in Table 4.17.

Table 4.17: Catalytic activity data of reproduced catalysts.

Catalyst	Conv. (%)		Selectivity (%)				Yield (%)
Ref.	C_2H_6	O_2	CO_2	CO	C_2H_4	AA	C_2H_4
MoV-350-1	21.8	68.9	5.3	8.4	67.8	18.5	14.8
MoV-350-2	22.4	70.8	6.1	8.1	67.3	18.6	15.1
MoV-350-3	22.9	69.2	6.6	7.5	67.8	18.1	15.5

Reaction conditions: Pressure = 70 psig, temp. = 290 ºC, feed gas = ethane: oxygen: nitrogen (40:10:50), catalyst wt. = 1 g, feed flow = 25 ml/min.

The reproduced catalysts data indicate that the catalysts of similar composition prepared with the same procedure at different times show very good reproducibility of the catalyst.

4.6.2 Characterization of reproduced catalyst

(i) BET

Table 4.18 shows surface area of molybdenum vanadium (MoV-350) catalysts prepared in different batches. The surface area results show that all three batches of MoV-350 catalyst have a similar surface area, from 21 - 22 m^2/g. The surface area of these catalysts indicates good reproducibility.

Table 4.18: Surface area of reproduced (MoV-350) catalysts.

Catalyst Ref.	Surface area (m^2/g)
MoV-350-1	21
MoV-350-2	22
MoV-350-3	22

(ii) TGA

Thermogravimetric analysis (TGA) was carried out on an uncalcined sample and a calcined sample (standard that was calcined at 350 °C) to determine the weight changes

upon thermal activation in air at 10 °C/min ramp until 800 °C, as shown in Figs. 4.13 and 4.14. During thermal activation, initial mass loss occurred due to the removal of H_2O and NH_3, $\approx$ 4.4 wt% up to 200 °C. After 200 °C, there was a sharp loss in weight ($\approx$ 27 wt %) up to 300 °C. There was a slight weight gain between 300-390 °C and then a further decrease. This transient behavior may be interpreted as the establishment of a steady state of an average oxide stoichiometry, below the nominally fully oxidized composition. The thermal graph shows slight weight loss ($\approx$ 31wt %) until 400 °C. There is no weight change in the temperature range between 400 and 650 °C. However, above 650 °C a large endotherm is observed, which is likely to be due to phase changes and the sudden weight loss ($\approx$ 59 wt %) until the final activation temperature is reached (Fig. 4.13).
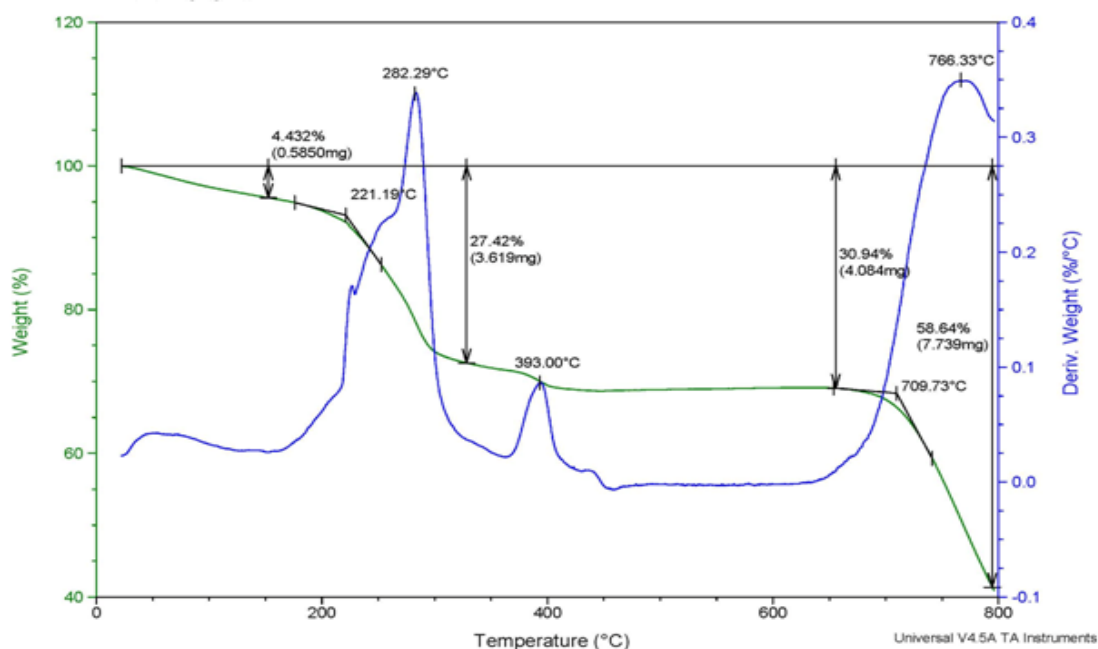
Fig.4.13: TGA of uncalcined (MoV) precursor weight losses upon thermal activation.

132
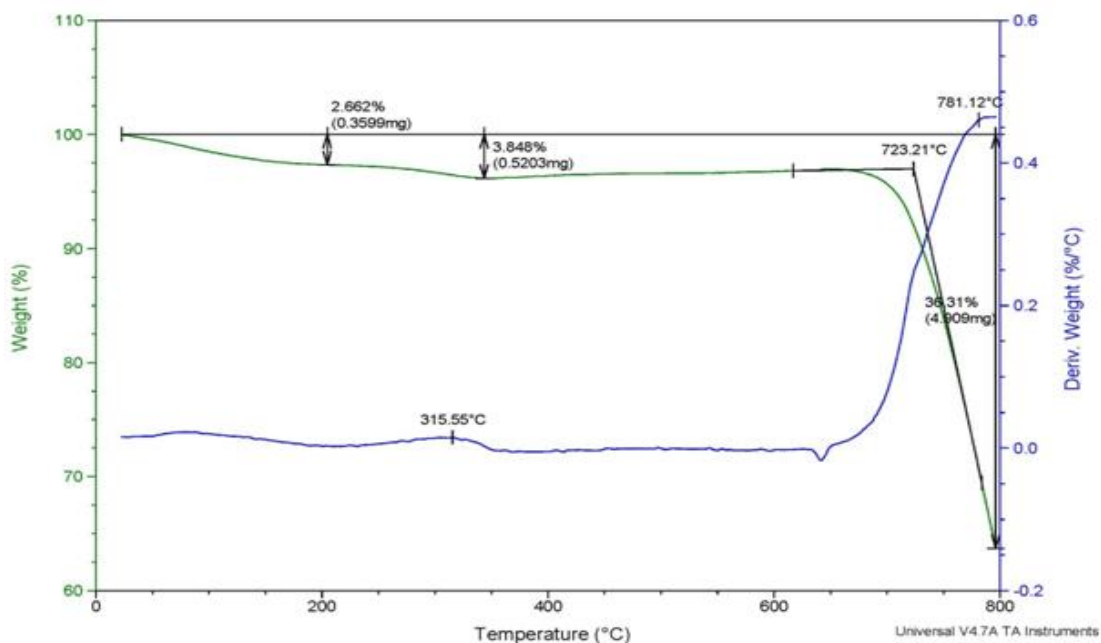
Fig.4.14: TGA of standard (MoV-350) sample weight losses upon thermal activation.

The TGA of the standard catalyst sample (MoV) that was calcined at 350 °C upon thermal activation is shown in Fig. 4.14. There was little weight loss ($\approx$ 4 wt %) until 650 °C. Similar behavior was observed between 300-350 °C with a slight weight gain, as seen in both the uncalcined precursor and calcined sample. The sample material calcined at 350 °C is more active than any of the catalysts calcined at other temperatures, meaning that this catalyst has active phases that are the most favourable for the ODH of ethane to ethene.

4.6.3 Catalyst stability test

Catalyst MoV-350 was tested for a longer time on stream to determine the stability of the catalyst over time. The catalytic experiments were carried out at 70 psig in a fixed bed tubular reactor (i.d. 3/8") at a fixed temperature (290 ºC). Reaction analysis was maintained for 30 days online. This catalytic analysis data is shown in Fig. 4.14.
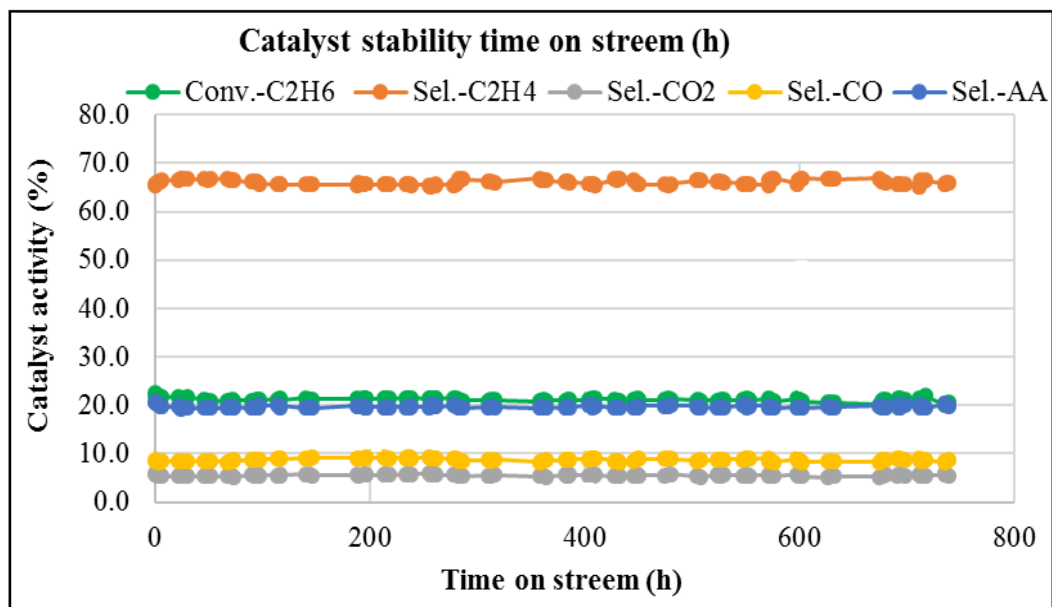
Fig.4.15: Catalyst (MoV-350) stability runs on time on stream 739 h.

4.6.3.1 Results of stability test

Catalytic data shows that catalyst MoV-350 was run on stream for more than one month (739 h) without any decrease in ethane conversion or product selectivity. This catalyst was analyzed for its characteristic properties.

(i) BET

Table 4.19 shows fresh and spent catalysts have similar surface area, between 21 - 22 m^2/g. These results indicate that there is no effect on catalyst surface area after running under reaction conditions for 739 h.

Table 4.19: Surface area of spent (MoV-350) catalyst.

Catalyst Ref.	Surface area (m^2/g)
MoV-350-fresh	21
MoV-350-spent	22

(ii) XPS

XPS results indicate that there is no change in surface of the catalyst after running under reaction conditions for 739 h. The binding energies as well the ratio of reduced vanadium remain the same. These results are presented in Table 4.20.

Table 4.20: Oxidation states ratios of V^{4+} and V^{5+} and their binding energies.

Catalyst	BE (eV)			FMHM (eV)			Ratio
Ref.	V2p	V2p^{5+}	V2p^{4+}	V2p	V2p^{5+}	V2p^{4+}	$V^{4+}:V^{5+}$
MoV-350-fresh	517.4	517.3	517.3	1.812	1.36	1.16	0.33
MoV-350-spent	517.3	517.3	516.2	1.813	1.35	1.16	0.32

4.7 Discussion

The interpretation of different characterization techniques propose that the MoV oxide composition constitutes an extremely efficient intermediate for the ODH process. The calcination temperature has a direct impact on the catalytic activity of the sample as a result in the formation of active phases. The surface area of the samples calcined at different temperatures decreases with increasing calcination temperature. The surface area decreases from 25 to 2 m^2/g when temperature increases from 200 - 700 °C. XRD of the samples calcined at different temperatures as depicted in Fig.4.10 shows complex phase patterns. These phases formed in the Mo-V-O system are orthorhombic, hexagonal and tetragonal [18]. For most of the samples small lines were observed, indicating amorphosity with the formation of MoO_3 in hexagonal and orthorhombic forms. With increasing calcination temperature the formation of $(V_{0.07}Mo_{0.93})_5O_{14}$ was noted. Calcined catalysts showed sharp and intense peaks after 350 °C, presented in all samples at $2\theta =$ 9.7, 13.4 and 25.6 ° [19]. These suggest a crystalline structure of the orthorhombic and

hexagonal phases. Orthorhombic phases of MoO_3 and tetragonal $(V_{0.07}Mo_{0.93})_5O_{14}$ (JCPDS 31-1437) reflections at 22 °, 27.8 ° were present [20].

The XPS data also showed the presence of MoO_3 and V_2O_5 in the samples. The reduciblity property of the vanadium species decreases when the samples are calcined at temperatures higher than 350 °C. There are no reduced vanadium species seen in either MoV-Un or MoV-700. This clearly indicates that the catalytic activity also depends on the presence of V^{4+} species in samples. As seen in Table 6.7, the ratio of V^{4+}/V^{5+} species is highest when the sample was calcined at 350 °C and this ratio lessens with further increasing calcination temperature.

The SEM micrographs of samples exhibit agglomerated crystals with a rod-like morphology. There is no clear dependency of the morphology on the various calcination temperatures used. They fully support the trends understood from EDX composition, BET, and due to phase changes. . The calcination temperature determines the effect on the physiochemical properties of MoV mixed oxide catalysts. Phase evolution was clearly evident due to variation of calcination temperature. The results highlight the benefits of the study on various calcination temperatures in order to reach the required active phase.

The amorphous character of the active catalysts (MoV oxide) prepared with oxalic acid make it difficult to propose an accurate description of these catalysts. Hexagonal mixed oxides like $V_xMo_{1-x}O_{3-x/2}$ and tetragonal θ-$(VMo)_5O_{14}$ cannot be distinguished by XRD (most of the major XRD reflections lie in the same 2θ-range), nor by Raman spectroscopy (Mo-O-V vibrations give rise to similar peaks of Mo-O-Mo in the same range of wavenumbers). Merzouki et al. [21] assumed that MoV(Nb) catalysts are composed of θ-$(VMo)_5O_{14}$ and α-MoO_3 nanoparticles. Similar phases were assumed to be present on MoVNbPd catalysts by Mestl [5], although some of the excess of V is

certainly present as α-$V_xMo_{1-x}O_{3-0.5x}$. Indeed, the presence of the θ-phase accounts for the similarity between MoVNb catalysts and the industrial MoVW catalyst of acrolein oxidation [22, 23], because W, like V and Nb, is known to stabilize the θ-oxide [9]. The frame work of θ-Mo_5O_{14} contains MoO_7 pentagonal bipyramids, the equatorial edges of which are shared with five MoO_6 distorted octahedral ($[MoO_7]$, $5MoO_6$) clusters. This pattern is isolated from three others by corner shared MoO_6 octahedra. Vanadium (as V^{4+}) replaces Mo in the octahedral structure, whilst Nb^{5+}, whose size is large enough to be 7-coordinated (ionic radius $r = 0.69$Å), shown in Table 4.21, reported by Shannon [24] with the optical basicity of some cations [25, 26], may be located in pentagonal bipyramids. Because of this, there is no need to consider Mo^{4+} ions ($r = 0.65$Å) which are known to be detrimental to catalytic activity. The large width of the (001) line of θ-$(VMoNb)_5O_{14}$ nanocrystal accounts for a high degree of disorder in the stacking of (001) planes, which could be promoted by insertion of V or Nb. The same interpretation may be proposed for V in the case of stacked (010) planes of orthorhombic α-$V_xMo_{1-x}O_{3-0.5x}$.

Table 4.21: Ionic radius [24] and optical basicity Λ [25, 26] of some active cations.

Cation	Ionic radius(Å)	CN*	Optical basicity(Λ)	Cation	Ionic radius(Å)	CN*	Optical basicity(Λ)
V^{5+}	0.36	4	0.69	V^{4+}	0.54	6	0.63
V^{5+}	0.58	6	0.68	V^{3+}	0.64	6	0.55
Mo^{6+}	0.41	4	0.55	Mo^{5+}	0.59	6	0.52
Mo^{6+}	0.61	6	1.17	Mo^{4+}	0.65	6	0.96
Nb^{5+}	0.48	4	0.64	Nb^{5+}	0.64	6	0.61
Nb^{5+}	0.69	7	0.6	Nb^{4+}	0.68	6	0.81
W^{6+}	0.42	4	0.54	W^{6+}	0.60	6	0.51
Fe^{2+}	0.61	6	1.00	Fe^{3+}	0.55	6	0.77
Pd^{2+}	0.64	4(square)	0.85	Pd^{2+}	0.86	6	1.11

*CN: Coordination number

Merzouki [27] for V-P-O catalyst and Seoane [28] for V_2O_5 reported that palladium (Pd^{2+}) accelerates the rate of the $V^{5+} + e \leftrightarrow V^{4+}$ redox couple. When comparing the ionic radius and optical basicity for the same 6-coordination, V^{5+} ($\Lambda = 0.63$) or V^{4+} ($\Lambda = 0.63$) are close to those of Nb^{5+} ($\Lambda = 0.63$), while Mo^{6+} ($\Lambda = 0.52$) and W^{6+} ($\Lambda = 0.51$), both hexacoordinated, are slightly more acidic (Table 4.21). Conversely, Pd^{2+} is a soft cation, is more basic then the early transition metal cations ($\Lambda = 1.11$) and has a larger ionic radius, therefore the only way for Pd to be stabilized is to be trapped between layers. Indeed, these catalysts contain hexagonal channels. In the present MoV-oxides, oxalic acid reduces the vanadium oxides, shown in the XPS spectra (Fig. 4.7) by the varying ratio of V^{5+}/V^{4+} in the calcined catalysts, prepared with varying oxalic concentrations.

The growth of α-MoO_3 and α-$V_xMo_{1-x}O_{3-0.5x}$ particles is seen in the MoV-400 oxides but not in Nb-containing catalysts (MoVNb-400 and MoVNbPd-400), noted by Bouchard [29]. This means that these crystals are stabilized at a nanometer scale, which is more indirect evidence of the insertion of V in θ-$(VMoNb)_5O_{14}$ and in $V_xMo_{1-x}O_{3-0.5x}$. Bouchard [29] observed, during in-situ XRD reduction of MoVNb-350 by H_2, the formation of a $V_xMo_{1-x}O_2$ solid solution, while only MoO_2 was identified in MoV-350. For reasons as yet unknown, it seems that Nb promotes the formation of solid solutions of $(VMo)O_x$. Initially, attempts were made to explain this stabilization by considering the formation and 'isolation' [30] of the $[MoO_7]$, $5MoO_6$ clusters of θ-$(VMoNb)_5O_{14}$ coherently grown in a matrix of (010) α-MoO_3 [31-33].

The catalysts prepared with oxalic acid addition and all calcined at 350 °C behave similarly to those of Bouchard [29], who observed the crystals stabilized as nanometer size particles, as observed in high resolution transmission electron microscopy (TEM) Fig. 4.8. This also shows nano-rods beginning to grow into one-another via an amorphous top layer. The present studied findings concur with the findings of Werner [34] on

Mo_4VO_{14}, which is isostructural to θ-oxides. Using high resolution transmission electron microscopy, the authors showed that "a continuum random network of basic structural units (distorted octahedra) was detected made up of approximately circular clusters embedded in a quadratic network". However, the surface composition of several MoV catalysts with different amounts of oxalic acid do not show an excess of Mo, but typicallyshow a slight excess of V (except MoV-0 and MoV-12.5), as compared with the bulk stoichiometry. The crystal structure of V_2O_5 and related V_nO_{2n+1} suboxides is very close to that of α-MoO_3 (and thus of $V_{0.13}Mo_{0.87}O_{2.935}$), has a similar framework (corner-sharing and/or edge-sharing octahedral) and the same mean octahedral size. This is the reason why so many mixed oxides exist in the Mo-V-O system [35]. Therefore, layers or intergrowths of VO_x with θ-oxides (or part of its framework) could also be considered.

Bouchard [29] reported that both MoV-350 and MoVNb-350 have similar catalytic activity. They displayed the same high selectivity to ethene, which was attributed to the presence of θ-oxides. These catalysts are more active and selective to mild oxidation products (ethene and acetic acid) than MoVPd and VNbPd. The conversion of ethane varies by a factor of 2-3, the selectivity to AA is much lower than to ethene ($S_{AA}/S_{AA}+S_{EE}$ ≈ 0.2), and the selectivity to CO_x is about 4-15 % that of total selectivity of $S_{AA}+S_{EE}$. The direct contribution of Nb^{5+} as an active site in $VNbO_5$ seems very small [36], although Nb in Mo-V-Nb oxide was found to inhibit the total oxidation to carbon oxide [37]. Therefore, the catalytic properties of VNbPd are mainly due to vanadium oxide (also doped with Pd) as opposed to $VNbO_5$. It may be inferred that $(Pd)VO_x$ is responsible for the high selectivity to AA, possibly by facilitating the selective oxidation of ethene [38-40].

In the MoV oxide catalysts, Mo-oxides (MoO_x) and/or V-oxides (VO_x) (according to bulk and surface stoichiometry) are also present besides the θ-phase. According to the majority

of the studies, the optimum range of Mo/V/Nb/Pd is 1/0.25-0.40/0.10-0.12/0.05-0.10, and it seems virtually impossible for a unique phase to be responsible for catalytic properties, as in the existence of M1 and M2 [41, 42]. However, the main role is played by only Mo and V oxides as presently discussed based due to their ionic radius/coordination. The two MoV oxide based catalysts known to have a definite composition, and claimed to be highly active and selective in the (amm)oxidation of propane to acrylonitrile or acrylic acid [43-45], provide the opportunity for comparison with the present catalytic results of ODH of ethane to ethene (Tables 4.2 - 4.4).

4.8 Conclusion

Catalysts prepared with oxalic acid showed a greater activity compared to the catalysts prepared without oxalic acid using the slurry method. Catalysts prepared with oxalic acid with a pH between 3 – 4 shows a greater activity compared to catalysts with a lower or higher pH. Catalytic activity increases upon the addition of oxalic acid from 2.5 - 7.5 g, and then begins to decrease after the addition of more than 10 g of oxalic acid in the preparation procedure.

Catalysts prepared with little or no oxalic acid and those prepared with higher than 10 g of oxalic acid have a lower surface area of 12 - 14 m^2/g as well as a lower catalytic activity, showing lower ethane conversion. The other catalysts prepared with 2.5 - 10 g of oxalic acid have a relatively high surface area of 19 - 23 m^2/g and show high catalytic activity with high ethene selectivity and lower carbon oxide formation in the product stream.

The catalysts prepared with the addition of oxalic acid showed a significant change in their morphology and their structure changed from crystalline to amorphous. Catalysts prepared with little or no oxalic acid showed crystalline structure. The same behavior is

observed with catalysts prepared by the addition of 12.5 g of oxalic acid and shows a clear crystalline structure as depicted in Fig. 4.6. The catalysts prepared by the addition of 5 - 10 g of oxalic acid show amorphous structure and have higher activity than the catalysts with crystalline structure.

Oxalic acid was successfully used during catalyst preparation to modify the physiochemical properties of the $Mo_1V_{0.4}O_x$ catalyst for ethane ODH. Comparison shows that the addition of oxalic acid not only enhances the ethane conversion of the catalyst, but also improves its ethene selectivity and reduces the carbon oxide formation. This is due to the reduction of V^{5+} to V^{4+} by oxalic acid in the starting solution to provide a driving force for formation of $V_xMo_{1-x}O_{3-0.5x}$, which remains stable and enhances the ODH of ethane to produce ethene. In addition, the performance of the catalyst is strongly related to the amount of oxalic acid used during catalyst preparation. Catalysts prepared with 5 to 10 g of oxalic acid showed the highest ethane conversion and ethene selectivity as they contain the desired phase composition and good redox capacity. Therefore, employment of reductive oxalic acid improves the catalytic performance of the $Mo_1V_{0.4}O_x$ catalyst.

4.9 References

[1] P. Botella, P. Concepcion, J. M. Lopez-Nieto, J. Moreno, *Catal. Today* **99** (2004) 51.

[2] F. Ivars, P. Botella, A. Dejoz, J. M. Lopez-Nieto, P. Concepcion, M. I. Vazquez, *Top. Catal*. **38** (2006) 59.

[3] G. Y. Popova, T. V. Andrushkevich, G. I. Aleshina, L. M. Plyasova, M. I. Khramov, *Appl. Catal. A: Gen.* **328** (2007) 195.

[3] H. Tsuji, K. Oshima, Y. Koyasu, *Chem. Mater*. **15** (2003) 2112.

[4] E. Thorsteinson, T. P. Vilson, F. G. Young, and P. H. Kasai, *J. Catal.* **52** (1978) 116.

[5] G. Mestl, Ch. Linsmeier, R. Gottschall, R. Dieterle, J. Find, D. herein, J. Jager, Y. Uchida, R. Schloegl, *J. Mol. Catal. A: Chem*. **162** (2000) 463.

[6] M. Dieterle, G. Mestl, J. Jager, Y.Uchida, H. Hibst, R. Schlogl, *J. Mol. Catal. A: Chem*. **174** (2001) 169.

[7] L. Dupont, D. Larcher, M. Touboul, *J. Solid State Chem*. **143** (1999) 41.

[8] Y. Hu, P. K. Davies, *J. Solid State Chem*. **119** (1995) 176.

[9] T. Eckstrom, M. Nygren, *Acta Chem. Scand*. **26** (1972) 1836.

[10] L. Dambies, C. Guimon, S. Yiacoumi, E. Guibal, *Coll. Surf. A*. **77** (2001) 203.

[11] D. Kim, S.V. Kagwade, C. R. Clayton, *Surf. Interface Anal*. **26** (1998) 155.

[12] P. Botella, J. M. Lopez-Nieto, B. Solsona, A. Mifsud, F. Marquez, *J. Catal*. **209** (2002) 445.

[13] http://www.Iasurface.com

[14] http://www.srdata.nist.gov.

[15] G. W. Coulston, E. W. Thompson, N. Herron, *J. Catal.* **163** (1996) 122.

[16] S. Siegbahn, *ESCA*, *Atomic, Molecular and Solid State Structures Studied by Means of Electron Spectroscopy*, Uppasal: Almquist and Wiksell, (1967).

[17] V. V. Nemoshkalenko, V. G. Aleshin, *Electronic Spectroscopy of Crytals* (Kiev, Naukova Dumka), 1976.

[18] W. Ueda, K. Oshihara, *Appl. Catal. A.* **200** (2000) 135.

[19] A. H. Adams, H. Frank, T. Buhrmester, J. Kunert, J. Ott, H. Vogel, H. Fuess, *J. Mol. Catal. A.* **216** (2004) 67.

[20] T. Ushikubo, K. Oshima, A. Kayou, M. Varakamp, M. Hatano, *J. Catal.* **199** (1997) 394.

[21] M. Mezourki, E. Bordes, B. Taouk, L. Monceaux, *Stud. Surf. Sci. Catal.* **72** (1992) 81.

[22] K. Ruth, R. Kieffer, R. Burch, *J. Catal.* **175** (1998) 27.

[23] H. Hibst, L. Marosi, A. Tenten, *US 5,380,531* (1998) to BASF.

[24] R. D. Shannon, *Acta Cryst. Sect. A* **32** (1976) 751.

[25] A. Lebouteiller, P. Courtine, *J. Solid State Chem.* **137** (1998) 94.

[26] P. Moriceau, A. Lebouteiller, E. Bordes, P. Courtine, *Phys. Chem. Chem. Phys.* **1** (1999) 5735.

[27] M. Mezourki, B. Taouk, L. Tessier, E. Bordes, P. Courtine, *Stud. Surf. Sci. Catal.* **75** (1993) 753.

[28] J. L. Seoane, P. Boutry, R. Montarnal, *J. Catal.* **63** (1980) 191.

[29] M. Bouchard, M. Roussel, E. Bordes-Richard, K. Karim, S. Al-Sayari*, Catal. Today* **99** (2005) 77.

[30] J. L. Challahan, R. K. grasselli, *J. Am. Inst. Chem. Eng.* **9** (1963) 755.

[31] E. Bordes, P. Courtine, *Appl. Catal. A: Gen.* **157** (1997) 45.

[32] E. Bordes, P. Courtine, *Stud. Surf. Sci. Catal.* **110** (1997) 177.

[33] E. Bordes, *Top. Catal.* **15** (2001) 21.

[34] H. Werner, O. Timpe, D. Herein, Y. Uchida, N. Pfander, U. Wild, R. Schlogl, *Catal. Lett.* **44** (1997) 153.

[35] E. Bordes, P. Courtine, *Stud. Surf. Sci. Catal.* **67** (1991) 21.

[36] P. Moriceau, A. Lebouteiller, E. Bordes, P. Courtine, *Phys. Chem. Chem. Phys.* **1** (1999) 5735.

[37] R. H. H. Smits, K. Seshan, J. R. H. Ross, L. C. A. van den Oetelaar, J. H. Helwegen, M. R. Anatharaman, H. H. Bronggersma, *J. Catal.* **157** (1995) 584.

[38] O. Desponds, R. L. Keiski, G. A. Somorjai, *Catal. Lett.* **19** (1993) 17.

[39] D. Linke, D. Wolf, M. Baerns, O. Timpe, R. Schlogl, U. Dingerdissen, *J. Catal.* **205** (2002) 16.

[40] A. Khodakov, B. Olthof, A. T. Bell, E. Iglesia, *J. Catal.* **181**(1999) 205.

[41] L. Tessier, E. Bordes, M. Gubelmann-Bonneau*, Catal. Today* **24** (1995) 335.

[42] J. M. M. Millet, H. Roussel, A. Pigamo, J. L. Dubois, J. C. Dumas, *Appl. Catal. A: Gen*. **232** (2003) 77.

[43] T. Katou, D. Vitry, W. Ueda, *Chem. Lett*. **32** (2003) 1028.

[44] P. De. Santo Jr., D. J. Buttrey, R. K. Grasselli, C. G. Lugmair, A. F. Volpe, B. H. Toby, T. Vogt, *Top. Catal*. **23** (2003) 23.

[45] P. De. Santo Jr., D. J. Buttrey, R. K. Grasselli, C. G. Lugmair, A. F. Volpe, B. H. Toby, T. Vogt, Z. Krist, *Top. Catal*. **219** (2004) 152.

Chapter 5

Influence of the different oxide supports on the activity of MoV oxides catalyst.

5.1 Introduction

This chapter focuses on studying the influence of oxide supports of zirconium, titanium, niobium, silica and alumina on MoV oxide based ($Mo_1V_{0.4}O_x$) catalyst, and compares the influence of the specific oxide support phase on base oxide catalysts. The MoV oxide catalyst has some unique physical and chemical characteristics compared to other supported oxide catalysts for the ODH of ethane. The supported oxide catalysts were investigated by X-ray photoelectron spectroscopy (XPS), X-ray diffraction (XRD) and surface area (BET) in order to determine the molecular structure and monolayer coverage of the surface MoV oxide phase, on oxide supports (ZrO_2, Nb_2O_5, TiO_2, SiO_2 and Al_2O_3).

Catalysts were prepared with 30 wt% support as described in Chapter 2, keeping the Mo and V molar ratio at 2.5:1, denoted as MoV-Zr, MoV-Nb, MoV-Ti, MoV-Si and MoV-Al respectively. These samples were tested under standard process conditions to observe their ODH of ethane activity at different temperatures.

5.2 Experimental results

The details of catalyst testing have been discussed in Chapter 2. Catalysts were tested for the ethane ODH reaction at temperatures in the range of 290 – 330 ºC.

5.2.1 Supports impact on catalytic activity

The catalytic ODH of ethane to ethene over supported MoV oxide catalysts in the gas phase was carried out at different reaction temperatures. The catalytic performance at each reaction temperature is illustrated in Fig. 5.1, and the catalytic activity and selectivity at each temperature are summarized in Table 5.2. The products detected included ethene, acetic acid (AA), CO and CO_2. Among the supported cataysts tested, the highest ethane conversion was obtained on the zirconia supported catalysts. However, it was slightly less active than the unsupported catalyst at low temperature (290 °C). At low conversion under low reaction temperatures, the selectivity to ethene over the supported catalysts was more than 80 %, which decreased gradually upon increasing temperature.

Ethane conversion and selectivities were measured for all supported catalysts at constant temperature (290 °C) and reactant pressure (70 psig) to determine their catalytic performance. Data for all supported catalysts are presented in Table 5.1.

Table 5.1: Catalytic activity results of supported catalysts at 290 °C.

Catalyst	Conversion (%)		Selectivity (%)				Yield (%)
Ref.	C_2H_6	O_2	CO_2	CO	AA	C_2H_4	C_2H_4
MoV-Zr	14.1	51.6	6.3	11.4	3.7	78.7	11.1
MoV-Nb	13.5	49.7	8.0	13.4	2.4	76.3	10.3
MoV-Ti	12.9	43.4	7.8	14.6	2.6	75.0	9.7
MoV-Si	7.4	24.8	6.3	12.6	1.8	79.4	5.8
MoV-Al	10.3	32.8	5.2	11.8	2.2	80.7	8.3
MoV-std	16.8	55.9	7.2	14.3	2.8	75.8	12.8

Reaction conditions: Pressure = 70 psig, temp. = 290 ºC, feed gas = ethane: oxygen: nitrogen (40:10:50), catalyst wt. = 1 g, feed flow = 25 ml/min.

The standard unsupported catalyst gave 17 % ethane conversion with 13 % ethene yield, higher than all supported catalysts. Zirconia, niobium oxide and titania supported catalysts have high ethane conversion compared to the silica and alumina supported catalysts at this temperature. Ethene selectivity is similar for all and the alumina supported catalyst shows the highest 81 %. Silica supported catalysts show low activity with 7 % ethane conversion. Results also show a slight decrease in carbon oxide (CO_x) selectivity in all supported catalysts compared to the standard unsupported catalyst, which could be due to a low concentration of active metals, as a result of up to 30 wt% supports used. These activity trends match those reported by Iglesia [1] for $MoVNbO_x$ catalysts supported over TiO_2, ZrO_2, and Al_2O_3.

5.2.2 Temperature impact on catalytic activity

To evaluate the ethane conversion levels and product selectivities of the supported catalysts, they were tested at different temperatures (290 - 330 °C). The temperature increment has a direct impact on ethane conversion and product selectivities. The CO_x selectivity increases greatly with ethane conversion, as temperature increases. AA selectivity increases marginally with temperature as ethene selectivity decreases (from 81

to 64 %). Niobium oxide, titania and silica supported catalysts show a greater CO_x formation compared to zirconia and alumina supported catalysts. At high (330 °C) temperature, alumina supported catalysts gave the highest ethene selectivity (64 %) with 24 % ethane conversion. Data of all supported catalysts at different temperatures are presented in Table 5.2.

Table 5.2: Supported catalysts activity at different temperatures.

Temp. (°C)	290		310		320		330	
(%)	Conv.	Sel.	Conv.	Sel.	Conv.	Sel.	Conv.	Sel.
Cat. Ref.	C_2H_6	C_2H_4	C_2H_6	C_2H_4	C_2H_6	C_2H_4	C_2H_6	C_2H_4
MoV-Zr	14.1	78.7	17.4	73.6	23.1	68.1	25.3	59.7
MoV-Nb	13.5	76.3	18.3	68.2	23.7	58.9	24.2	56.5
MoV-Ti	12.9	75	16.4	69.7	19.5	65.1	20.4	62.6
MoV-Si	7.4	79.4	15	68.9	19.2	65.2	20.9	59.1
MoV-Al	10.3	80.7	17.9	74.9	22.8	70.1	24.2	63.8
MoV-std	16.8	75.8	19.8	66.2	23.5	58.6	23.7	57.2

Reaction conditions: Pressure = 70 psig, feed gas = ethane: oxygen: nitrogen (40:10:50), catalyst wt. = 1 g, feed flow = 25 ml/min.

In terms of selectivity to carbon dioxide and AA, only a slight difference among the supported catalysts is observed. Significant changes were observed in the ethene and carbon monoxide formation and ethane conversion at the different temperatures. Ethane conversion increases with increasing temperature for all tested catalysts. At 320 °C the unsupported catalyst reaches a saturation point where all oxygen is consumed (conversion of O_2 = 100 %) with 23.5 % ethane conversion, while supported catalysts continue to consume oxygen. At 330 °C, the ethane conversion of unsupported catalysts remains the same but activity decreases due to increasing CO_x formation. Zirconia, niobium oxide and alumina supported catalysts show higher ethane conversion (>24 %) compared to that of unsupported catalyst at high temperature (330 °C).

At 290 °C zirconia, niobium oxide and titania supported catalysts have better activity than alumina and silica supported catalysts. Silica supported catalyst show the lowest activity compared with other supported catalysts at all temperatures tested. While at higher temperatures (greater than 300 °C) supported catalysts ethane conversion pattern changed as depicted in Fig.5.1. In many oxidation reactions moisture is usually present as a component in the feed as well as a product of the reaction. Wachs [2] reported that the oxide supports have different capabilities to activate oxygen. Catalyst with vanadium species supported on Al_2O_3, TiO_2, Nb_2O_5 and CeO_2 had an effect of oxygen species transform upon adsorption on the metal oxide surface but it has less effect on silica supported vanadium catalysts.
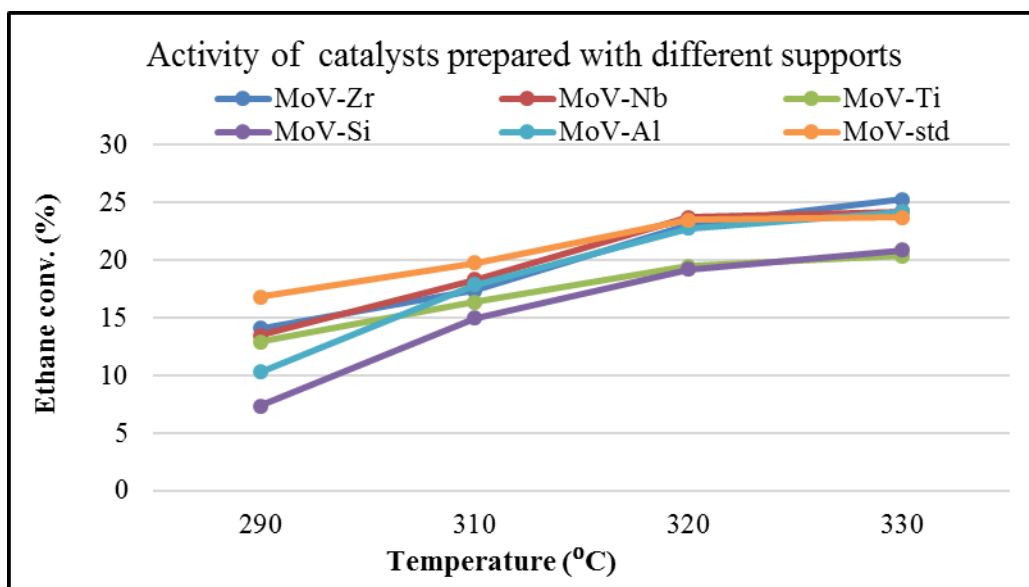
Fig.5.1: Supported catalysts activity, temperatures vs. ethane conversion.

Catalysts supported with alumina and zirconia has a greater activity at higher temperatures compared to the other supported catalysts. These catalysts display a greater activity than the unsupported standard catalysts in terms of ethane conversion and ethene

selectivity and have low CO_x formation, though the formation of AA remains almost constant. Overall, the zirconia catalyst is the best supported catalyst.

5.3 Results of characterization of supported catalysts

5.3.1 BET

The surface area (BET) of the catalysts was measured for all supported material as described in Chapter 2. The surface areas of the oxide supports (calcined at 350 °C) were slightly higher than the supported catalysts. The surface areas of the supported catalysts were in the range of 17-53 m^2/g as given in Table 5.3.

Table 5.3: Surface area of the catalysts prepared with different supports.

Catalyst Ref.	Oxide supports (m^2/g)	Uncalcined catalyst (m^2/g)	Calcined catalysts (m^2/g)
MoV-Zr	22	20	17
MoV-Nb	27	25	23
MoV-Ti	26	23	21
MoV-Si	56	55	53
MoV-Al	23	21	19
MoV-std	-	25	23

The uncalcined catalysts have a higher surface area than the calcined catalysts. The standard catalyst without a support has a moderate surface area (23 m^2/g). The silica supported catalyst shows a higher surface area than the other supported catalysts and also shows least activity towards ethane oxidative hydrogenation.

5.3.2 XRD

XRD patterns of all supported catalysts obtained show that the phases change with the support used. The majority of peaks assigned to α-MoO_3 are shifted from the standard pattern (JCPDS 76-1003). Other than these shifted peaks several other phases can be

identified in other samples. In all samples, a common Mo-containing peak is indicated by the presence of a line at d (Å)/2θ = 3.56/25.7 °.
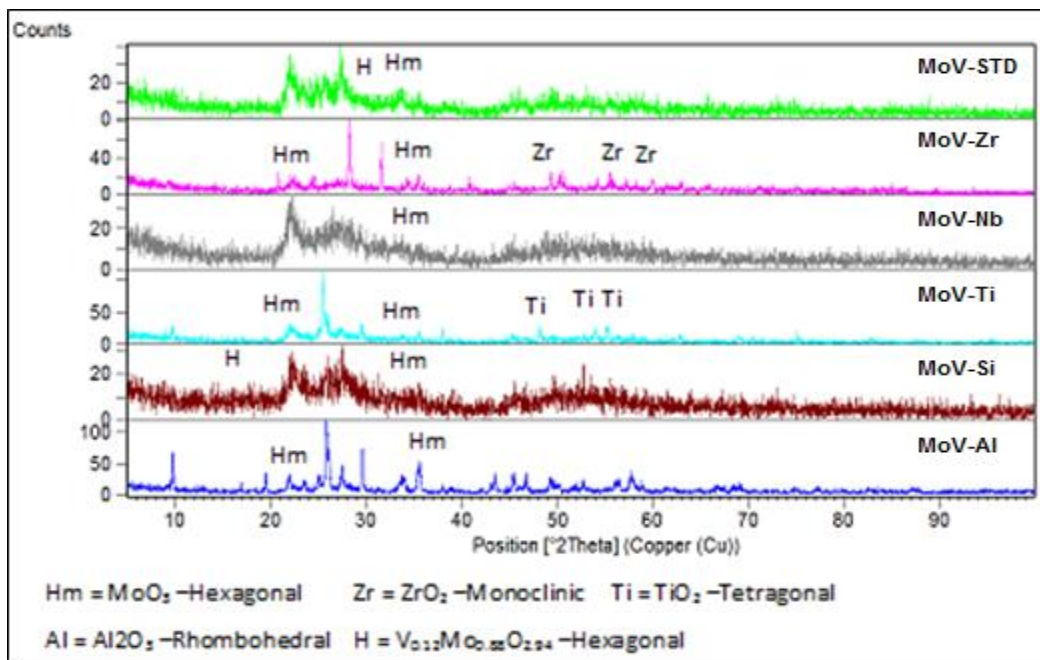
Fig.5.2: XRD patterns of different oxide supported catalysts.

Fig. 5.2 shows XRD patterns for supported and unsupported catalysts. From the XRD, two types of patterns are seen; unsupported, MoV-Nb, and MoV-Si are similar and have amorphous structure, while MoV-Zr, MoV-Ti and MoV-Al have crystalline structure [3]. These XRD patterns for bulk (unsupported) and supported MoV oxide on titania supports resemble those reported in previously prepared samples [4]. The peaks at 2θ value of 22.5 ° get weaker due to the crystallinity of the patterns while the lines at 25-30 ° become stronger. The use of ZrO_2 and Al_2O_3 supports results in different oxide structures to those of unsupported or Nb_2O_5 and SiO_2 supported catalysts, while the titania supported catalyst shows a semi-crystalline structure.

5.3.3 XPS

XPS of all catalyst was performed as outlined in Chapter 2. The binding energies (BE) of Mo ($3d_{3/2}$, $3d_{5/2}$), V ($2p_{3/2}$), Zr ($3d_{3/2}$), Nb ($3d_{3/2}$,), Ti ($2p_{3/2}$), Si ($2p_{3/2}$) Al ($2p_{3/2}$) peaks were measured for each sample and the surface stoichiometry determined as given in Table 5.4.

Table 5.4: Binding energies of elements of supported catalysts.

Catalyst	BE (eV)						
Ref.	Mo3d	V2p	Zr3d	Nb3d	Ti2p	Si2p	Al2p
MoV-Zr	232.5	517.0	182.3	-	-	-	
MoV-Nb	232.6	517.1	-	207.2	-	-	-
MoV-Ti	232.4	516.9	-	-	458.9	-	-
MoV-Si	232.6	517.1	-	-	-	103.5	-
MoV-Al	232.9	517.3	-	-	-	-	-
MoV-std	232.8	517.3	-	-	-	-	-

Table 5.5: Results of V^{5+} and V^{4+} and compounds identified in supported catalysts

Catalyst Ref.	BE (eV) $V2p_{3/2}$	BE (eV) V^{5+} ($V2p_{3/2}$)	BE (eV) V^{4+} ($V2p_{3/2}$)	V^{4+}/V^{5+} ratio	Identified compounds
MoV-Zr	1.920	1.45	1.09	0.28	MoO_3, V_2O_5, V_2O_4, ZrO_2
MoV-Nb	2.040	1.30	1.30	0.60	MoO_3, V_2O_5, V_2O_4, Nb_2O_5
MoV-Ti	2.139	1.39	1.24	0.39	MoO_3, V_2O_5, V_2O_4, TiO_2
MoV-Si	2.050	1.61	1.08	0.24	MoO_3, V_2O_5, V_2O_4, SiO_2
MoV-Al	2.044	1.27	1.20	0.44	MoO_3, V_2O_5, V_2O_4
MoV-std	1.812	1.36	1.16	0.32	MoO_3, V_2O_5, V_2O_4

XPS analysis clearly shows the presence of molybdenum oxide, vanadium oxides and the oxide support in all catalysts. XPS results show the oxidation state of the surface vanadium species in supported and unsupported MoV catalysts, as in Table 5.5. XPS analysis of the alumina sample (MoV-Al) does not show the presence of

aluminium oxide compound, though Mo and V oxides were identified in the sample.

5.3.4 SEM

Images of all catalyst samples are shown in Fig. 5.3.
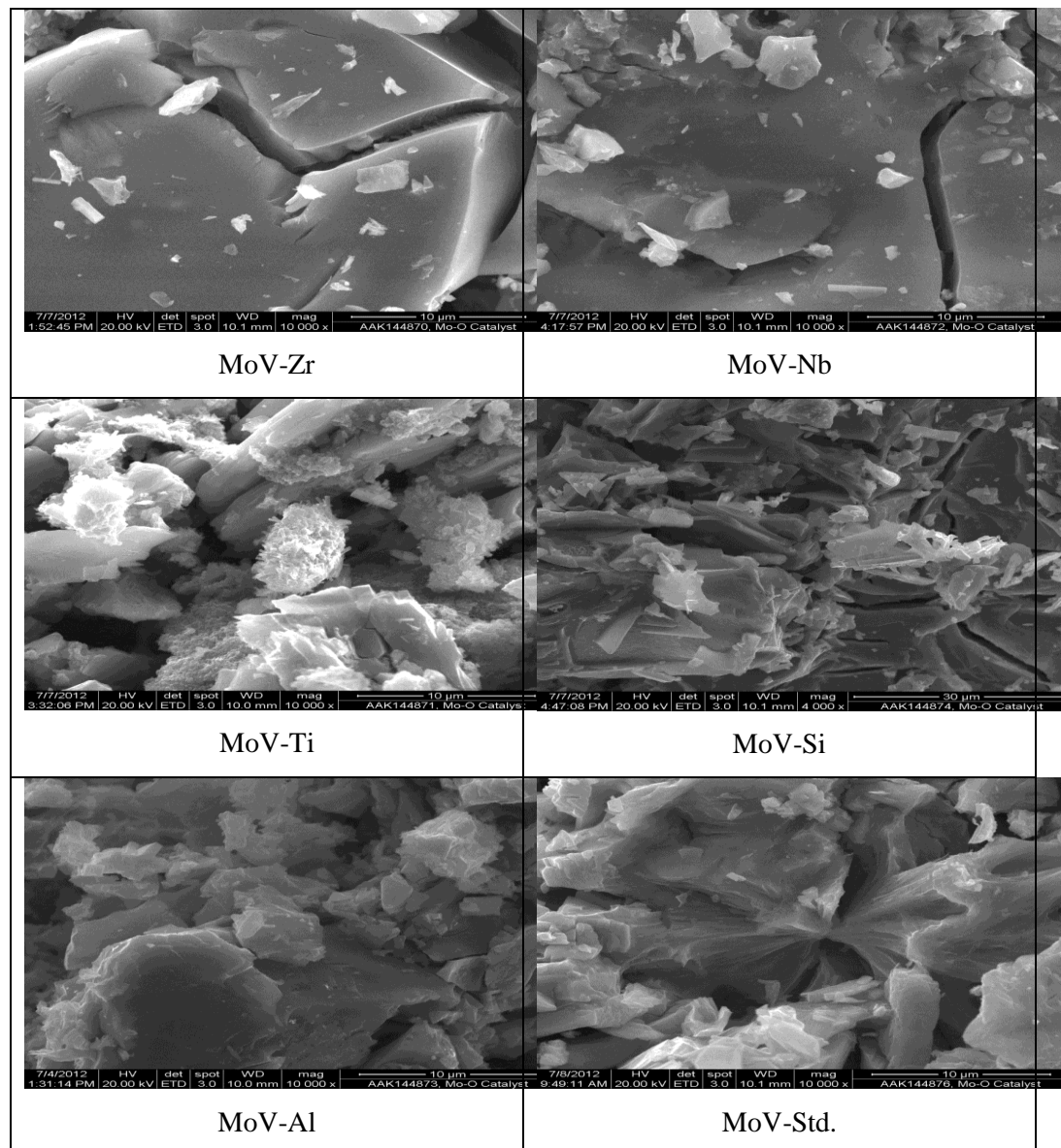
Fig.5.3: SEM images of catalyts with different oxide supports.

All samples are composed of irregularly shaped particles of variable size. The surface of the catalyst particles in all the samples are generally rough with surface cracks and fine irregularly shaped particles present.

5.3.5 EDX

EDX analysis results are given in Table 5.6. All samples prepared with the addition of different oxide supports show almost the same concentration ratio of Mo and V. However, silica concentration was lower than other prepared supported catalysts.

Table 5.6: Elemental content of particles determined by EDX (wt %).

Cat. Ref.	O	Mo	V	Zr	Nb	Ti	Si	Al	Mo/V
MoV-Zr	28.1	50.9	12.7	8.3	-	-	-	-	4.0
MoV-Nb	33.8	45.2	10.7	-	10.4	-	-	-	4.2
MoV-Ti	30.7	47.7	11.6	-		10.0	-	-	4.1
MoV-Si	30.4	50.1	11.9	-	-	-	7.7	-	4.2
MoV-Al	32.6	47.9	11.3	-	-	-	-	8.6	4.2
MoV-std	31.5	55.6	13.0	-	-	-	-	-	4.3

SEC Factors: EDAX

5.4 Discussion

The results described above indicate that several parameters influence the physiochemical and catalytic properties of supported oxides. The nature and phases of surface composition depend on the oxide supports (ZrO_2, Nb_2O_5, TiO_2, SiO_2 and Al_2O_3). Characterization studies have revealed that many factors play a role in the activity of the supported catalysts over MoV oxide. Bond [7] has studied various factors that impact the catalytic activity of supported catalysts. These include monolayer coverage of the surface vanadium species, stability of the monolayer coverage of surface vanadium species, oxidation state of the surface vanadium species, influence of environments upon the

molecular structures and oxidation state, acidity of the surface vanadium species and the influence of the oxide support on the vanadium surface and reactivity.

This study has primarily focused on a well-defined model of supported MoV oxide catalysts. This study addresses fundamental issues about the supported catalysts by reaction and characterization analysis. The oxidation state of the surface vanadium species (XPS), influence of environments upon the molecular structures and oxidation state, acidity of the surface vanadium species and the influence of the oxide support on the vanadium surface (XPS and XRD) were also examined.

The extent of V reduction during steady-state ODH is much lower than for the stoichiometric reduction of V^{5+} to V^{4+} or V^{3+}, reported by Banares and Gao [8]. Furthermore, only a fraction of the reduced centers are catalytically active in the reaction. The number of catalytically significant reduced centers depends only on alkane/O_2 ratios. The extent of reduction of the surface V^{5+} species also depends on the specific oxide support: V_2O_5-ZrO_2 > V_2O_5-Al_2O_3 > V_2O_5-SiO_2; the reactivity of the catalysts, for ethane ODH, follows the same ranking. This reported behavior of the supports matches the results found in this study of ethane ODH.

The ODH reaction of C_2–C_4 alkanes over supported transition metal oxides proceeds through a Mars-van Krevelen mechanism, which involves reduction of the catalyst by the alkane with participation of the lattice oxygen, followed by re-oxidation of the lattice with gaseous oxygen. As is well known, the catalyst performance depends on a number of factors, such as the chemical nature of the active oxygen species, the redox properties and the acid–base character, which in turn depend on transition metal loading, dispersion and support effects [9–11]. The different overall activities of reducible supported catalysts are most probably related to the influence of the support than to the structure of

the active species [12, 13]. The activity of the active metal sites is governed by the bonds formed with the support (and the activity of oxygen species in these bonds) during the chemical interaction of the surface hydroxyl groups and precursor salts. This in turn highly depends on the acid–base properties of the supporting material.

The investigation of the catalytic properties of supported vanadium catalysts for propane ODH showed that more selective catalysts were obtained on basic metal oxide supports [11, 14]. The presence of basic sites enhances the rapid desorption of the produced alkene from the catalytic surface, resulting in higher selectivities. Additionally, according to Kung [15], the selectivity for dehydrogenation versus formation of oxygen-containing products is strongly affected by the ability of the catalyst to form C-O bonds with the surface hydrocarbon, which depends on the reactivity of the oxygen species, and the number of reactive oxygens available at the reaction site. Reducibility has also been claimed to greatly affect the catalytic performance. Reports in literature have correlated variations in ODH activity with the ease of reducibility of the MO_x species on different supports [16], however other studies do not support such a trend [17].

For both propane and ethane, reactivity data for catalysts made of supported vanadium oxide are consistent both with kinetically relevant steps involving the dissociation of C–H bonds (methylenic C atom in propane) and with a Mars-van Krevelen redox mechanism involving lattice oxygen in C–H bond activation. The resulting alkyl species desorb as alkenes and the remaining O–H group recombines with neighboring O–H groups in order to form water and reduced V centers; the latter are re-oxidized by irreversible dissociative chemisorption of O_2. Surface oxygen, O–H groups and, especially, oxygen vacancies are the most abundant reactive intermediates during ODH on active VO_x domains [18–20]. The contribution to CO_x formation, conversely, mainly derives from adsorbed O species, at least in ethane ODH [21, 22].

The fraction of V-atoms that exist as catalytically reduced centers increases with increasing vanadium surface density and domain size up to surface densities typical of polyvanadate monolayers, and then reaches nearly constant values at higher surface densities; therefore, both isolated and polymeric species are active [23-26, 29, 46]. However, polymerized surface VO_4 species are more extensively reduced than the isolated species during steady-state alkane oxidation. The selectivity to propene formation is affected by surface reduction: the higher the surface reduction, the higher the selectivity [27]. The use of N_2O to replace O_2 causes the development of a more reduced, and more selective, surface [28, 30-35]. The reduction of the surface V^{5+} species significantly depends on the type of oxide support [36-37].

The acid character of a hydrocarbon decreases as the number of carbon atoms and/or the degree of saturation decrease. Thus, less acidic alkenes require stronger basic catalysts to limit the interaction of the alkene with the catalytic surface and preserve the alkene from further degradation. Furthermore, catalytic results for the ODH of propane and n-butane on VMgO catalysts suggest that, depending on the size of the reactant, the distance between the active sites on the catalytic surface can influence the selectivity in the ODH reactions [38].

Apart from the redox characteristics, the acid-base property of catalysts also plays a very important role for the initial activation of the C-H bond in the hydrocarbon. The acid-base interaction between alkane and the surface of catalysts can promote the approach of the hydrocarbon to the active sites. Banares [39] pointed out that for metal oxides, the surface acid-base features depend on the charge and radius of the cation. A new concept related to selectivity in mild oxidation catalysis of hydrocarbons was established [40-41] and a relationship between optical basicity and selectivity was found by Bordes et al.

[42]. Here the concept of optical basicity was defined as the electron donor power of the catalyst lattice oxygen.

5.5 Conclusion

Supported catalysts at low temperature have low activity; though zirconia and alumina supported catalysts have better activity even at low temperature as compared with other supported catalysts. The silica supported catalyst has the lowest activity compared to the other catalysts at low as well as high temperatures, which may be due to many factors, such as complete coverage of the active surface of the catalysts with silica oxide, or due to its higher surface area compared to the other supported catalysts, as reported by many researchers [43-44].

Alumina and zirconia supported catalysts have higher activity at higher temperatures. These catalysts have greater ethane conversion, with higher ethene selectivity and lower carbon oxide selectivity than the unsupported standard catalyst. The overall activity of the alumina supported catalyst is better than that of the zirconia and unsupported catalysts. Cavani et al. [43] reported that supported catalytic activity also depends on the process conditions.

5.6 Alumina loading impact on catalytic activity

5.6.1 Catalyst preparation

Catalysts were prepared as described in Chapter 2, maintaining the Mo and V molar ratio, 2.5:1. Three samples were prepared by adding 30, 50 and 70 wt. % alumina into the slurry of molybdenum and vanadium respectively as the support material. These samples were labelled as MoV-Al-30, MoV-Al-50 and MoV-Al-70 respectively. These catalysts were tested at different temperatures. Samples were characterized by BET, XRF, XRD,

SEM and EDX techniques to analyze various structural and compositional properties of the materials.

5.6.2 Experimental results

Catalysts prepared with an alumina support showed low activity. Product distributions showed that the carbon monoxide, carbon dioxide and acetic acid (AA) selectivity decreases while the ethene selectivity inreases with increasing alumina support concentration. Ethane conversion decreases with increasing alumina concentration. Data for alumina supported catalysts are presented in Table 5.7.

Table 5.7: Alumina supported catalytic activity at 290 ºC.

Catalysts	Conv. (%)		Selectivity (%)				Yield (%)
Ref.	C_2H_6	O_2	CO_2	CO	AA	C_2H_4	C_2H_4
MoV-Std	16.8	68.9	6.3	10.4	8.5	74.8	12.6
MoV-Al-30	10.3	39.8	5.2	11.3	3.2	80.2	8.3
MoV-Al-50	8.2	30.1	4.8	10.2	3.7	81.3	6.7
MoV-Al-70	5.7	19.4	3.5	6.1	5.1	85.3	4.9

Reaction conditions: Pressure = 70 psig, temp. = 290 ºC, feed gas = ethane: oxygen: nitrogen (40:10:50), catalyst wt. = 1 g, feed flow = 25 ml/min.

5.6.2.1 Reaction temperature impact on alumina supported catalysts

Alumina supported catalysts were tested at different reaction temperatures to see their catalytic behaviour. Temperature has a direct impact on the catalytic activity; increased temperature results in increased activity.

(i) Catalyst MoV-Al-30 activity at different temperatures

Catalytic activity data shows a slight decrease in ethene selectivity as ethane conversion increases with increasing reaction temperature. At higher temperatures MoV-Al-30 has a high ethane conversion and ethene yield; however there is a slight increase in carbon oxide and AA formation. The catalytic activity results for MoV-Al-30 are given in Table 5.8.

Table 5.8: MoV-Al-30 catalytic activity at different temperatures.

Temp.	Conv. (%)		Selectivity (%)				Yield (%)
(°C)	C_2H_6	O_2	CO_2	CO	AA	C_2H_4	C_2H_4
290	10.3	39.8	5.2	11.3	3.2	80.2	8.3
310	17.9	71.6	7.1	16.4	4.5	72.1	12.9
320	22.8	91.2	8.6	18.4	5.6	67.4	15.4
330	24.6	100.0	10.3	21.3	7.1	61.3	15.0

Reaction conditions: Pressure = 70 psig, feed gas = ethane: oxygen: nitrogen (40:10:50), catalyst wt. = 1 g, feed flow = 25 ml/min.

(ii) Catalyst MoV-Al-50 activity at different temperatures

The catalyst prepared with 50 wt. % alumina support (MoV-Al-50) showed lower ethane conversion compared to 30 wt. % alumina supported catalyst, but gives higher ethene selectivity. Ethene selectivity decreases as ethane conversion increases with increasing reaction temperature. At higher temperatures, MoV-Al-50 performs well with moderate ethane conversion. At 330 °C oxygen is not completely consumed (converted), although, there is a slight increase in carbon oxide and AA formation. MoV-Al-50 activity results are given in Table 5.9.

Table 5.9: MoV-Al-50 catalytic activity at different temperatures.

Temp.	Conv. (%)		Selectivity (%)				Yield (%)
(ºC)	C_2H_6	O_2	CO_2	CO	AA	C_2H_4	C_2H_4
290	8.2	30.1	4.8	10.2	3.7	81.3	6.7
310	15.3	67.0	6.5	15.1	5.1	73.3	11.2
320	19.4	79.6	8.1	17.2	6.8	67.9	13.2
330	21.9	91.2	9.5	19.1	8.5	62.9	13.8

Reaction conditions: Pressure = 70 psig, feed gas = ethane: oxygen: nitrogen (40:10:50), catalyst wt. = 1 g, feed flow = 25 ml/min.

(iii) Catalyst MoV-Al-70 activity at different temperatures

The catalyst prepared with 70 wt. % alumina support (MoV-Al-70) has very low activity compared to the other (30, 50 wt. %) alumina supported catalysts. Ethene selectivity decreases as ethane conversion increases with increasing reaction temperature. Even at 330 °C, MoV-Al-70 gives low ethane conversion.

Table 5.10: MoV-Al-70 catalytic activity at different temperatures.

Temp.	Conv. (%)		Selectivity (%)				Yield (%)
(ºC)	C_2H_6	O_2	CO_2	CO	AA	C_2H_4	C_2H_4
290	5.7	19.4	3.5	6.1	5.1	85.3	4.9
310	8.1	28.3	4.9	7.1	8.8	79.2	6.4
320	9.6	31.6	5.6	7.7	11.3	75.4	7.2
330	11.7	36.8	6.8	8.4	13.4	71.4	8.4

Reaction conditions: Pressure = 70 psig, feed gas = ethane: oxygen: nitrogen (40:10:50), catalyst wt. = 1 g, feed flow = 25 ml/min.

At high temperature, a low oxygen consumption (only 40 mol %) was observed. The catalytic activity could increase further at higher temperatures as more oxygen remains unconverted at 330 °C. However, there is a slight increase in the formation of carbon monoxide and carbon dioxide. It is interesting that at high temperature, 70 wt. % alumina

supported catalyst gives a higher AA formation compared with those using a lower concentration of alumina. Data for MoV-Al-70 activity are given in Table 5.10.

Fig. 5.4 clearly shows that increasing the reaction temperature increases the ethane conversion for all alumina supported catalysts. However, catalysts with a higher alumina concentration are less active compared to low alumina concentration catalysts.
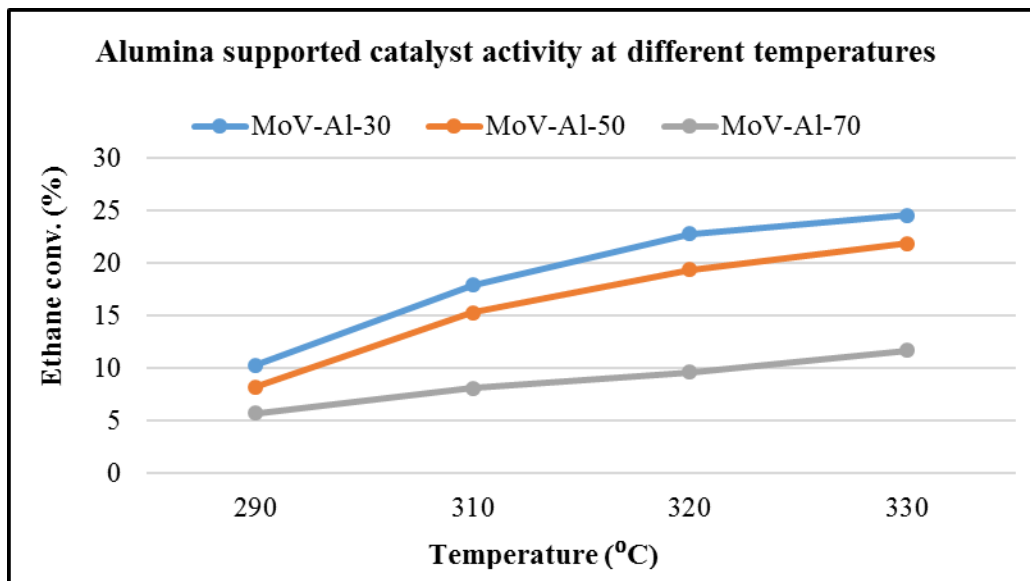
Fig.5.4: Alumina supported catalytic activity at different temperatures.

5.6.3 Catalyst Characterization

These samples were characterized by BET, XRF, XRD, SEM and EDX techniques.

(i) BET

Surface area (BET) of MoV oxides catalyst prepared with alumina support was measured. There is a slight decrease in the surface area from lower concentration to higher concentration of alumina supported catalysts. Alumina supported catalysts BET data is shown in Table 5.11.

163

Table 5.11: Surface area of alumina supported catalysts.

Catalyst Ref.	Surface area (m^2/g)
MoV-Al-30	19
MoV-Al-50	17
Mov-Al-70	14

(ii) XRF

The bulk composition of catalysts prepared with alumina support was determined by XRF spectroscopy. The bulk composition of catalysts is given in Table 5.12.

Table 5.12: Alumina supported catalyst composition by XRF analysis.

Catalyst Ref.	MoO$_3$	V$_2$O$_5$	Al$_2$O$_3$
Loading	(%)	(%)	(%)
MoV-Al-30	55.9	19.6	24.4
MoV-Al-50	50.9	17.5	31.5
MoV-Al-70	41.4	12.5	45.8

(iii) XPS

XPS was performed using a Kratos Axis Ultra-DLD photoelectron spectrometer as described in Chapter 2. Binding energy (BE) was referenced to O *1s* core (530.40 eV).

Table 5.13: Binding energies of elements and identified compounds of alumina supported catalysts.

| Catalyst	Binging Energy (eV)			Identified compounds
Ref.	Mo3d$_{5/2}$	V2p$_{3/2}$	Al2p$_{3/2}$	
MoV-Al-30	232.9	517.4	-	MoO$_3$, V$_2$O$_5$
MoV-Al-50	232.9	517.3	74.5	MoO$_3$, V$_2$O$_5$, Al$_2$O$_3$
MoV-Al-70	232.8	517.3	74.4	MoO$_3$, V$_2$O$_5$, Al$_2$O$_3$

The BE of Mo $3d_{5/2}$, V$2p_{3/2}$ for MoV oxide with alumina supported catalysts are reported in Table 5.13. In these samples, the standard binding energies are 232.2 ± 0.2 for Mo^{6+}, 516.6 ± 0.1 for V^{5+}, 515.9 ± 0.4 for V^{4+} oxides. These values match those of the literature [44-47]. The Mo photopeak is characteristic of Mo^{6+} by its BE as well as by its FWHM. Reduced Mo species, Mo^{5+} (230.8-231.8 eV) and Mo^{4+} [44-45] are absent; whilst some vanadium is reduced. The relative ratios of V^{5+} and V^{4+} are given in Table 5.14 after peak decomposition. The relative ratio of V^{5+} to V^{4+} does not change with the concentration of alumina support, as shown in Table 5.14.

Table 5.14: Concentration and ratios of V^{5+} and V^{4+} in alumina supported catalysts.

Catalyst Ref.	FMHM V2p(eV)	FWHM V2p5$^+$(eV)	FWHM V2p4$^+$(eV)	V^{4+}/V^{5+} Ratio
MoV-Al-30	2.044	1.27	1.20	0.44
MoV-Al-50	2.080	1.49	1.23	0.36
MoV-Al-70	1.980	1.38	1.21	0.39

(iv) XRD

The XRD patterns of the alumina supported catalysts shows a crystalline type structure in the samples. The patterns with varying alumina concentration are presented in Fig. 5.5. These show that the some peaks in the beginning shifted in the crystalline phase. The peaks corresponding to a lower concentration of alumina increases with increasing alumina concentration (70 wt %). However, the catalysts with less amount of alumina are catalytically more active compared to the samples with a higher concentration of alumina.
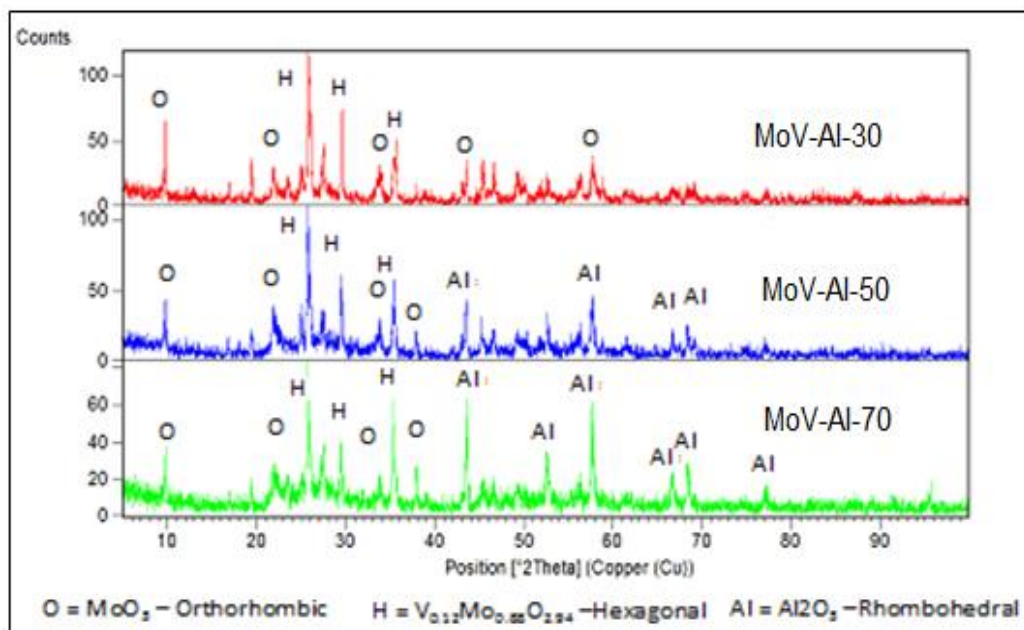
Fig.5.5: XRD patterns of alumina supported catalysts.

Fig. 5.5 depicts the XRD patterns of the catalysts prepared by the addition of different amounts of alumina as a support. They contain reflection lines of different phases which were found to change slightly with varying alumina concentration. The crystalline structure is represented with the orthorhombic and hexagonal phases. The orthorhombic phase decreases and the hexagonal phases become more prominent as alumina concentration increases.

(v) SEM and EDX

Surface morphology examination was carried by using SEM with EDX. All alumina supported catalysts were analyzed for surface morphology as described in Chapter 2. Images are shown in Fig. 5.6.

166

(a) General view- (MoV-Al-30) | (b) Close-up- (MoV-Al-30)

(a) General view- (MoV-Al-50) | (b) Close-up- (MoV-Al-50)

(a) General view- (MoV-Al-70) | (b) Close-up- (MoV-Al-70)
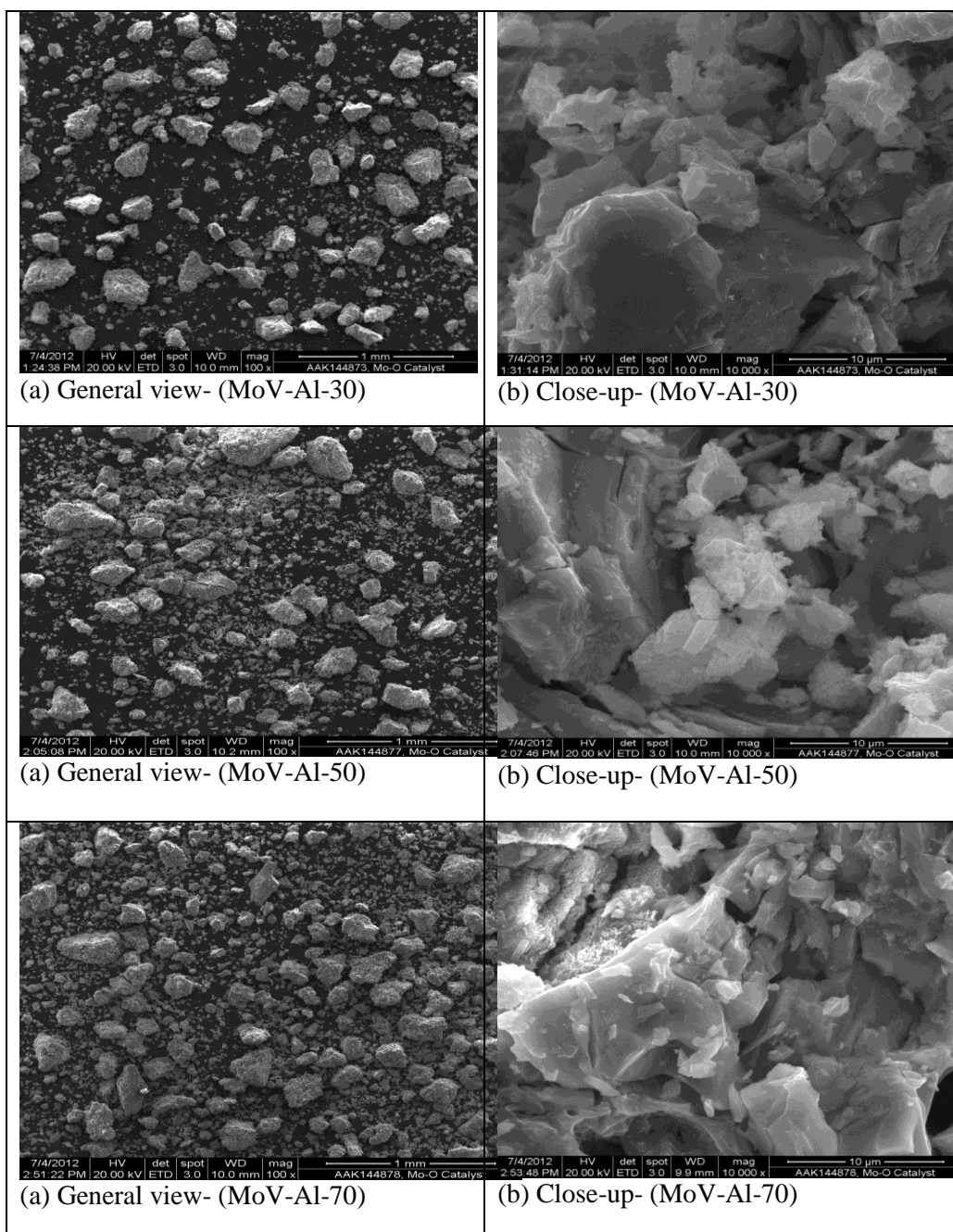
Fig.5.6: SEM images of catalysts prepared with different concentrations of alumina.

The catalyst samples MoV-Al-30, MoV-Al-50, and MoV-Al-70 are composed of both coarse and fine irregularly shaped particles. The individual particles had both rough and smooth sides. The surface of the particles contained cracks and bundles of thin flake like crystal arranged in flower-like morphology (Figs. 5.6).

Table 5.15: Elemental content of alumina supported catalysts determined by EDX (wt %).

Catalyst Ref.	O	Mo	V	Al
MoV-Al-30	31.6	50.9	11.3	6.6
MoV-Al-50	29.7	49.6	10.3	10.4
MoV-Al-70	29.1	45.8	8.2	16.9

The elemental compositions of catalysts prepared with different concentrations of alumina support were determined by EDX. These showed the presence of O, Mo, V and Al as given in Table 5.15. Particle to particle compositional variability was observed in almost all samples. Data indicate a proportional concentration of alumina support in the catalysts.

5.6.4 Discussion

The effect of calcination temperatures on the physiochemical properties of MoV mixed oxides was clearly observed as phase evolution as the calcination temperature was varied. However, the various calcination temperatures were not found to have a large impact on the morphology of the samples, rod-like structure as seen by SEM, an observation fully supported by the BET and XRD measurements. The results of these samples, calcined at different temperatures, highlights the benefits of the study of these calcination temperatures in order to reach the required active phase, which has a significant impact on the activity.

Though it is difficult to formulate an exact reaction mechanism with the present investigation, a tentative surface mechanism for the ODH of ethane over MoVAl based catalysts has been proposed based on the information obtained. The efficiency of the present catalyst system for the selective ethane oxidation is assumed to be due to the

presence of MoV_2O_8 and other reduced species supporting the MoO_3 phase [48]. Activation of the C–H bond of ethane on the catalytic surface, possibly via an unstable ethoxy intermediate, leads to ethene formation. Part of the produced ethene adsorbs either weakly or strongly, selectivity on the site of the catalyst surface in the presence of water and oxygen,which leads to the formation of intermediates such as ethanol and acetaldehyde and finally to acetic acid. Although alcohol/aldehyde products were not seen as final products, their concentration up to 150 ppm could be detected in the GC analysis. With the present experimental conditions, the oxidation rate of these alcohol/ aldehyde intermediates, leading to the formation of AA, might be very high. Any of these intermediates, ethane and/or AA, are oxidized to CO_x, if they are strongly adsorbed on any non-selective phase (e.g., alumina or V_2O_5). Desorption of ethene is easier if it is bound on a weak acid site such as MoO_3 [49].

GHSV has strong effect on the catalytic activity as evident from the catalytic results obtained during the ODH of ethane. Ethene, carbon dioxide, carbon monoxides and acetic acid are the main reaction products. The AA selectivity is lower than 10 %, especially at atmospheric pressure. From these results it can be concluded that activity increases as GHSV decreases. The catalytic activity increases with increasing temperature whilst ethene selectivity decreases. The highest activity is obtained at a GHSV of 780 h^{-1}, 330 °C and atmospheric pressure, showing 16.3 % ethene yield at 27.4 mol % ethane conversion. The activity is roughly doubled by increasing the reaction pressure from atmospheric to 70 psig.

5.6.5 Conclusion

This study establishes the impact of various parameters that directly influence the catalytic activity towards the ODH of ethane to ethene. The reduction of V^{5+} to V^{4+} has a

significant contibution to this reaction. The catalytic oxidation cycle is completed by reoxidation of the vanadium V^{4+} to V^{5+}, which is supported by XPS data. The production of carbon oxide shows dependence on the ethane partial pressure whilst AA production is independent of ethane partial pressure. This strongly suggests that the primary ODH product of ethane is ethene and that carbon oxide and AA are formed by its subsequent oxidation. The role of reaction temperature and pressure upon the acetic acid production is informative. The oxidation of ethene to acetic acid may involve an analogous first step, giving an ethoxide species, ($MOH + C_2H_4 = MOC_2H_5$). Certainly this oxidation of ethene to AA is well known for molybdenum- and vanadium containing catalysts [50].The activity results highlight the impacts of various parameters which can be optimised to produce the most active MoV oxide catalysts.

5.7 References

[1] X. Li, E. Iglesia, *Appl. Catal. A*: *Gen*. **334** (2008) 339.

[2] I. E. Wachs, B. M. Weckhuysen, *Appl. Catal. A*: *Gen*. **157** (1997) 67.

[3] M. Bouchard, M. Roussel, E. Bordes-Richard, K. Karim, S. Al-Sayari*, Catal. Today* **99** (2005) 77.

[4] E. Thorsteinson, T. P. Vilson, F. G. Young, and P. H. Kasai, *J. Catal.* **52** (1978) 116.

[5] G. Centi, E. Giamello, D. Pinelli, F. Tifiro, *J. Catal*. **130** (1991) 220.

[6] N. Das, H. Eckert, H. Hu, I. E. Wachs, J. F. Walzar, F. J. Feher, *J. Phys. Chem*. **97** (1993) 82.

[7] G. C. Bond, *Appl. Catal*. **71** (1991) 1.

[8] M. A. Banares, M. V. Martınez-Huerta, X. Gao, J. L. G. Fierro, I. E. Wachs, *Catal. Today* **61** (2000) 295.

[9] T. Blasco, J. M. Lopez-Nieto, *Appl. Catal. A* **157** (1997) 117.

[10] E. A. Mamedov, V. Cortes Corberan, *Appl. Catal. A* **127** (1995) 1.

[11] A. A. Lemonidou, L. Nalbandian, I. A. Vasalos, *Catal. Today* **46** (2000) 333.

[12] B. Grzybowska-Swierkosz, *Top. Catal*. **21** (2002) 35.

[13] G. Deo, I. E. Wachs, *J. Catal*. **146** (1994) 323.

[14] A. Corma, J. M. Lopez Nieto, N. Paredes, M. Perez, Y. Shen, H. Cao, S. L. Suib, *Stud. Surf. Sci. Catal*. **72** (1992) 213.

[15] H. H. Kung, *Adv. Catal*. **40** (1994) 1.

[16] K. Chen, S. Xie, A.T. Bell, E. Iglesia, *J. Catal*. **198** (2001) 232.

[17] D. S. Kim, I. E. Wachs, K. Segawa, *J. Catal*. **146** (1994) 268.

[18] K. Chen, A. Khodakov, J. Yang, A. T. Bell, E. Iglesia, *J. Catal*. **186** (1999) 325.

[19] K. Chen, E. Iglesia, A. T. Bell, *J. Catal*. **192** (2000) 197.

[20] M. D. Argyle, K. Chen, A. T. Bell, E. Iglesia, *J. Phys. Chem. B* **106** (2002) 5421.

[21] P. M. Michalakos, M. C. Kung, I. Jahan, H. H. Kung, *J. Catal*. **140** (1993) 226.

[22] E. Mamedov, A. Crtes Coberan, *Appl. Catal. A* **127** (1995) 140.

[23] X. Gao, M. A. Banares, I. E. Wachs, *J. Catal*. **188** (1999) 325.

[24] M. A. Banares, M. V. Martınez-Huerta, X. Gao, J. L. G. Fierro, I. E. Wachs, *Catal. Today* **61** (2000) 295.

[25] X. Gao, I. E. Wachs, *J. Catal*. **146** (1994) 335.

[26] X. Zhang, J. Liue, Y. Jing, Y. Xie, *Appl. Catal. A* **240** (2003) 143.

[27] G. Colorio, J. C.Vedrine, A. Auroux, B. Bonnetot, Appl. Catal. **137** (1991) 55.

[28] G. Busca, V. Lorenzelli, G. Oliveri, G. Ramis, *Stud. Surf. Sci. Catal.* **82** (1994) 253.

[29] A. Bruckner, E. Kondratenko, *Catal. Today* **113** (2006) 16.

[30] N. Dimitratos, J. C. Vedrine, *Catal. Today* **81** (4) (2003) 561.

[31] M. D. Argyle, K. Chen, C. Resini, C. Krebs, A.T. Bell, E. Iglesia, *J. Phys. Chem. B* **108** (2004) 2345.

[32] X. Gao, J. M. Jehng, I. E. Wachs, *J. Catal*. **209** (2002) 43.

[33] S. Yang, E. Iglesia, A.T. Bell, *J. Phys. Chem. B* **110** (2006) 2732.

[34] A. Christodoulakis, M. Machli, A. A. Lemonidou, S. Boghosian, *J. Catal*. **222** (2004) 293.

[35] M. D. Argyle, K. Chen, E. Iglesia, A. T. Bell, *J. Phys. Chem. B* **109** (2005) 2414.

[36] M. D. Argyle, K. Chen, A. T. Bell, E. Iglesia, *J. Catal*. **208** (2002) 139.

[37] G. Mul, M. A. Banares, G. Garcia Cortez, B. van der Linden, S. J. Khatib, J. A. Moulijn, *Phys. Chem. Chem. Phys*. **5** (2003) 4378.

[38] A. Khodakov, B. Olthof, A. T. Bell, E. Iglesia, *J. Catal*. **181** (1999) 205.

[39] M. A. Banares, *Catal. Today* **51** (1999) 319.

[40] K. Kijenski, A. Baiker, M. Glinski, P. Dollenmeier, A. Wokaun, *J. Catal*. **101** (1986) 1.

[41] V. Nikolov, D. Klissurski, A. Anastasov, *Catal. Rev. Sci. Eng*. **33** (1991) 1.

[42] P. Moriceau, A. Lebouteiller, E. Bordes, P. Courtine, *Phys. Chem*. **1** (1999) 5735.

[43] F. Cavani, J. H. Teles, *Chem. Sus. Chem.* **2** (2009) 508.

[44] L. Dambies, C. Guimon, S. Yiacoumi, E. Guibal, *Colloid Surf. A*. **177** (2001) 203.

[45] D. Kim, S. V. Kagwade, C. R. Clayton, *Surf. Interf. Anal.* **26** (1998) 155.

[46] *http://www.lasurface.com/. Publi* (1997).

[47] *http://www.srdata.nist.gov.*

[48] J. M. Jehng, I. E. Wachs, F. T. Clark, M. C. Springman, *J. Mol. Catal*. **81** (1993) 63.

[49] E. Heracleous, M. Machli, A. A. Lemonidou, I. A. Vasalos, *J. Mol. Catal. A*. **232** (2005) 29.

[50] Y. Takia, A. Ozaki, Y. Moro-Oka, *J. Catal.* **27** (1972) 185.

Chapter 6

Conclusions and Proposed Future Work

This thesis has attempted to examine some important aspects of ethane ODH since its initial development. A detailed historical review is provided in Chapter 1 in which a comparison of the commonly used catalysts is given, along with proposed mechanisms for ethane ODH. Chapter 2 is devoted to a detailed description of the equipment and methods used during this study.

One of the main objectives of the current thesis was the reproducible synthesis of a catalyst which is highly selective to ethene and consequently shows low selectivity towards carbon oxide formation. MoV oxide catalysts have been found to be an active and selective in the reaction. The oxides are usually prepared by employing hydrothermal method as reported by numerous references that contain both the single hexagonal phase

and the single orthorhombic phase of MoV mixed oxide. This method, however, is only applicable at lab scale synthesis due to uneconomical scaled up production. Therefore, in this work it was desired to synthesize an active and selective catalyst using a more conventional method. The method chosen is a slurry preparation followed by drying in an oven; followed by calcination of the obtained solid. In order to study the chemical properties of the catalyst many parameters have been studied.

Various preparation variables for this catalysts have been studied in order to find out the optimum preparation conditions. Catalysts prepared by precipitation and drying to remove the excess water from the slurry by heating with continuous stirring has been found better than that prepared by the previously studied methods of spray drying or hydrothermal treatment in an autoclave. A detailed investigation has been done for the optimization of the reaction conditions. The optimum process condition was found at temperature 290 ℃ and pressure 70 psig with ethane oxygen ratio 4:1. It has been observed that at atmospheric pressure, the activity was low but with the highest ethene selectivity. At pressures higher than 70 psig the activity increases with increasing temperature to more than 290 ℃ and ethene selectivity decreases rapidly followed by increase in carbon oxide formation.

Catalytic results with high conversion of ethane at low feed concentrations show high selectivity towards carbon oxide and low selectivity of ethene. While high concentration of ethane in the feed gas shows lower conversion of ethane but a higher selectivity to ethene with low carbon oxide formation. However, at higher temperature e.g. 310 ℃, conversion increases followed by increasing carbon oxide formation due to the high consumption of oxygen at the higher temperature. There is also a significant impact on the acetic acid (AA) selectivity at higher temperature and pressure in the reaction.

The requirement for an improved catalyst for the selective synthesis of ethene from ethane encouraged an investigation of the effect of adding oxalic acid on an existing but modified MoV catalyst. Catalysts prepared with oxalic acid showed higher activity compared to catalysts prepared without oxalic acid in the slurry method. It was shown that a catalyst prepared with oxalic acid with a pH lower than 4 has more activity than prepared at different pH catalysts. Catalyst activity increases with the addition of oxalic acid from 2.5 to 7.5 g, but starts to decrease on adding more than 10 g of oxalic acid in the preparation procedure. Catalysts prepared with zero or very low amounts of oxalic acid and those prepared with higher than 10 g of oxalic acid have lower surface area (12-14 m^2/g) and these catalysts have low catalytic activity. On the other hand, catalysts prepared with 2.5-10.0 g of oxalic acid have high surface areas (19-26 m^2/g) and show high catalytic activity giving high conversion of ethane as well as more selectivity to ethene with lower formation of carbon oxide in the products. Catalysts prepared with the addition of oxalic acid showed significant changes in their morphology and their structure changes from crystalline to amorphous. Catalysts prepared without the addition of oxalic acid or the addition of very small amount (1 g) of oxalic acid showed a crystalline structure. Similar behavior is seen with catalysts prepared by adding more than 10 g of oxalic acid, which show a good crystalline structure. On the other hand, other catalysts prepared by adding from 5-10 g of oxalic acid gave an amorphous structure and these also showed higher activity than catalysts having a crystalline structure.

Oxalic acid was used successfully during catalyst preparation to modify the physiochemical properties of the $Mo_1V_{0.4}O_x$ catalyst for ethane ODH. Comparison shows that the addition of oxalic acid not only enhances the ethane conversion, but also improves its ethene selectivity while also reducing carbon oxide formation. This is due to oxalic acid converting V^{5+} to V^{4+} in the starting solution to provide a driving force for the

formation of an active phase in the MoV material, which is directly related to ethene formation. In addition, the performance of the catalyst is strongly related to the amount of oxalic acid used during the catalyst preparation. Catalysts prepared with 5 to 10 g oxalic acid addition showed the highest ethane conversion and ethene selectivity because it contains the expected phase composition and good redox capacity. Therefore, employment of reductive oxalic acid improves the catalytic performance of the $Mo_1V_{0.4}O_x$ catalyst.

The effect of the addition of a support for MoV mixed oxide catalyst on the performance was also studied. Different supports like zirconia, niobium oxide, titania, silica and alumina at a particular concentration of 30 wt. % were used to see their impact on ethane ODH to ethene. Variation of the supports shows significant impact even at lower temperature. Zirconia and niobium oxide seems to be good at lower temperatures (290 ºC), while titania and silica give low activity. At higher temperatures, alumina shows higher activity and ethene selectivity compared to zirconia and niobium oxide supported catalysts.

An additional effort has been made for the study of synthesis of catalysts with varying concentration of alumina over the MoV mixed metal catalysts. It has been found that the catalyst with a high support concentration of 70 wt. % was still very active. It gave 12 % ethane conversion at 330 ºC temperatures with small amount of carbon oxide formation. Alumina has good effect of lowering CO_x formation with increasing loading over the catalyst, with slight increases in acetic acid formation.

Proposed future work

The catalytic (MoV) system can be further improved by the addition of dopants (e.g. K, Mg etc.) that can further suppress the CO_x and acetic acid formation. Variation in reaction pressure, temperature and ethane oxygen ratio can also be studied in the future. Varying the concentrations of the dopant can influence the surface basicity or acidity leading to different reaction pathways.

Various aspects of adding transition metals as promoters (e.g. Cr, Pd, Nb, W and Re) into the catalyst can change the physicochemical properties and catalytic performance of the catalyst. As molybdenum-vanadium compounds retain their high selectivity to desired products at higher temperatures, it would be necessary to attempt to increase the conversion of the reactant with a known promoter which produces a high conversion of reactant.

Attempting to increase the surface area of the catalyst is possible as all of the catalysts in this study have been found to have a low surface area, hence there may only be a fraction of active sites available. By increasing the surface area of the catalyst, potentially more active sites within the catalyst would become available, increasing the conversion of reactant.

Appendix 1

Fixed bed reactor

A schematic representation of the single fixed bed reactor system is shown below. The reactor unit made of stainless steel tube (3/8 inch i.d) housed within the furnace. The furnace controlled the temperature of the reactor through a thermocouple dipped inside the middle of the catalyst bed. The temperature displayed set values and real temperature values on the monitor.
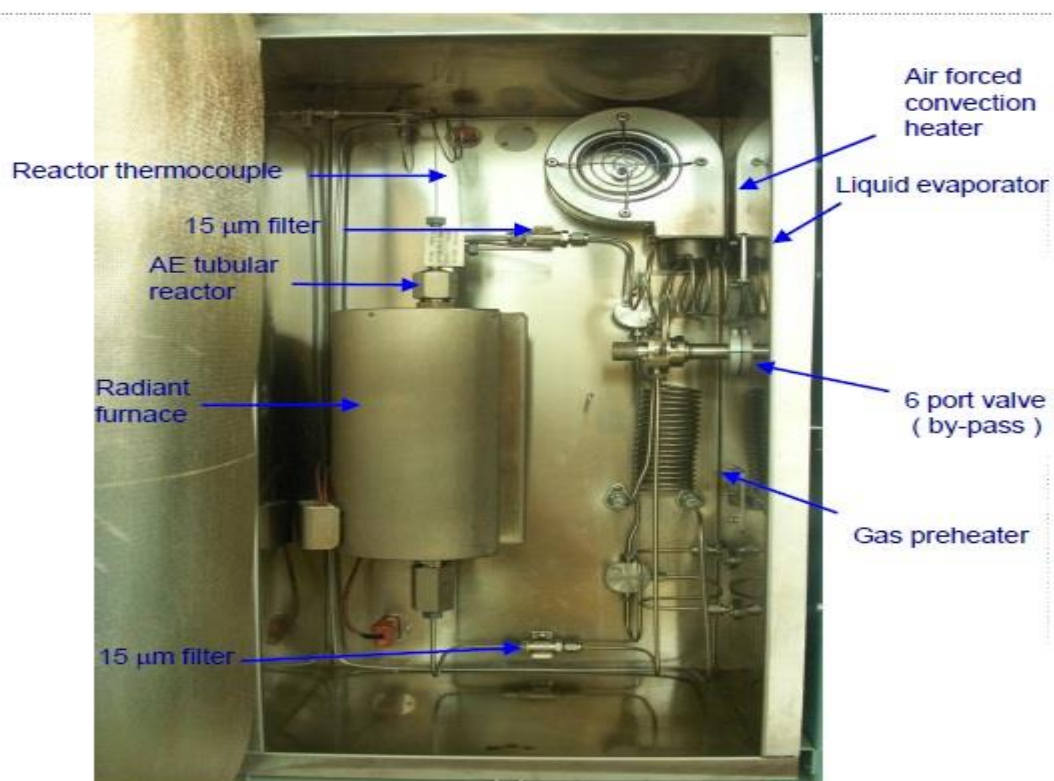

Fig. 1: Fixed bed reactor system, hot box chamber, reactor thermocouple, tubular reactor, 6-port valve, gas preheated coil, radiant furnace.

Appendix 2

Flow Diagram of Fixed bed reactor

A schematic diagram of the feed gas flows to the fixed bed reactor. All lines are equipped with mass flow controllers, filters, pressure gauge, pressure regulators and check valves. The system has both functioned to collect liquid product stream and also send only gas to the GC for analysis and as well sending entire product stream as vapor phase to the GC for the product analysis without condensing the liquid.
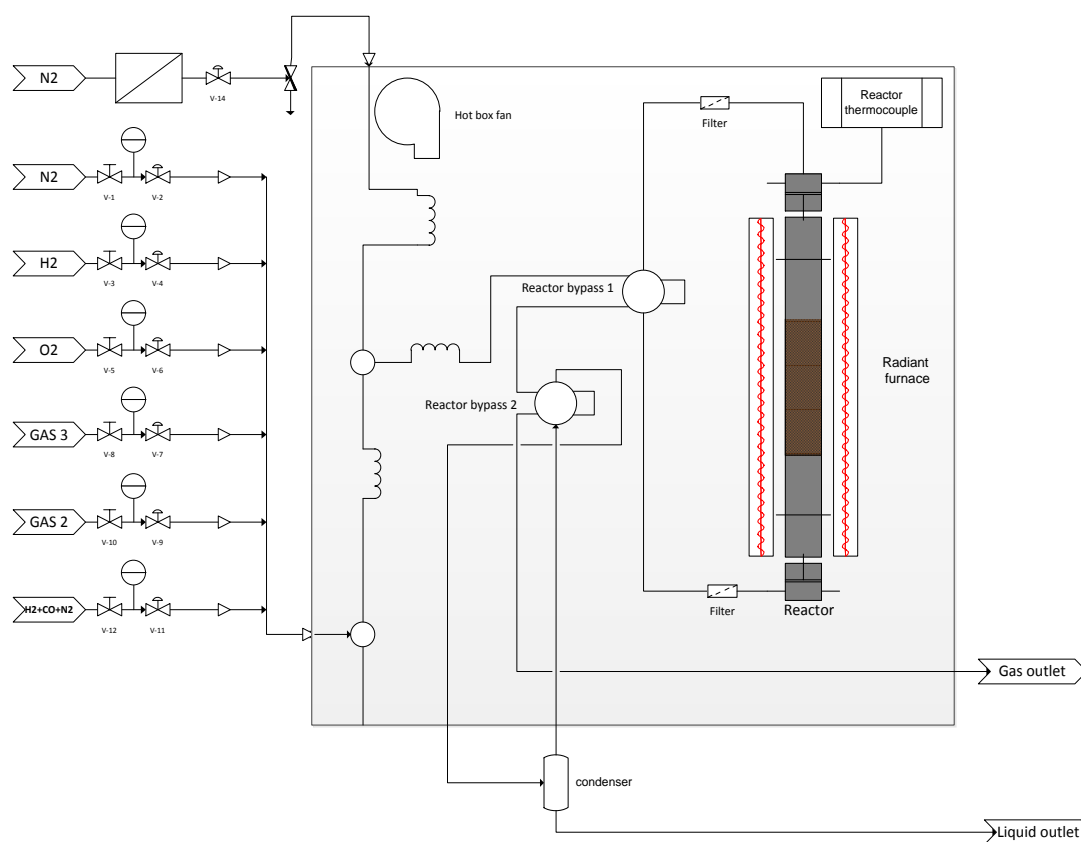
Fig. 2: Flow Diagram of Fixed bed reactor, feed gas lines, two port valves, and condenser

181

Appendix 3

Product Analysis by GC

Product Analysis for catalysts tested in fixed bed reactor by GC

Reaction products (gaseous stream) of the lower hydrocarbons, oxygenated and other products were analyzed by an online gas chromatography instrument. The gas chromatography (GC) used for the online sample analysis was HP Model Agilent 6890 instrument, fitted with injector and two detectors (TCD and FID).

The GC configuration consists of switching valves, sample loop, separating columns and data acquisition system. GC was configured with one 10 port and one 6-port valve, and have three different columns to analyze the gaseous stream.

1) Molecular sieve   :   6' X 1/8" SS Placed into oven at 100 °C.

2) Hayesep Q   :   6' X 1/8" SS Placed into oven at 100 °C.

3) Porapak N   :   0.62' X 1/8" SS Placed in the heated zone at 180 °C

The first two columns (Molecular sieve and Haysep Q) were connected to a TCD, while the third column (Porapak N) was connected to a FID. Oxygen, nitrogen and CO separated on the Molecular sieve column, CO_2, C_2H_4, C_2H_6, C_3H_6, C_3H_8, and water on Hayesep Q while acetic acid, acetone, and acrolein were separated on Porapak N column.

Following components can be separated and quantified by using this configuration; ethane, ethene, propane, propene, nitrogen, oxygen, carbon monoxide, carbon dioxide, acetic acid, acetone, acrolein, and water.

Appendix 4

Data evaluation

To obtain quantitative data, a procedure of data manipulation was required in the form of individual product selectivities from the integrated response factor of the gas chromatographs. The method was based on use of online response factors of particular products in gas phase and for liquids made separate calculation based on the injected amount of known concentration into GC of the product.

Standard gas mixtures of known volume percentage compositions were used to obtain components response factor based on components area counts.

Calculation of the Response Factor

The response factor of each component was calculated as follows:

Response factor   = amount (moles) / area of component

Amount moles can be calculated based on the standard gas mixture concentrations (volume %) of each component.

Calculation of moles of each component:

Volume (%) of component   = for each components of gas mixture

Mole amount of components   = component conc. Vol (%)/100/22.4

Standard gas mixture consist the following gas components:

CO_2, C_2H_4, C_2H_6, N_2, CO (10.1: 15.01: 14.9: 57.0: 3.1) %.

Using the area counts and no. of moles of each component can calculate the response factors for individual components.

Response factor = No. of moles of the component/ GC area counts of component

Calibration of oxygen was done by using air sample:

Several injections of air were made till get consistent results. The nitrogen response factor calculated from the calibration mixture was used to find the number of moles of nitrogen from which oxygen moles can be calculated from air. Dividing the oxygen moles with area, we get oxygen response factor.

Acetic acid calibration was done by using acetic acid solutions of known different concentrations. 0.6 ml of each standard solution of (2, 3, 5, 7 wt %) acetic acid was injected several time till get consistent results. The areas under the curve were found for each concentration.

Calculation to find acetic acid (AA) response factor is given below:

Concentration of Acetic acid solution   = 2 wt%

2 gm of AA   = 100 ml.

2/60 g moles of AA   = 0.1 L.

moles   = 0.6×10^{-6} L.

0.6 is the amount of injection (0.6 μL)

Moles of AA injected $= \dfrac{2 \times 0.6 \times 10e - 6}{60 \times 0.1}$

$= 2 \times 10^{-6}$ moles

Calculation of conversion and selectivity

An indication of the catalyst activity was determined by the extent of conversion of ethane or by the extent of volume reduction of the reagent gases. The ethane conversion and selectivity of ethene were calculated by the following equations:

Conv. Ethane (C_2H_6) % $= \dfrac{\text{moles[C2H6 in} - \text{C2H6 out]}}{\text{moles[C2H6 in]}} * 100$

Sel. Ethene (C_2H_4) % $= \dfrac{2[C2H4]}{[CO] + [CO2] + 2[C2H4] + 2[CH3COOH]} * 100$

Data collection by using online response factor

The varying response of the detector to each component was multiplying them with calibration factors. Then these were converted into moles by taking account the flows out of the feed. Moles of each product were converted into mole % and then selectivity was measured by taking carbon numbers into account.

Product analysis

Product data collection starts after the reaction gets stabilized. All products were in gaseous phase, therefore online analysis used to get the catalyst activity data.

Appendix 5

GC Configuration diagram

Gas Chromatography Schematic Diagram — GC- Agilent 7890 A Series

Column 1- Hayesep Q   Column 2- Molecular sieve   Column 3 - Porapak N

Channel A - Lower hydrocarbons, acetone, acetic acid, acrolien   Channel B - O_2, N_2, H_2, CO, CO_2, H_2O etc.